The Astronomical Journal, 170:84 (48pp), 2025 August https://doi.org/10.3847/1538-3881/ade1d1

Survey of Oxygen-rich AGB Stars Using the KVN 4 Receiving Bands—SMASTES. I.

Hyeon Baek[1,2], Se-Hyung Cho[1,3], Jaeheon Kim[3], Seung-Min Son[1,2], Dong-Hwan Yoon[3], and Kyung-Won Suh[2]
[1] Department of Physics and Astronomy, Seoul National University, Gwanakgu, Seoul 08826, Republic of Korea; cho@kasi.re.kr
[2] Department of Astronomy and Space Science, Chungbuk National University, Cheongju-City, 28644, Republic of Korea
[3] Korea Astronomy and Space Science Institute, 776 Daedeok–daero, Yuseong–gu, Daejeon 34055, Republic of Korea
Received 2024 October 15; revised 2025 May 12; accepted 2025 May 20; published 2025 July 11

Abstract

Simultaneous observations of 19 H_2O and SiO maser and thermal lines were performed toward 155 M-type oxygen-rich (O-rich) AGB stars. We used the upgraded four-band (22/43/86/129 GHz) wide receiving system of the Korean VLBI Network (KVN). The 155 O-rich stars composed of 50 semiregulars (SRs), 55 Miras, and 50 OH/IR stars were selected based on previous KVN H_2O/SiO detected sources. Both H_2O and SiO masers were detected in 23 stars among 50 SRs, 50 stars among 55 Miras, and 24 stars among 50 OH/IRs, respectively. Out of 50 SRs, H_2O-only masers, without corresponding SiO maser detection, were observed in four stars. In contrast, no H_2O-only masers were detected in any of the 55 Mira or 50 OH/IR stars, which differs from the pattern seen with SiO-only masers. Interestingly, in the 50 SRs, the SiO $v = 1$, $J = 2$–1 maser was detected more than the SiO $v = 1$, $J = 1$–0 maser despite requiring a higher excitation energy. The ^{28}SiO $v = 0$, $J = 1$–0, 2–1, 3–2 lines were detected more frequently at higher rotational transitions, especially in the SRs and Miras. The HCN and SiS were detected from 11 and 3 stars, respectively. For our observational results, we performed statistical analysis on the intensity ratio variations among H_2O and various SiO masers, chemical environments, and wind kinematics. The characteristics of these property variations were investigated in the IRAS two-color diagram in relation to their evolutionary stages.

Unified Astronomy Thesaurus concepts: Asymptotic giant branch stars (2100); Late stellar evolution (911); Astrophysical masers (103); Interstellar thermal emission (857)

Materials only available in the online version of record: figure set, machine-readable tables

1. Introduction

Most main-sequence stars with a low-to-intermediate mass evolve to the late evolutionary stage of the asymptotic giant branch (AGB). AGB stars are divided into two main types based on the carbon-to-oxygen ratio in their atmospheres: M-type oxygen-rich (O-rich) AGB with C/O < 1 and carbon-rich (C-rich) AGB. A transition object with C/O ~ 1 is also known as an S-type star. AGB stars are known to exhibit high mass loss rates and evolve into planetary nebulae through a post-AGB phase. However, key issues of the evolutionary process from AGB to post-AGB stars are still the subject of debate, such as mass loss mechanisms, physical and chemical effects of the thermal pulse, and the development of asymmetric outflows from the spherical morphology of the AGB to bipolar and multipolar features of post-AGB and planetary nebulae. SiO, H_2O, and OH masers, which are strongly emitted from many O-rich AGB stars, can be a good probe to investigate the above issues (B. Lewis 1989; H. Imai 2007; A. M. S. Richards 2012; D.-H. Yoon et al. 2018; A. M. S. Richards et al. 2022). In addition, they are distributed in a stratification structure from the star due to both chemical and excitation conditions (M. J. Reid & J. M. Moran 1981), providing important insights into the radial structure of the envelope and kinematics of the mass loss process in AGB stars. The SiO maser is emitted from the atmosphere affected by the pulsation between 2 and 4 R_* (P. Diamond et al. 1994) and the 22 GHz H_2O maser is emitted from above the dust layer (5–20 R_*, A. Richards et al. 2012) that is still accelerating. The OH maser occurs at the largest distance from the star ($\geqslant$100 R_*, A. Richards et al. 2012). Regarding the pumping mechanism, a SiO maser is generated by both collisional and radiative pumping (E. Humphreys et al. 2002; V. Bujarrabal 1994), while an H_2O maser is generated by collisional pumping (P. Lockett & M. Elitzur 1992).

However, because of the high variability of masers and the physical complexity of stellar pulsations that cause it, it is important to make an extensive statistical study based on homogeneous data obtained with simultaneous observations of various masers and an unbiased large sample of objects. The stellar variability mainly caused by pulsations as a common feature of AGB stars is classified into regular Mira-type, semiregular (SR), and irregular based on the appearance of light curves. In the case of SRs, they show more complex variability with the overtone pulsating mode (P. Wood et al. 1999). These stellar variabilities are intimately related with maser properties according to Miras, SRs, and Irregulars. As general characteristics of SiO masers observed in Miras, the pulsation period is stable from cycle to cycle, but line profiles vary greatly (L.-A. Nyman & H. Olofsson 1986). The fluxes of SiO masers are correlated with those of optical and infrared light curves. However, there is an average phase lag of ~0.2, though this somewhat varies according to objects and for the same object (A. Martinez et al. 1988; S.-H. Cho et al. 1996; J. Alcolea et al. 1999). Short-term variability over a period of a few days was reported by M. Balister et al. (1977) and F. Pijpers et al. (1994) in the SiO $v = 1$, $J = 1$–0 maser. In addition, VLBA observations show that the lifetimes of individual components follow a Gaussian distribution with the maximum value from 150 to 200 days (I. Gonidakis et al. 2010).

For about 3 yr monitoring of H_2O masers, M. Shintani et al. (2008) reported that a significant portion of H_2O masers emitted by 46 AGB stars exhibit periodic behavior, equal to the stellar pulsation period. They found a limited phase lag between H_2O maser flux variations and stellar pulsation periods. G. Rudnitskij et al. (2000) deduced the phase lags of a 0.2–0.4 period for U Ori. However, SRb type variables exhibit intensity variations of H_2O masers on a range of timescales, i.e., individual feature variations on timescales from months to 1.5 yr and decade-long variations of the general brightness level, independent from individual features (J. Brand et al. 2020). They suggested that the contribution of optical variability to the maser brightness may be obscured by strong short-term maser fluctuations. For the average lifetime of an H_2O maser, U Her maser components show a lifetime of 0.5–1 yr (A. Winnberg et al. 2011) and RX Boo maser shows ~1 yr (A. Winnberg et al. 2008). These stellar variabilities and related complex maser variabilities may have significant implications for the derived results in statistical analyses.

First, simultaneous observations of various rotational transitions of SiO masers, including the SiO $J = 1$–0, $J = 2$–1, $J = 3$–2, and $J = 4$–3 transitions, using two or more receiver bands, were conducted, as reported by P. Schwartz et al. (1982). These snapshot spectra provide good constraints for constructing anSiO maser model. J. Pardo et al. (1998) observed several rotational transitions of SiO toward 12 O-rich AGB stars with the IRAM 30 m telescope. They conducted a comparative study of the SiO maser intensities and profiles. S.-H. Cho et al. (1998, 2009) and J. Kang et al. (2006) presented simultaneous observational results for the SiO $J = 2$–1 and $J = 3$–2 transitions toward 42 O-rich stars with the TRAO (Taeduk Radio Astronomy Observatory) 14 m telescope. The intensity ratios within the vibrational and rotational states were reported. They also reported that the velocity patterns of the $v = 1$, $J = 3$–2 masers, including the line profile and peak velocity variations, are somewhat different from those of the $v = 1$, $J = 2$–1, implying different tracing regions. Recently, M. C. Stroh et al. (2018) performed quasi-simultaneous observations of the SiO $J = 1$–0 and $J = 2$–1 masers toward 86 BAaDE (Bulge Asymmetries and Dynamical Evolution) sources with ATCA (Australia Telescope Compact Array). Their results showed that the intensity of the SiO $v = 1$, $J = 1$–0 maser is, on average, 1.3 times stronger than the SiO $v = 1$, $J = 2$–1 maser and is, on average, about twice as bright as the SiO $v = 1$, $J = 2$–1 maser for sources with a detectable SiO $v = 3$, $J = 1$–0 maser. J. R. Rizzo et al. (2021) provided homogeneous data for SiO, ^{29}SiO, and ^{30}SiO lines for $J = 1$–0 to $J = 5$–4 and $v = 0$ to $v = 6$ in 67 O-rich stars that could serve as the basis for making a SiO maser model. On the other hand, simultaneous observations of SiO and 22 GHz H_2O masers were performed toward about 750 M-type O-rich AGB and 160 post-AGB stars by the Korean VLBI Network (KVN) evolved star team using the early stage of KVN single-dish telescopes, which are equipped with both 22 and 43 GHz band receivers (J. Kim et al. 2010, 2012, 2014; S.-H. Cho & J. Kim 2012; D.-H. Yoon et al. 2014; C.-Y. Cho et al. 2017). J. Kim et al. (2010) conducted the first simultaneous observational survey of 166 sources detected with both H_2O and SiO masers. After that, S.-H. Cho & J. Kim (2012) and J. Kim et al. (2012) performed these surveys toward known SiO maser detected sources without H_2O maser detections and H_2O maser detected sources without SiO masers, respectively. In addition, C.-Y. Cho et al. (2017) performed survey observations of 252 OH/IR stars. Based on these observational data, they performed a statistical analysis. As a result, the observations indicate that there are differences in the fundamental emission characteristics of the SiO and H_2O masers associated with SRs, Miras, and OH/IRs, implying connectivity with different evolutionary phases. Although it was a limited sample for post-AGB stars, the results revealed different characteristics of the maser emission in the IRAS two-color diagram (W. van der Veen & H. Habing 1988) distinguishable from those of AGB stars (D.-H. Yoon et al. 2014).

The current KVN was improved to a four-band simultaneous observational system with 22/43/86/129 GHz, adding 86/129 GHz band receivers from 2012, recently upgraded to a wide-band system utilizing a new sampler Optically Connected Transmission system for Analog to Digital Conversion (OCTAD). As a result, in addition to the five existing 22 GHz H_2O and 43/42/86/129 GHz SiO masers ($v = 1, 2$, $J = 1$–0; $v = 1$, $J = 2$–1, $J = 3$–2), nine additional SiO transition lines, and five other thermal molecular lines can be observed at the same time (details in Section 2). This allows for a more accurate characterization of the 86/129 GHz SiO masers, which originate slightly farther out from the stellar atmosphere compared to the 43/42 GHz SiO masers, as confirmed by KVN VLBI observations (D.-H. Yoon et al. 2018). In particular, we need to consider the properties of the 129 GHz SiO maser, which can be pumped by both radiation and collision and influenced by an interaction with the inner dust layer. Therefore, this upgraded KVN four-band receiving system led us to start the Simultaneous Multi-mAser Survey Toward Evolved Stars (SMASTES) project. We aim to statistically analyze the changes in the SiO and H_2O maser properties during the transition from AGB to post-AGB stellar evolution. The entire SMASTES project consists of three projects. SMASTES–I focuses on 155 M-type O-rich AGB stars (this paper), which follow the evolutionary process from SRs to Miras and OH/IR stars. SMASTES–II focuses on 150 S-type AGB stars (S.-M, Son et al. 2025, in preparation), and SMASTES–III focuses on 150 post-AGB stars (S.-M. Son et al. 2025, in preparation). The results of SMASTES–I, which focused on O-rich stars exhibiting both SiO and H_2O masers, will serve as a benchmark for comparative studies of maser properties in S-type and post-AGB stars. Through SMASTES–I, we investigated the variations in maser properties between H_2O and SiO masers, including various SiO transition lines according to the evolutionary phase of SRs, Miras, and OH/IR stars. In this paper, we present the source selection and observation methods in Section 2. Observational results are given in Section 3. Section 4 provides a discussion on the observational results: Ratios of the peak and integrated flux densities between SiO and H_2O masers are given in Section 4.1; different characteristics in various SiO transition masers according to the evolutionary phases of the SR, Mira, and OH/IR stars are given in Section 4.2, and investigation of the kinematics and variations of the maser properties in the IRAS two-color diagram is given in Sections 4.3 and 4.4. We summarize in Section 5.

2. Source Selection and Observations

2.1. Source Selection

Table 1 presents 155 selected target sources based on the observation results using the 22/43 GHz band receivers of the

Table 1
Observed Target Sources List

No.	Source (type)	R.A. (J2000) (h:m:s)	Decl. (J2000) (d:m:s)	Spectral Type	Period (Days)	V_* (km s^{-1})	T_A^* (peak)(K) SiO $v = 1$, $J = 1$–0	T_A^* (peak)(K) H_2O	References
(1)	(2)	(3)	(4)	(5)	(6)	(7)	(8)	(9)	(10)
1	Y Cas (Mira)	00 03 21.461	+55 40 52.03	M6e-M8.5e	413.5	−15.6	4.61	1.02	(a)
2	SY Scl (Mira)	00 07 36.243	−25 29 39.97	M6e-M8:	411.0	22.7	0.25	1.45	(a)
3	WX Psc (OH/IR)	01 06 25.988	+12 35 52.90	M9:	660.0	8.5	8.33	4.17	(a)
4	V465 Cas (SR)	01 18 13.884	+57 48 11.40	M3	60.0	−16.2	<0.03	<0.02	(d)
5	V669 Cas (OH/IR)	01 33 51.210	+62 26 53.20	M:	1995.0	−55.0	0.25	<0.14	(a)
6	SV Psc (SR)	01 46 35.344	+19 05 04.54	M5	102.0	16.0	<0.19	0.66	(d)
7	V370 And (SR)	01 58 44.326	+45 26 06.91	M7III	228.0	2.6	0.17	<0.11	(a)
8	omi Cet (Mira)	02 19 20.792	−02 58 39.50	M5e-M9e	332.0	46.5	5.44	0.62	(a)
9	YY Ari (SR)	02 43 16.475	+22 03 34.95	M8-M9	184.0	−42.4	<0.11	0.24	(c)
10	Z Eri (SR)	02 47 55.922	−12 27 38.32	M4III	80.0	−12.3	<0.04	<0.03	(d)
11	T Ari (SR)	02 48 19.740	+17 30 33.77	M6e-M8e	340.0	7.1	<0.10	0.18	(a)
12	OH138.0+7.2 (OH/IR)	03 25 08.406	+65 32 07.06	⋯	1350.0	−37.0	0.52	<0.11	(e)
13	IK Tau (Mira)	03 53 28.892	+11 24 21.90	M6e-M10e	470.0	34.3	52.52	2.57	(a)
14	WZ Eri (Mira)	04 02 08.838	−13 44 55.28	M8.5	400.0	9.3	0.79	0.40	(a)
15	IR Per (SR)	04 20 03.166	+41 03 50.11	M6.5	175.0	−25.8	0.21	<0.07	(c)
16	R Tau (Mira)	04 28 18.003	+10 09 44.80	M5e-M9e	320.9	14.7	0.49	2.76	(a)
17	IU Tau (SR)	04 35 57.210	+28 30 52.40	M7	418.0	−1.2	0.10	<0.04	(d)
18	RX Tau (Mira)	04 38 14.568	+08 20 09.29	M6e-M7e	331.8	−43.0	3.80	1.65	(a)
19	BX Eri (SR)	04 40 32.767	−14 12 02.53	M2-M7	165.0	0.4	0.36	0.83	(a)
20	BZ Tau (SR)	04 42 21.285	+06 52 40.07	M4-M7	400.0	11.4	5.99	0.35	(e)
21	TX Cam (Mira)	05 00 51.163	+56 10 54.04	M8-M10	557.4	10.8	3.45	<0.22	(b)
22	NV Aur (Mira)	05 11 19.451	+52 52 33.24	M10	635.0	3.0	2.50	17.35	(a)
23	RX Lep (SR)	05 11 22.872	−11 50 56.72	M6.2III	60.0	46.1	<0.03	<0.03	(d)
24	IRAS 05131+4530 (OH/IR)	05 16 47.474	+45 34 04.14	⋯	⋯	−31.1	<0.11	<0.07	(e)
25	BW Cam (Mira)	05 19 52.147	+63 15 54.96	M9	⋯	51.0	1.93	0.61	(a)
26	GP Tau (SR)	05 38 32.630	+25 00 06.84	M7	90.0	−1.0	<0.18	0.30	(a)
27	RW Lep (SR)	05 38 52.735	−14 02 26.84	M4-M8III	149.9	−58.6	1.03	1.34	(c)
28	BX Cam (Mira)	05 46 44.329	+69 58 24.42	M9:	⋯	−0.9	5.81	5.48	(a)
29	S Col (Mira)	05 46 56.309	−31 41 28.37	M6e-M8	325.9	63.4	3.79	4.39	(a)
30	AW Tau (Mira)	05 47 30.209	+27 08 12.37	M9:	654.4	−4.7	0.36	1.41	(a)
31	U Ori (Mira)	05 55 49.171	+20 10 30.68	M6e-M9.5e	368.3	−37.0	14.93	1.86	(a)
32	U Lyn (Mira)	06 40 46.458	+59 52 01.54	M7e-M9.5:e	433.6	−12.9	1.95	0.61	(a)
33	IRC-10151 (OH/IR)	07 07 49.388	−10 44 06.03	M8	⋯	45.0	1.00	2.02	(a)
34	IRAS 07153-2411 (OH/IR)	07 17 27.800	−24 17 12.00	⋯	⋯	50.1	0.33	0.46	(b)
35	IRAS 07180-1314 (OH/IR)	07 20 19.541	−13 20 13.89	⋯	⋯	59.1	0.16	0.82	(d)
36	Z Pup (Mira)	07 32 38.064	−20 39 29.22	M4e-M9e	508.6	5.9	2.44	3.18	(a)
37	S Gem (Mira)	07 43 02.555	+23 26 58.14	M4e-M8e	293.2	94.6	0.43	0.87	(a)
38	R Cnc (Mira)	08 16 33.827	+11 43 34.47	M6e-M9e	361.6	16.5	4.62	0.67	(a)
39	RT Hya (SR)	08 29 41.154	−06 19 07.64	M6e-M8e	290.0	40.0	<0.03	<0.03	(d)
40	V429 Hya (SR)	08 55 43.789	−19 13 27.69	M6-M7	117.0	4.0	<0.15	0.82	(c)
41	RT Cnc (SR)	08 58 15.999	+10 50 42.68	M4III	60.0	36.0	<0.02	<0.02	(d)
42	W Cnc (Mira)	09 09 52.612	+25 14 53.79	M6.5e-M9e	393.2	35.5	0.62	0.54	(a)
43	X Hya (Mira)	09 35 30.267	−14 41 28.61	M7e-M8.5e	301.1	27.2	1.07	0.72	(a)
44	IW Hya (Mira)	09 45 15.239	−22 01 45.33	M9	650.0	39.2	10.31	1.93	(a)
45	R LMi (Mira)	09 45 34.284	+34 30 42.81	M6.5e-M9.0e	372.2	1.8	9.76	0.72	(a)
46	R Leo (Mira)	09 47 33.484	+11 25 43.82	M6e-M9.5IIIe	310.0	−0.1	11.74	<0.11	(a)
47	V Leo (Mira)	10 00 01.920	+21 15 44.36	M5e-M7e	273.4	−27.8	0.16	2.06	(c)
48	R UMa (Mira)	10 44 38.472	+68 46 32.68	M3e-M9e	301.6	38.9	3.01	9.33	(a)
49	VX UMa (Mira)	10 55 40.882	+71 52 09.63	M8e	215.2	−48.5	2.52	0.74	(a)
50	R Crt (SR)	11 00 33.853	−18 19 29.58	M7	160.0	12.8	1.32	31.25	(a)
51	ST UMa (SR)	11 27 50.378	+45 11 06.74	M4-M5III	110.0	−19.4	<0.03	<0.02	(d)
52	AF Leo (SR)	11 27 53.146	+15 08 48.41	M5(II)	107.0	9.6	<0.10	2.05	(c)
53	II Hya (SR)	11 48 45.083	−26 44 59.20	M4III	61.0	6.8	<0.28	<0.29	(c)
54	S Crt (SR)	11 52 45.098	−07 35 48.08	M6e-M7e	155.0	37.9	<0.18	4.02	(c)
55	Z UMa (SR)	11 56 30.226	+57 52 17.65	M5eIII	196.0	−53.0	<0.02	<0.02	(d)
56	T Vir (Mira)	12 14 36.680	−06 02 08.74	M6e	339.5	6.4	0.31	0.89	(a)
57	BK Vir (SR)	12 30 21.014	+04 24 59.14	M7III	150.0	18.2	0.35	<0.05	(d)
58	TU CVn (SR)	12 54 56.520	+47 11 48.20	M5III	50.0	−17.0	<0.01	<0.02	(d)
59	RT Vir (SR)	13 02 37.981	+05 11 08.36	M8III	155.0	19.3	2.01	7.75	(a)
60	SW Vir (SR)	13 14 04.383	−02 48 25.13	M7III	150.0	−10.8	<0.13	0.15	(a)
61	R Hya (Mira)	13 29 42.782	−23 16 52.77	M6e-M9eS	388.9	−8.6	21.22	0.23	(a)
62	W Hya (SR)	13 49 02.002	−28 22 03.53	M7.5e-M9ep	361.0	40.4	60.77	15.06	(a)

Table 1
(Continued)

No.	Source (type)	R.A. (J2000) (h:m:s)	Decl. (J2000) (d:m:s)	Spectral Type	Period (Days)	V_* (km s^{-1})	T_A^* (peak)(K) SiO $v = 1$, $J = 1$–0	T_A^* (peak)(K) H_2O	References
(1)	(2)	(3)	(4)	(5)	(6)	(7)	(8)	(9)	(10)
63	AY Vir (SR)	13 51 51.659	−03 40 34.03	M6	113.0	−41.1	<0.16	0.21	(c)
64	RU Hya (Mira)	14 11 34.399	−28 53 07.41	M6e-M8.8e	331.5	−1.4	0.43	0.47	(a)
65	RX Boo (SR)	14 24 11.625	+25 42 13.39	M6.5e-M8IIe	340.0	1.5	<0.17	1.57	(a)
66	RS Vir (Mira)	14 27 16.391	+04 40 41.13	M6IIIe-M8e	354.0	−12.0	1.88	3.79	(a)
67	V Boo (SR)	14 29 45.266	+38 51 40.66	M6e	257.0	−38.0	<0.03	<0.02	(d)
68	Y Cen (SR)	14 30 58.620	−30 05 51.83	M4e-M7	180.0	−6.0	<0.04	<0.04	(d)
69	RR UMi (SR)	14 57 35.007	+65 55 56.86	M4.5III	43.0	7.0	<0.03	<0.02	(d)
70	Y Lib (Mira)	15 11 41.306	−06 00 41.34	M5e-M8.2e	275.7	14.6	0.46	1.77	(a)
71	S CrB (Mira)	15 21 23.955	+31 22 02.58	M6e-M8e	360.3	−0.8	1.53	1.69	(a)
72	WX Ser (Mira)	15 27 47.042	+19 33 51.67	M8e	425.1	7.3	1.19	2.98	(a)
73	RR CrB (SR)	15 41 26.228	+38 33 26.60	M5III	61.0	−50.0	<0.031	<0.02	(d)
74	BG Ser (Mira)	15 43 36.774	−01 42 37.67	M6e-M8e	143.0	−1.3	1.05	0.91	(a)
75	FS Lib (Mira)	16 00 23.768	−12 20 57.33	M8.1-M9.0	415.0	−2.7	0.57	1.88	(a)
76	OH345.0+15.7 (OH/IR)	16 06 08.363	−30 49 33.99	M	⋯	−3.0	0.68	<0.18	(a)
77	U Her (Mira)	16 25 47.472	+18 53 32.86	M6.5e-M9.5e	406.1	−14.6	2.94	2.30	(a)
78	R UMi (SR)	16 29 57.892	+72 16 49.17	M7IIIe	325.7	−5.6	0.32	0.59	(a)
79	T Oph (Mira)	16 33 43.549	−16 07 54.24	M6.5e	366.8	−32.0	1.81	0.85	(b)
80	V446 Oph (SR)	16 46 39.118	−11 38 53.05	M4-M8III	341.0	8.3	3.47	0.40	(b)
81	AH Dra (SR)	16 48 16.635	+57 48 49.35	M7	158.0	63.0	<0.025	<0.031	(d)
82	IRAS 16486–3014 (OH/IR)	16 51 49.400	−30 19 50.00	⋯	⋯	50.9	0.92	0.26	(e)
83	V2108 Oph (SR)	17 14 19.380	+08 56 02.85	M7-M9.8	⋯	16.9	5.84	4.04	(a)
84	V438 Oph (SR)	17 14 39.782	+11 04 09.97	M0-M7e	169.0	9.0	<0.09	0.13	(c)
85	RV Ser (Mira)	17 17 50.486	−11 59 33.14	M4IIIe-M8	269.9	3.9	0.34	2.09	(c)
86	OH358.23+0.11 (OH/IR)	17 40 54.139	−30 22 38.06	⋯	⋯	−10.0	0.75	4.17	(c)
87	IRAS 17436-1545 (OH/IR)	17 46 33.654	−15 46 56.14	⋯	⋯	13.8	0.46	0.25	(e)
88	OH13.1+5.1 (OH/IR)	17 55 45.053	−15 03 42.82	M;	707.0	−65.0	<0.08	<0.05	(b)
89	VV Sgr (Mira)	17 57 03.066	−19 20 16.17	M8e	401.0	55.1	0.48	4.00	(e)
90	OH4.5-0.4 (OH/IR)	17 57 37.206	−25 12 58.67	⋯	⋯	−123.5	0.48	<0.11	(e)
91	WY Her (Mira)	18 00 03.917	+23 35 36.95	M5e-M7e	376.0	4.4	0.55	0.94	(c)
92	V4120 Sgr (Mira)	18 03 56.531	−20 19 00.52	M8+:	⋯	10.8	7.98	4.56	(a)
93	IRAS 18034-2441 (OH/IR)	18 06 29.526	−24 40 47.79	⋯	⋯	5.5	0.75	0.58	(e)
94	IRAS 18035-2529 (OH/IR)	18 06 37.750	−25 29 27.73	⋯	⋯	4.1	0.28	<0.12	(e)
95	V2302 Oph (Mira)	18 09 18.550	+09 12 15.35	M	⋯	−14.8	0.73	1.07	(a)
96	IRAS 18099+3127 (OH/IR)	18 11 47.500	+31 28 19.86	⋯	⋯	23.9	0.43	0.13	(e)
97	IRAS 18172–2305 (OH/IR)	18 20 19.300	−23 03 51.00	⋯	⋯	6.6	0.13	0.18	(e)
98	V2571 Oph (SR)	18 29 34.580	+03 28 11.69	⋯	206.1	−38.0	0.30	0.25	(c)
99	V1111 Oph (Mira)	18 37 19.258	+10 25 42.49	M4III-M9	⋯	−31.7	11.52	2.70	(a)
100	IRAS 18395+0130 (OH/IR)	18 42 03.100	+01 33 15.00	⋯	⋯	48.6	0.08	<0.08	(e)
101	RW Lyr (Mira)	18 45 10.142	+43 38 07.77	M7e	503.8	−18.9	0.71	0.41	(a)
102	V439 Sct (OH/IR)	18 45 48.434	−04 00 46 329	⋯	627.0	46.8	0.35	0.28	(e)
103	IRAS 18476+0555 (OH/IR)	18 50 04.744	+05 59 28.82	⋯	⋯	50.3	1.35	0.44	(b)
104	IRAS 18525+0210 (OH/IR)	18 55 05.148	+02 14 42.59	⋯	⋯	70.2	0.52	<0.13	(e)
105	R Lyr (SR)	18 55 20.102	+43 56 45.93	M5III	46.0	−28.0	<0.02	<0.02	(d)
106	V1366 Aql (OH/IR)	18 58 30.095	+06 42 57.696	⋯	1424.0	20.4	1.57	0.71	(a)
107	IRAS 18578+0831 (OH/IR)	19 00 17.366	+08 35 31.38	⋯	⋯	48.8	0.15	<0.09	(e)
108	IRAS 19010+1307 (OH/IR)	19 03 21.510	+13 12 01.20	⋯	⋯	59.8	0.30	<0.12	(e)
109	V1367 Aql (OH/IR)	19 04 09.749	+06 13 16.40	⋯	823.0	148.8	<0.06	<0.07	(e)
110	OH43.9+1.2 (OH/IR)	19 06 42.891	+10 14 32.35	⋯	⋯	50.0	<0.08	<0.04	(c)
111	V3880 Sgr (Mira)	19 08 54.925	−22 14 18.60	M8:	510.0	22.7	0.97	0.73	(a)
112	OH43.8+0.5 (OH/IR)	19 09 31.858	+09 51 48.45	⋯	⋯	9.0	0.15	0.12	(c)
113	IRAS 19081+0322 (OH/IR)	19 10 36.700	+03 27 02.31	⋯	⋯	41.5	<0.11	<0.14	(e)
114	IRAS 19183+1148 (OH/IR)	19 20 42.591	+11 54 04.54	⋯	⋯	34.4	<0.11	<0.09	(e)
115	OH12.11-17.19 (OH/IR)	19 20 55.757	−26 14 35.55	M9	⋯	5.0	2.07	<0.06	(d)
116	IRAS 19186+0315 (OH/IR)	19 21 11.714	+03 20 57.82	M	460.0	−22.0	0.33	0.12	(c)
117	OH44.79-2.31 (OH/IR)	19 21 36.636	+09 27 56.69	M	552.0	−67.0	2.36	<0.15	(a)
118	OH49.8-0.8 (OH/IR)	19 26 02.240	+14 36 39.30	⋯	⋯	75.6	0.19	<0.13	(e)
119	IRAS 19261+1435 (OH/IR)	19 28 28.480	+14 41 52.20	⋯	⋯	48.3	0.15	<0.10	(e)
120	IRAS 19265+3116 (OH/IR)	19 28 31.195	+31 22 24.85	⋯	⋯	31.0	0.16	0.27	(e)
121	OH55.0+0.7 (OH/IR)	19 30 29.475	+19 50 41.04	M	⋯	27.0	<0.09	<0.07	(b)
122	OH63.5+5.3 (OH/IR)	19 30 50.323	+29 29 57.32	⋯	⋯	−39.0	0.15	<0.09	(a)
123	UV Cyg (SR)	19 31 13.280	+43 38 13.60	M6-M8	135.5	22.6	0.28	2.64	(c)

Table 1
(Continued)

No.	Source (type)	R.A. (J2000) (h:m:s)	Decl. (J2000) (d:m:s)	Spectral Type	Period (Days)	V_* (km s^{-1})	T_A^* (peak)(K) SiO $v = 1$, $J = 1$–0	T_A^* (peak)(K) H_2O	References
(1)	(2)	(3)	(4)	(5)	(6)	(7)	(8)	(9)	(10)
124	RT Aql (Mira)	19 38 01.604	+11 43 18.23	M6e-M8e	327.1	−30.2	1.51	1.98	(a)
125	IRAS 19395+1827 (OH/IR)	19 41 44.549	+18 34 25.71	⋯	⋯	−0.5	0.18	0.32	(e)
126	IRAS 19422+3506 (OH/IR)	19 44 07.001	+35 14 08.31	M7.5III	⋯	−49.0	1.31	0.82	(c)
127	OH65.5+1.3 (OH/IR)	19 51 21.200	+29 13 01.30	⋯	⋯	−21.0	0.25	0.61	(a)
128	IRAS 19495+0835 (OH/IR)	19 51 57.714	+08 42 54.69	⋯	⋯	45.0	0.67	0.52	(c)
129	RR Aql (Mira)	19 57 36.062	−01 53 11.34	M6e-M9	394.8	29.1	11.16	4.27	(a)
130	IRAS 19579+3223 (OH/IR)	19 59 51.339	+32 32 09.97	M9p	315.0	5.5	0.69	0.22	(e)
131	Z Cyg (Mira)	20 01 27.508	+50 02 32.63	M5e-M9e	263.7	−151.6	0.44	1.37	(a)
132	V718 Cyg (SR)	20 03 05.119	+30 20 12.83	M0-M5	264.0	23.7	0.14	0.54	(c)
133	IRAS 20043+2653 (OH/IR)	20 06 22.738	+27 02 10.63	⋯	⋯	−5.0	0.09	<0.06	(d)
134	SY Aql (Mira)	20 07 05.406	+12 57 06.22	M5e-M7e	355.9	−44.5	0.16	1.24	(a)
135	AC Cyg (SR)	20 12 49.807	+49 27 03.14	M7-M8	142.0	−42.0	<0.06	0.06	(c)
136	IRAS 20123+0429 (OH/IR)	20 14 50.305	+04 38 56.31	⋯	⋯	−17.7	0.23	0.36	(e)
137	T Mic (SR)	20 27 55.190	−28 15 39.80	M6e	347.0	26.8	0.21	<0.07	(b)
138	OH63.3–10.2 (OH/IR)	20 28 57.098	+21 15 37.03	⋯	⋯	−72.8	1.36	0.21	(e)
139	RU Cap (Mira)	20 32 34.093	−21 41 25.58	M9e	347.4	7.3	0.42	0.62	(a)
140	IRAS 20381+5001 (OH/IR)	20 39 39.510	+50 12 16.39	M	570.0	−38.0	1.74	0.51	(d)
141	IRAS 20403+3700 (OH/IR)	20 42 18.501	+37 11 41.00	⋯	⋯	−51.0	0.83	0.30	(c)
142	OH73.8-6.3 (OH/IR)	20 42 20.481	+31 54 30.33	⋯	⋯	−15.2	0.12	<0.08	(e)
143	V Aqr (SR)	20 46 49.362	+02 26 15.24	M6e	249.1	−28.0	<0.07	0.12	(c)
144	OH83.42-0.89 (OH/IR)	20 50 58.624	+42 48 11.51	⋯	⋯	−39.0	1.02	1.24	(c)
145	V363 Cep (SR)	21 27 31.393	+71 48 59.85	M5	⋯	−32.2	1.84	0.11	(d)
146	W Cyg (SR)	21 36 02.496	+45 22 28.53	M4III	131.0	−14.0	<0.03	<0.02	(d)
147	TU Peg (Mira)	21 45 04.599	+12 41 54.98	M7e-M8e	321.6	10.1	0.44	0.48	(a)
148	EP Aqr (SR)	21 46 31.849	−02 12 45.93	M8III	55.0	−41.0	0.19	<0.10	(a)
149	SV Peg (SR)	22 05 42.084	+35 20 54.56	M7	144.6	3.5	<0.19	3.65	(a)
150	CU Cep (SR)	22 11 31.884	+57 02 17.47	M4-M6	700.0	−46.2	1.45	0.16	(c)
151	OH104.9+2.4 (OH/IR)	22 19 27.480	+59 51 21.70	⋯	1215.0	−26.0	<0.16	<0.08	(a)
152	V627 Cas (Mira)	22 57 40.972	+58 49 12.53	M2eII-III	⋯	−52.0	3.90	1.13	(a)
153	R Peg (Mira)	23 06 39.166	+10 32 36.08	M6e-M9e	378.1	23.4	3.90	1.72	(a)
154	BU And (Mira)	23 23 39.892	+39 43 37.03	M7e	378.0	−4.6	2.14	0.34	(a)
155	R Cas (Mira)	23 58 24.868	+51 23 19.71	M6e-M10e	430.5	24.7	26.00	2.27	(a)

Note. (a) J. Kim et al. (2010), (b) S.-H. Cho & J. Kim (2012), (c) J. Kim et al. (2012), (d) D.-H. Yoon et al. (2014), (e) C.-Y. Cho et al. (2017). The conversion factors from antenna temperatures (T_A^*) to flux density (Jy) are as follows: (a) 11.07 Jy K^{-1} at 22 GHz and 11.55 Jy K^{-1} at 43 GHz; (b) 11.07 Jy K^{-1} at 22 GHz and 11.72 Jy K^{-1} at 43 GHz; (c) 12.27 Jy K^{-1} at 22 GHz and 11.90 Jy K^{-1} at 43 GHz; (d) 12.40 Jy K^{-1} at 22 GHz and 12.90 Jy K^{-1}, 13.51 Jy K^{-1}, 13.29 Jy K^{-1} at 43 GHz; and (e) 12.27 Jy K^{-1} at 22 GHz and 11.90 Jy K^{-1} at 43 GHz. The information from columns 3 to 9 corresponds to the values of the references in column 10. V_*: stellar velocity.

(This table is available in machine-readable form in the online article.)

KVN in its early stages. The highest priority sources were those in which both SiO and H_2O masers were detected together, and the next priority were sources in which either SiO or H_2O maser emission was relatively strong (SiO $\geqslant$ 0.1K and H_2O $\geqslant$ 0.5K). Additionally, 15 SRs and 8 OH/IR stars that were not detected in the previous KVN observation dates were selected to fit the 50 sample each, because these sources may be detected in this observation at a different stellar phase. Thus, 71 sources were selected from J. Kim et al. (2010), 8 from S.-H. Cho & J. Kim (2012), 26 from J. Kim et al. (2012), 23 from D.-H. Yoon et al. (2014), and 27 from C.-Y. Cho et al. (2017). As another statistical selection criterion, the target sources were organized into about 50 sources according to SRs, Miras, and OH/IR stars and into the distribution regions of the IRAS two-color diagram. As a result, 155 target sources were selected, consisting of 50 SRs, 55 Miras, and 50 OH/IR stars. These sources were distributed evenly across the IRAS two-color diagram regions I, II, IIIa, IIIb, and VII, considering their evolutionary stages on the IRAS two-color diagram (W. van der Veen & H. Habing 1988) as shown in Section 4.4.

Table 1 presents the source identification numbers and names in columns (1) and (2), while columns (3) and (4) display the R.A. and decl. coordinates, indicating the position of each star. Columns (5) through (7) provide the spectral type, stellar period, and stellar velocity. Additionally, columns (8) and (9) present the peak antenna temperatures of SiO $v = 1$, $J = 1$–0, and H_2O masers, which were obtained from previous KVN observations, as referenced in column (10). The note specifies the conversion factor used to convert the peak antenna temperatures to peak flux densities.

2.2. Observations

We observed the selected 155 M-type O-rich AGB stars (Table 1) with three KVN 21 m single-dish telescopes from

Table 2
Frequency Setting

Stream No. # (1)	Rest Freq. (MHz) (2)	Molecular Transition (3)	Bandwidth (4)	Abbreviation (5)	T_{sys} (K) (6)	Velocity Resolution (km s^{-1}) (7)	Channel (8)
#1	22235.080	H_2O $J_{Ka,Kc} = 6_{16}$–5_{23}	64 MHz	H_2O	64 ∼ 200	0.21	4096
#2	22482.548	SO_2 $v = 0$, $J_{Ka,Kc} = 24_{4,20}$–$23_{5,19}$	64 MHz	SO2	⋯	⋯	4096
#3	42373.427	^{30}SiO $v = 0$, $J = 1$–0	64 MHz	^{30}SiO01	⋯	⋯	4096
#4	42519.340	SiO $v = 3$, $J = 1$–0	64 MHz	SiO31	⋯	⋯	4096
#5	42820.480	SiO $v = 2$, $J = 1$–0	64 MHz	SiO21	⋯	⋯	4096
#6	42879.820	^{29}SiO $v = 0$, J=1–0	64 MHz	^{29}SiO01	⋯	⋯	4096
#7	43122.030	SiO $v = 1$, $J = 1$–0	64 MHz	SiO11	67 ∼ 258	0.11	4096
#8	43423.760	SiO $v = 0$, $J = 1$–0	64 MHz	SiO01	⋯	⋯	4096
#9	48990.955	CS $v = 0$, $J = 1$–0	64 MHz	CS	⋯	⋯	4096
#10	85640.460	SiO $v = 2$, $J = 2$–1	64 MHz	SiO22	⋯	⋯	8192
#11	85759.199	^{29}SiO $v = 0$, $J = 2$–1	64 MHz	^{29}SiO02	⋯	⋯	8192
#12	86093.950	SO $v = 0$, $N_J = 2_2$–1_1	64 MHz	SO	⋯	⋯	8192
#13	86243.370	SiO $v = 1$, $J = 2$–1	64 MHz	SiO12	150 ∼ 360	0.05	8192
#14	86846.960	SiO $v = 0$, $J = 2$–1	64 MHz	SiO02	⋯	⋯	8192
#15	88631.602	HCN $v = 0$, $J = 1$–0	64 MHz	HCN	⋯	⋯	8192
#16	90771.564	SiS $v = 0$, $J = 5$–4	64 MHz	SiS	⋯	⋯	8192
#17	128458.887	SiO $v = 2$, $J = 3$–2	64 MHz	SiO23	⋯	⋯	8192
#18	129363.240	SiO $v = 1$, $J = 3$–2	64 MHz	SiO13	110 ∼ 480	0.036	8192
#19	130268.610	SiO $v = 0$, $J = 3$–2	64 MHz	SiO03	⋯	⋯	8192

Note. T_{sys} : System noise temperature.

2023 March to 2023 May, except SY Scl (#2), Z Eri (#10), and II Hya (#53) in 2023 September and NV Aur (#22) in 2023 October. The recently upgraded KVN four wide-band (22/43/96/129 GHz) receiving system (KVN 2023 Status Report)[4] enables us to carry out simultaneous observations of H_2O and SiO multi-maser lines together with several molecular thermal lines, in other words, 19 molecular lines in total. The frequency setup, lines, and rest frequencies are configured as provided in Table 2. For the backend system, the KVN is equipped with a data acquisition system (DAS) comprising four gigabit samplers, a digital filter bank (DFB), and a digital spectrometer (DSM). Additionally, it features a recently installed wide-band sampler (OCTAD) and a graphics processing unit (GPU) spectrometer (GSM). To facilitate our observations, the K-band and one Q-band line were assigned to the DAS+DSM, while the remaining 16 streams were allocated to the OCTAD+GSM (Table 2). The bandwidths of 64 MHz cover the range of radial velocities of 850 km s^{-1} (at 22 GHz), 440 km s^{-1} (at 43 GHz), 220 km s^{-1} (at 86 GHz), and 150 km s^{-1} (at 129 GHz). The velocity resolutions correspond to 0.21 km s^{-1} (4096 channels at 22 GHz), 0.11 km s^{-1} (4096 channels at 43 GHz), 0.05 km s^{-1} (8192 channels at 86 GHz), and 0.036 km s^{-1} (8192 channels at 129 GHz) as shown in Table 2. The velocity resolution for all four bands was uniformly smoothed to approximately 0.4 km s^{-1} to better distinguish the real emissions from noise during the data reduction. We adopted the position–switching mode with a 1 minute ON/OFF source time. Pointing was checked every 2 hr using the target sources themselves or nearby strong SiO maser sources. The half power beam widths (HPBW), aperture efficiencies, and conversion factors of the KVN Yonsei 21 m radio telescope (hereafter KYS), KVN Ulsan 21 m radio telescope (hereafter KUS), and KVN Tamna 21 m radio telescope (hereafter KTN) are given in Table 3 (KVN 2023 Status Report). The integration time was 100 ∼ 120 minutes per source to achieve 0.06–0.09 K (0.81 ∼ 1.23 Jy) as the minimum detection level of the signal-to-noise ratio (SNR) ∼ 3. The conversion factors from the antenna temperature, T_A^*, to the flux density of the KYS, KUS, and KTN are given in Table 3. Data reduction was performed using Continuum and Line Analysis Single-dish Software (CLASS) from the Grenoble Image and Line Data Analysis Software (GILDAS)[5] package.

3. Observational Results

Table 4 presents the overall results of a H_2O and three strong maser transitions of SiO $v = 1, 2$, $J = 1$–0, and $v = 1$, $J = 2$–1 (hereafter, SiO11, SiO21, and SiO12, as shown in Table 2). For comparison with previous KVN observational results using 22/43 GHz band receivers, Table 5 presents the results of the H_2O, SiO11, and SiO21 masers. As shown in Table 4, the detection rate ranking of the H_2O and SiO masers is as follows: Miras rank first, followed by OH/IR stars, and SRs rank last, as shown in the previous observational results in Table 5. There are no H_2O-only detected sources without SiO maser detections in the Miras and OH/IR stars, whereas there are five sources in the SRs shown in Table 4. Additionally, unlike the Miras and OH/IR stars, in the case of the SRs, there are 13 sources in this observation where neither H_2O nor SiO masers were detected. The undetected 13 SRs are V465 Cas (#4), Z Eri (#10), RT Cnc (#41), ST UMa (#51), II Hya (#53), TU CVn (#58), V Boo (#67), RR UMi (#69), RR CrB (#73), R Lyr (#105), and W Cyg (#146). The inclusion of the SiO12 maser by the KVN four-band receiving system led us to change the detection rates among the SRs, as shown in Tables 4 and 5. Two SRs (AF Leo (#52) and S Crt (#54)) were newly detected as both H_2O and SiO maser sources

[4] https://radio.kasi.re.kr/status_report.php

[5] https://www.iram.fr/IRAMFR/GILDAS/

Table 3
HPBW, Aperture Efficiency, and Conversion Factor

Site	Band (GHz)	HPBW (arcsec)	$A_{\rm eff}$ (%)	C.F (Jy K^{-1})	Backend
(1)	(2)	(3)	(4)	(5)	(6)
	22	130	65	12.21	DAS+DSM
	43	67	71	11.30	···
	43	67	72	11.10	···
KYS	49	61	57	14.10	···
	86	32	54	14.90	···
	88	32	49	16.35	OCTAD+GSM
	90	31	53	14.96	···
	128	25	38	20.93	···
	130	25	37	21.76	···
	22	129	69	11.58	DAS+DSM
	43	65	64	12.54	···
	43	67	65	14.40	···
KUS	49	59	52	17.72	···
	86	32	67	15.45	···
	88	31	60	17.00	OCTAD+GSM
	90	31	67	15.36	···
	128	23	46	19.13	···
	130	23	46	19.12	···
	22	128	70	11.40	DAS+DSM
	43	64	64	12.53	···
	43	68	64	12.45	···
KTN	49	57	52	15.42	···
	86	31	59	13.47	···
	88	31	55	14.40	OCTAD+GSM
	90	32	58	13.78	···
	128	23	42	19.12	···
	130	22	42	18.91	···

Note. Aperture efficiency = $A_{\rm eff}$, C.F. = conversion factor from antenna temperature(T_A^*) to fulx density, Ref.: KVN 2023 Status Report.

Table 4
Observational Results of H_2O, SiO11, SiO21, and SiO12 Masers

Source	Both H_2O and SiO Detected	SiO-only detected	H_2O-only detected	Undetected
Type	Sources (%)	Sources (%)	Sources (%)	Sources (%)
(1)	(2)	(3)	(4)	(5)
SR(50)	21(42%)	11(22%)	5(10%)	13(26%)
Mira(55)	50(91%)	5(9%)	0(0%)	0(%)
OH/IR(50)	26(52%)	24(48%)	0(0%)	0(%)

compared to the previous work. Three SRs (RX Lep (#23), SW Vir (#60), and EP Aqr (#148)) were newly identified as SiO-only detected sources without H_2O maser detections. Considering stellar phase variability in the optical due to the difference in observation time, the detection rate of the H_2O, SiO11, and SiO21 masers in this work is similar to that of the previous work. Table 6 presents the overall detection results of the 19 observed molecular lines according to the source types. The H_2O and all SiO masers and thermal lines show the highest detection rate in the Miras, followed by the OH/IR stars and SRs. The SiO21 maser has the highest detection rate, exhibiting all detections from the 55 observed Miras and 50 OH/IR stars. The SiO11 maser is detected from the 54 Miras except V Leo (#47), in which both the SiO11 and H_2O masers were detected in a previous work by J. Kim et al. (2012). In the SRs, the SiO12 maser and ^{29}SiO12 line show a higher detection rate than the SiO11 maser, despite having higher excitation energies. Furthermore, in the SRb type, RT Vir (#59) and SV Peg (#149), the SiO11 maser was not detected despite the detection of the SiO21 maser shown in Figure 1. The rare SiO22 is detected from IU Tau (#17) (SR) and 3 Miras (TX Cam (#21), NV Aur (#22), and V1111 Oph (#99)) including three new detections (IU Tau (#17), NV Aur (#22), and V1111 Oph (#99)). This rare maser is usually strongly detected in S-type stars compared to M-type stars (V. Bujarrabal et al. 1996) because of the infrared line overlap between the SiO $v = 1$, $J = 0 \rightarrow v = 2$, $J = 1$ vibrational component and the H_2O $v_2 = 0$, $12_{75} \rightarrow v_2 = 1$, 11_{66} line (H. Olofsson et al. 1981, 1985), whose frequencies are very close. The SiO31 is detected from only two sources among the 50 SRs (detection rate: 4.0%) compared to the high detection rate of about 30% from the Miras and OH/IR stars. The detection rates of the SiO ground vibrational state lines of SiO01, SiO02, and SiO03 show a similar value in the OH/IR stars. However, these detection rates increase toward higher rotational transition from SiO01 to SiO03 in the SRs and Miras. In addition, they naturally appear highest in the Miras, but unlike other SiO transition lines, the detection rates appear higher in the SRs than in the OH/IR stars, as with the ^{29}SiO02 line. The detection rate of the ^{29}SiO01 line in the SRs has a lower value than that of the ^{29}SiO02 line in the OH/IR stars.

For the ground vibrational state lines of the isotopologues ^{29}SiO01 and ^{29}SiO02, and ^{30}SiO01 lines, they show the highest detection rate in the Miras among the SRs, Miras, and OH/IR stars. However, the detection rates appear differently for the types of SRs and OH/IR stars. For the ^{29}SiO02 line, the detection rate of SRs (16.0%) is somewhat higher than that of the OH/IR stars (10.0%), whereas, for the ^{29}SiO01 line, its detection rate of SRs (12.0%) is lower than that of the OH/IR stars (36.0%). For the ^{30}SiO01 line, the detection rate of SRs (4.0%) is also lower than that of the OH/IR stars (10.0%). Despite observations of O-rich AGB stars, we detected the carbon-bearing molecule HCN in 11 sources and SiS in 3 sources, which are typically found in C-rich AGB stars. The HCN line was detected in two SRs (W Hya (#62) and RX Boo (#65)), eight Miras (IK Tau (#13), TX Cam (#21), NV Aur (#22), BX Cam (#28), R Leo (#46), V4120 Sgr (#92), V1111 Oph (#99), and R Cas (#155)), and one OH/IR star (WX Psc (#3)). The SiS line was detected in one OH/IR star (WX Psc (#3)) and two Miras (IK Tau (#13) and TX Cam (#21)). Three SiS detected sources are also HCN detected sources. The presence of HCN in O-rich AGB stars is attributed to non-local thermodynamic equilibrium (LTE) conditions in the inner wind region of the circumstellar envelope (CSE) induced by shock activity due to stellar pulsation (D. Duari & J. Hatchell 2000; I. Cherchneff 2006). V. Bujarrabal (1994) detected the SiS line in TX Cam and IK Tau and derived a lower SiS abundance in O-rich stars than in C-rich stars. No detections were made for SO_2, SO, and CS lines within our observational noise rms levels of 0.19–0.27 Jy. High sensitivity ALMA data show the presence of many SO_2, SO, and CS molecular lines around O-rich AGB stars (T. Danilovich et al. 2019, 2020). Figure 1 shows the simultaneously obtained spectra of the lines from 144 sources, excluding the 11 sources from which any lines were not detected. Each spectrum is labeled with the source identification

Table 5
Observational Results of H_2O, SiO11, and SiO21 Masers Comparing with Previous Results

Source Type	Both H_2O and SiO		SiO-only detected		H_2O-only detected		Undetected	
	Detected Sources (%)		Sources (%)		Sources (%)		Sources (%)	
	Previous	This Work	Previous	This Work	Previous	This Work	Previous	This Work
(1)	(2)	(3)	(4)	(5)	(6)	(7)	(8)	(9)
SR(50)	18(36%)	19(38%)	5(10%)	8(16%)	11(22%)	7(14%)	16(32%)	16(32%)
Mira(55)	53(96%)	50(91%)	2(4%)	5(9%)	0(0%)	0(0%)	0(0%)	0(0%)
OH/IR(50)	27(54%)	26(52%)	23(46%)	24(48%)	0(0%)	0(0%)	0(0%)	0(0%)

Table 6
Detection Rate According to Source Type

Transition	SR (50) (%)	Mira (55) (%)	OH/IR (50) (%)	Total (Total Detection Rate)	Notes
(1)	(2)	(3)	(4)	(5)	(6)
H_2O $J_{Ka,Kc} = 6_{16}$–5_{23}	26 (52.0%)	50 (90.9%)	26 (52.0%)	102 (65.8%)	⋯
SiO $v = 1$, $J = 3$–2	13 (26.0%)	46 (83.6%)	23 (46.0%)	82 (52.9%)	⋯
SiO $v = 1$, $J = 2$–1	32 (64.0%)	54 (98.2%)	41 (82.0%)	127 (81.9%)	Undetected Mira : 47. V Leo
SiO $v = 1$, $J = 1$–0	24 (48.0%)	54 (98.2%)	48 (96.0%)	126 (81.3%)	Undetected Mira : 47. V Leo
SiO $v = 2$, $J = 3$–2	5 (10.0%)	25 (45.5%)	6 (12.0%)	36 (23.3%)	⋯
SiO $v = 2$, $J = 2$–1	1 (2.0%)	3 (5.5%)	⋯	4 (2.6%)	17. IU Tau, 21. TX Cam, 22. NV Aur, 99. V1111 Oph
SiO $v = 2$, $J = 1$–0	24 (48.0%)	55 (100.0%)	50 (100.0%)	129 (83.2%)	⋯
SiO $v = 3$, $J = 1$–0	2 (4.0%)	19 (34.5%)	15 (30.0%)	36 (23.2%)	⋯
SiO $v = 0$, $J = 3$–2	27 (54.0%)	38 (69.1%)	8 (16.0%)	73 (47.1%))	⋯
SiO $v = 0$, $J = 2$–1	20 (40.0%)	34 (61.8%)	7 (14.0%)	61 (39.4%)	⋯
SiO $v = 0$, $J = 1$–0	11 (22.0%)	22 (40.0%)	8 (16.0%)	41 (26.5%)	⋯
^{29}SiO $v = 0$, $J = 2$–1	8 (16.0%)	13 (23.6%)	5 (10.0%)	26 (16.8%)	⋯
^{29}SiO $v = 0$, $J = 1$–0	6 (12.0%)	21 (38.2%)	18 (36.0%)	45 (29.7%)	⋯
^{30}SiO $v = 0$, $J = 1$–0	2 (4.0%)	9 (16.4%)	5 (10.0%)	16 (10.3%)	⋯
HCN $v = 0$, $J = 1$–0	2 (4.0%)	8 (14.5%)	1 (2.0%)	11 (7.1%)	⋯
SiS $v = 0$, $J = 5$–4	⋯	2 (3.6%)	1 (2.0%)	3 (1.9%)	3. WX Psc, 13. IK Tau, 21. TX Cam
SO_2 $v = 0$, $J_{Ka,Kc} = 24_{4,20}$–$23_{5,19}$	⋯	⋯	⋯	0 (0.0%)	⋯
CS $v = 0$, $J = 1$–0	⋯	⋯	⋯	0 (0.0%)	⋯
SO $v = 0$, $N_J = 2_2$–1_1	⋯	⋯	⋯	0 (0.0%)	⋯

number and name from the first and second columns of Table 4, respectively. The molecular transitions listed in Table 1 are also displayed. The vertical dashed line indicates the stellar velocity in Table 1. However, the vertical solid line indicates the newly determined stellar velocities based on Gaussian fitting of SiO thermal lines in Table 7. Most SiO maser lines are detected near the stellar velocity, while H_2O masers often have a single peak near the stellar velocity or double peaks or single peaks with respect to the stellar velocity with red- and/or blueshifted emission. SiO ground vibrational lines (thermal) exhibit a broad parabolic emission centered at the stellar velocity, similar to the HCN and SiS thermal lines. However, the SiO01 emission consists of two components: a broad plateau and a central narrow spike as shown in WX Psc (#3), IK Tau (#13), TX Cam (#21), NV Aur (#22), BX Cam (#28), and V1111 Oph (#99). The central narrow spike is the result of weak maser emission as suggested by D. A. Boboltz & M. Claussen (2004) and P. De Vicente et al. (2016) due to its high brightness and time variability. The ^{29}SiO02 line in IK Tau (#13) shows two spike features on the broad plateau. Tables 8–14 present all the properties of the observational data. Table 8 lists the peak fluxes' 144 detected sources. Table 9 presents the integrated fluxes' 144 detected sources, and Table 10 shows the ratios of the peak and integrated fluxes compared to the SiO11 maser. Table 11 provides peak velocities, and Table 12 lists full width at zero power (FWZP) values.

Table 13 presents the best-fit periods, stellar phases, and associated errors for 56 sources calculated using available optical data from the American Association of Variable Star Observers (AAVSO) by the Lomb–Scargle periodogram method (J. T. VanderPlas 2018).

Table 14 lists noise rms values for all the 19 observed lines and the KVN telescopes used for the observations. The average noise rms values for these observations were 0.19, 0.14, 0.25, and 0.37 Jy for the *K*-, *Q*-, *W*-, and *D*-bands, with an overall average of about 0.24 Jy indicating a simultaneous and almost homogeneous data set. We selected three well–known sources from each category—SRs, Miras, and OH/IR stars—with numerous detected molecular lines and commented on them. Their positions in the IRAS two-color diagram can be confirmed in Figure 8.

3.1. Semiregular Variables

No. 50. R Crt (SR): The SR R Crt with an M7 spectral type (N. Samus' et al. 2017) is classified as a SRb, which shows uncertain or superimposed periodicities, such as one or more overtones. The line profile of the H_2O maser is composed of three

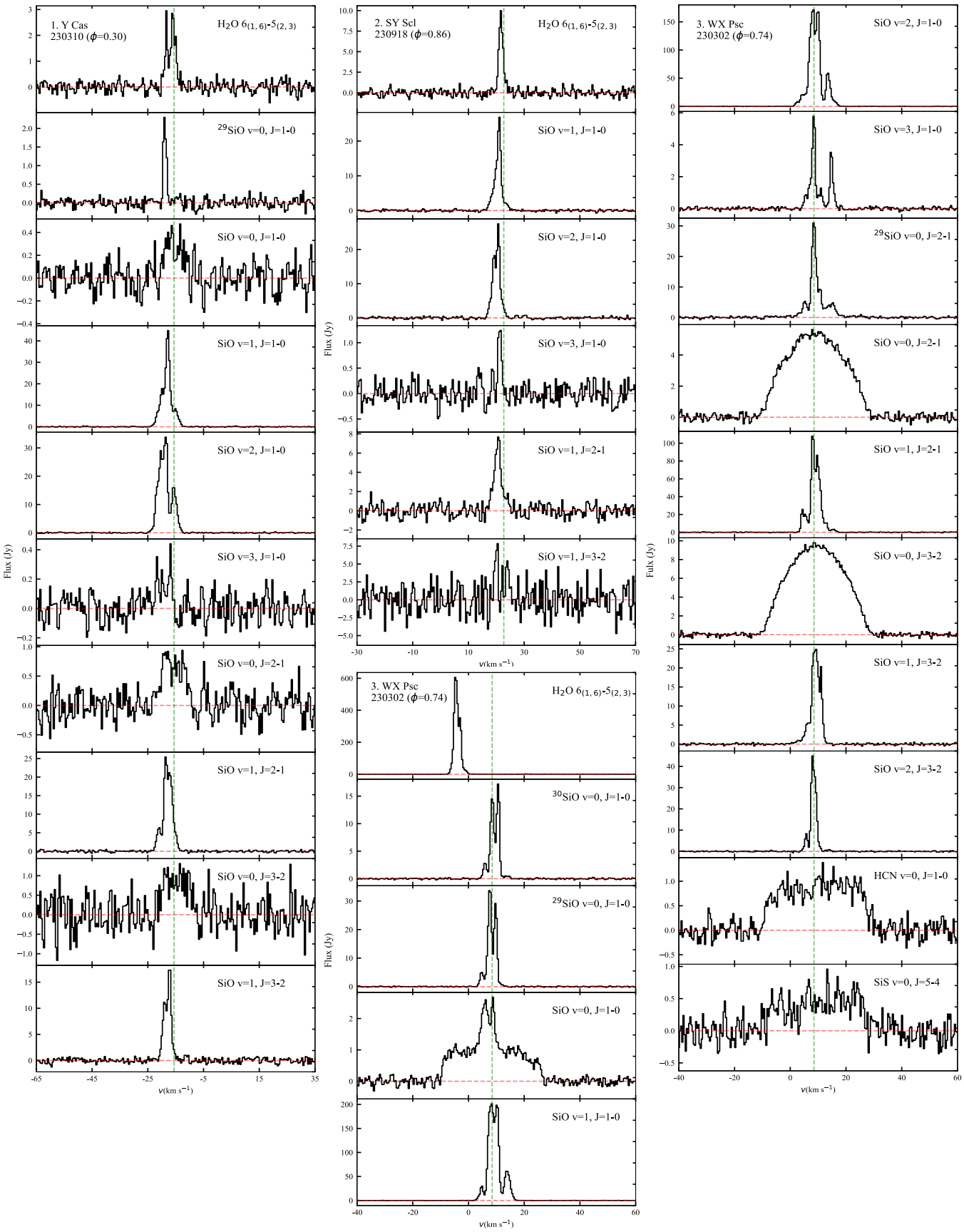

Figure 1. The spectra of 144 detected stars from simultaneous observations of 19 molecular lines. The *x*-axis indicates the velocity of the local standard of rest (V_{LSR}), and the *y*-axis indicates the flux density. The vertical dashed line marks the stellar velocity in Table 1. The vertical solid line indicates the newly determined stellar velocities based on Gaussian fitting of SiO thermal lines. The complete figure set (35 images) is available in the online journal.
(The complete figure set (34 images) is available in the online article.)

Table 7
Newly Determined Stellar Velocity for 13 Sources

No.	Source (Type)	V_* (km s^{-1})	New V_* (km s^{-1})
6	SV Psc (SR)	16.0	6.0
7	V370 And (SR)	2.6	−1.5
11	T Ari (SR)	7.1	−1.2
32	U Lyn (Mira)	−12.9	10.8
39	RT Hya (SR)	40.0	27.0
68	Y Cen (SR)	−6.0	−0.8
71	S CrB (Mira)	−0.8	1.2
78	R UMi (SR)	−5.6	−8.1
81	AH Dra (SR)	63.0	74.7
117	OH44.79-2.31 (OH/IR)	−67.0	−71.9
135	AC Cyg (SR)	−42.0	−33.0
137	T Mic (SR)	26.8	24.6
148	EP Aqr (SR)	−41.0	−33.5

Note. Column (3): existing stellar velocity from Table 1. Column (4): newly determined V_* from our observations.

components, and the peak emission at 10.4 km s^{-1} is blueshifted with respect to the stellar velocity 12.8 km s^{-1}(Figure 1). Long-term monitoring observations of the H_2O maser from 1987 to 2011 were performed by J. Brand et al. (2020). On the other hand, the peak emission of SiO11, SiO21, SiO12, and SiO13 masers is redshifted. The KVN VLBI images show that SiO masers are distributed in a ring-like structure, while the H_2O maser is distributed in a very asymmetric one-side outflow structure (D.-J. Kim et al. 2018). D.-J. Kim et al. (2018) also reported that the SiO12 maser is distributed in an inner region compared to the SiO11 maser, contrary to what is known in the distribution of the SiO12 maser.

No. 62. W Hya (SR, $\phi = 0.02$): This star is classified as a SRa-type variable with a persistent periodicity but smaller optical amplitudes (<2.5 mag in V) than the Mira variables. W Hya is one of the brightest infrared sources in the sky and is located relatively close to us (from 78 to 115 pc: G. Knapp et al. 2003; I. Glass & F. Van Leeuwen 2007; M. A. Perryman et al. 1997). The phase was calculated using optical data from the AAVSO. The peak and integrated flux ratios of the H_2O to SiO masers are very small, unlike those observed in other SRs (Peak flux density(H_2O)/Peak flux density (SiO) = 0.03, Integrated flux density(H_2O)/Integrated flux density(SiO) = 0.03). The line profile of the H_2O maser exhibits a double peak with respect to a stellar velocity of 40.4 km s^{-1} on 2023 March 26 ($\phi = 0.19$). Most SiO lines exhibit peaks around the stellar velocity, although the ^{29}SiO02 line peaks at 44.69 km s^{-1}. In the observations by J. Kim et al. (2010) on 2009 June 4 ($\phi = 0.38$), the H_2O, SiO11 and SiO21 masers were detected as a single peak near the stellar velocity. The SiO11 and SiO21 masers were detected as double peaks in our observations. Recent KVN VLBI monitoring observations show the existence of SiO12 and SiO13 maser bumps (D.-H. Yoon, in preparation).

No. 83. V2108 Oph (SR): The H_2O maser shows both blue- and redshifted components with respect to the stellar velocity in Figure 1. VLBI observations are needed to confirm a bipolar outflow from these double peaks. The redshifted component is much stronger than the blueshifted component. In comparison, the blueshifted component was somewhat stronger than the redshifted component in 2009 June (J. Kim et al. 2010). The peak emission of all SiO masers except the SiO23 maser is blueshifted with respect to the stellar velocity. The peak velocity of the SiO23 maser agrees with the stellar velocity. The SiO01, ^{29}SiO01, ^{29}SiO02, and ^{30}SiO01 lines show a typical spiky maser feature, unlike the thermal Gaussian feature of the SiO02 and SiO03 lines.

3.2. Mira Variables

No. 13. IK Tau (Mira, $\phi = 0.15$): As shown in Figure 1, an H_2O maser and 12 SiO lines, as well as HCN and SiS, were detected. The water maser exhibits two velocity components. The redshifted component peaked at 45.5 km s^{-1}, which is stronger than the blueshifted component, which peaked at 24.4 km s^{-1}. Monitoring observations from 2005 January to 2006 November by M. Shintani et al. (2008) showed that the blueshifted component was stronger than the redshifted component. According to KVN VLBI observations, in contrast to the asymmetric and bipolar outflow feature of the H_2O maser (C.-Y. Cho et al. 2017, Yun et al. 2019 KVN user's meeting), the 43/42/86/129 GHz SiO masers showed a ring–shaped image. The SiO01 and SiO02 and ^{29}SiO02 lines are composed of a wide pedestal component with a central spike due to a weak maser emission. In particular, the ^{29}SiO01 line shows a weak maser spike with a double peak with respect to the stellar velocity. In contrast, the ^{29}SiO01 and ^{30}SiO01 lines show a typical maser emission without wide pedestal components. The peak components of all the SiO masers show a blueshifted emission with respect to the stellar velocity unlike the peak of the H_2O maser.

No. 22. NV Aur (Mira): This object was observed in two epochs, 2023 September 18 and 2023 October 13 as shown in Figure 1. Therefore, we cannot obtain the optical phase. The H_2O maser was not detected on 2023 September 18 but was detected on 2023 October 13, as a redshifted weak emission peaked at 14.6 km s^{-1} (0.61 Jy). However, a one-sided blueshifted emission ($V_{LSR} = -11$ km s^{-1}) was detected with a strong intensity of 192.06 Jy on 2009 June 5 (J. Kim et al. 2010). The SiO22 rare maser was detected from NV Aur for the first time, although it is an O-rich AGB star with detected H_2O maser. Unlike IK Tau, the ^{29}SiO01 line shows a maser spike feature without a thermal pedestal.

No. 99. V1111 Oph (Mira): The H_2O maser shows four narrow spikes peaked at V_{LSR} = 40.0 km s^{-1}. On 2009 June 18, it exhibited both blueshifted and redshifted components with respect to the stellar velocity with the peak velocity at V_{LSR} = –19.7 km s^{-1}, and the blueshifted component at V_{LSR} = –39.6 km s^{-1} exhibited a thermal-like feature (J. Kim et al. 2010). Monitoring observations of the H_2O maser by M. Shintani et al. (2008) show that the redshifted component is stronger than the blueshifted component from 2003 December to 2005 March. These variations of H_2O maser lines appear to be due to changes in the bipolar outflow, which is represented by the red- and blueshifted components. However, the bipolar outflow is stronger in the direction away from the line of sight during the above observations, so the redshifted component appears stronger. A detailed confirmation would require long-term VLBI monitoring over multiple cycles. Both ^{29}SiO01 and ^{30}SiO01 lines show double peak maser features different from those of IK Tau and NV Aur. The narrow spike maser feature is not found in the ^{29}SiO02 line. The SiO22 rare maser was detected from V1111 Oph for the first time. The SiO22 maser shows a redshifted peak velocity against the SiO23 maser that appeared at the stellar velocity.

Table 8
Peak Flux Density

No.	Source	*S*(peak) (Jy)														
			^{30}SiO	^{29}SiO	SiO				^{29}SiO	SiO			SiO			
					J = 1–0					J = 2–1			J= 3–2			HCN	SiS
		H_2O	v = 0	v = 0	v = 0	v = 1	v = 2	v = 3	v = 0	v = 0	v = 1	v = 2	v = 0	v = 1	v = 2		
(1)	(2)	(3)	(4)	(5)	(6)	(7)	(8)	(9)	(10)	(11)	(12)	(13)	(14)	(15)	(16)	(17)	(18)
1	Y Cas	2.95	⋯	2.22	0.33	44.07	33.19	0.33	⋯	0.75	25.48	⋯	1.00	17.37	⋯	⋯	⋯
2	SY Scl	9.96	⋯	⋯	⋯	26.93	27.36	12.38	⋯	⋯	7.73	⋯	⋯	7.84	⋯	⋯	⋯
3	WX Psc	605.98	17.18	33.70	2.74	201.46	171.65	5.76	30.94	5.25	108.00	⋯	10.13	24.87	44.96	1.02	0.46
5	V669 Cas	⋯	⋯	⋯	⋯	⋯	9.07	⋯	⋯	⋯	1.08	⋯	⋯	⋯	⋯	⋯	⋯
6	SV Psc	⋯	⋯	⋯	⋯	⋯	⋯	⋯	⋯	1.08	⋯	⋯	1.53	⋯	⋯	⋯	⋯
7	V370 And	⋯	⋯	⋯	1.22	0.44	0.78	⋯	0.78	4.02	3.13	⋯	6.75	⋯	⋯	⋯	⋯
8	omi Cet	⋯	⋯	⋯	0.86	108.72	36.86	⋯	⋯	1.70	285.05	⋯	3.06	91.63	⋯	⋯	⋯
9	YY Ari	2.44	⋯	⋯	⋯	⋯	⋯	⋯	⋯	⋯	⋯	⋯	⋯	⋯	⋯	⋯	⋯
11	T Ari	1.10	⋯	⋯	⋯	16.43	8.33	⋯	⋯	⋯	17.14	⋯	0.65	⋯	⋯	⋯	⋯
12	OH138.0+7.2	⋯	⋯	0.72	⋯	1.01	4.61	⋯	⋯	⋯	2.16	⋯	⋯	⋯	⋯	⋯	⋯
13	IK Tau	141.25	2.51	26.15	4.36	555.15	545.68	9.84	2.16	9.16	219.97	⋯	12.67	76.29	25.81	1.58	0.55
14	WZ Eri	⋯	⋯	⋯	⋯	1.44	1.44	⋯	⋯	⋯	1.64	⋯	⋯	⋯	⋯	⋯	⋯
15	IR Per	⋯	⋯	⋯	⋯	0.37	1.99	⋯	⋯	⋯	1.21	⋯	⋯	⋯	⋯	⋯	⋯
16	R Tau	6.83	⋯	⋯	⋯	71.57	54.86	⋯	⋯	1.08	76.17	⋯	0.96	4.78	⋯	⋯	⋯
17	IU Tau	⋯	⋯	1.22	⋯	8.88	7.99	⋯	⋯	⋯	9.69	5.62	1.52	1.67	5.44	⋯	⋯
18	RX Tau	8.21	⋯	⋯	⋯	14.57	8.09	⋯	⋯	0.40	15.76	⋯	0.76	11.09	1.15	⋯	⋯
19	BX Eri	35.91	⋯	⋯	⋯	⋯	0.87	⋯	⋯	0.40	0.81	⋯	0.57	⋯	⋯	⋯	⋯
20	BZ Tau	⋯	⋯	⋯	⋯	6.91	7.34	⋯	⋯	⋯	14.37	⋯	⋯	5.55	⋯	⋯	⋯
21	TX Cam	⋯	4.63	33.08	2.89	145.74	97.90	⋯	2.19	6.71	376.37	0.62	11.32	206.37	65.30	2.62	0.30
22	NV Aur(230918)	...	1.47	7.55	1.89	58.83	56.28	6.44	4.68	1.64	28.76	2.97	2.61	7.12	20.51	0.82	⋯
	NV Aur(231013)	0.61	1.36	8.33	2.11	59.94	57.61	4.22	3.90	1.64	24.29	2.19	2.83	8.58	16.33	0.49	⋯
23	RX Lep	⋯	⋯	⋯	⋯	⋯	⋯	⋯	⋯	⋯	1.08	⋯	⋯	⋯	⋯	⋯	⋯
24	IRAS 05131+4530	⋯	⋯	⋯	⋯	3.66	4.22	⋯	⋯	⋯	⋯	⋯	⋯	⋯	⋯	⋯	⋯
25	BW Cam	7.76	0.38	1.01	0.43	40.75	46.94	0.29	⋯	1.39	21.32	⋯	1.53	2.87	1.15	⋯	⋯
26	GP Tau	11.93	⋯	⋯	⋯	5.18	1.15	⋯	⋯	⋯	5.10	⋯	⋯	⋯	⋯	⋯	⋯
27	RW Lep	35.90	⋯	⋯	⋯	4.18	4.90	⋯	⋯	⋯	7.57	⋯	⋯	⋯	⋯	⋯	⋯
28	BX Cam	8.66	1.75	3.98	1.37	30.75	28.51	0.62	0.43	1.21	51.32	⋯	3.40	26.39	17.21	0.58	⋯
29	S Col	14.48	⋯	⋯	⋯	9.50	5.33	⋯	⋯	⋯	21.78	⋯	⋯	4.78	⋯	⋯	⋯
30	AW Tau	4.56	⋯	⋯	⋯	2.49	4.98	0.25	⋯	⋯	1.75	⋯	⋯	1.34	⋯	⋯	⋯
31	U Ori	1.95	⋯	2.78	1.11	105.56	23.42	⋯	⋯	2.09	150.94	⋯	2.83	17.37	19.46	⋯	⋯
32	U Lyn	2.43	⋯	⋯	⋯	62.50	77.18	5.47	⋯	0.93	10.66	⋯	0.96	10.14	⋯	⋯	⋯
33	IRC-10151	3.30	⋯	⋯	⋯	12.77	12.88	⋯	⋯	⋯	6.56	⋯	⋯	1.67	⋯	⋯	⋯
34	IRAS 07153-2411	⋯	⋯	0.37	⋯	1.00	0.50	⋯	⋯	⋯	1.35	⋯	⋯	⋯	⋯	⋯	⋯
35	IRAS 07180-1314	4.88	⋯	0.78	⋯	8.66	7.44	0.67	⋯	⋯	3.73	⋯	⋯	⋯	⋯	⋯	⋯
36	Z Pup	13.57	⋯	⋯	0.75	28.14	16.68	⋯	⋯	0.67	17.11	⋯	0.57	4.02	4.21	⋯	⋯
37	S Gem	10.19	⋯	⋯	⋯	5.18	4.61	⋯	⋯	⋯	2.16	⋯	⋯	3.06	⋯	⋯	⋯
38	R Cnc	6.14	⋯	1.58	0.86	42.05	92.88	⋯	⋯	1.70	99.34	⋯	2.49	42.66	4.21	⋯	⋯
39	RT Hya	⋯	⋯	⋯	⋯	⋯	0.37	⋯	⋯	⋯	0.94	⋯	0.76	⋯	⋯	⋯	⋯
40	V429 Hya	4.03	⋯	⋯	⋯	⋯	⋯	⋯	⋯	0.30	⋯	⋯	⋯	⋯	⋯	⋯	⋯
42	W Cnc	2.28	⋯	⋯	⋯	23.28	19.42	⋯	⋯	0.67	30.85	⋯	1.13	19.12	⋯	⋯	⋯
43	X Hya	40.07	⋯	⋯	⋯	25.92	27.22	⋯	⋯	0.93	34.92	⋯	1.53	11.10	3.83	⋯	⋯
44	IW Hya	6.59	⋯	3.33	0.22	96.35	72.71	2.00	0.94	1.19	32.18	⋯	2.83	12.56	1.88	⋯	⋯
45	R LMi	9.46	⋯	⋯	0.50	32.37	39.22	0.25	⋯	2.29	34.08	⋯	3.78	10.13	2.10	⋯	⋯

Table 8
(Continued)

No.	Source	S(peak) (Jy)														
			^{30}SiO	^{29}SiO	SiO J = 1–0				^{29}SiO	SiO J = 2–1			SiO J= 3–2			HCN	SiS
		H_2O															
			$v = 0$	$v = 0$	$v = 0$	$v = 1$	$v = 2$	$v = 3$	$v = 0$	$v = 0$	$v = 1$	$v = 2$	$v = 0$	$v = 1$	$v = 2$		
(1)	(2)	(3)	(4)	(5)	(6)	(7)	(8)	(9)	(10)	(11)	(12)	(13)	(14)	(15)	(16)	(17)	(18)
46	R Leo	1.10	⋯	0.44	1.22	190.48	258.08	5.11	1.25	43.06	222.61	⋯	19.80	28.05	30.14	0.65	⋯
47	V Leo	⋯	⋯	⋯	⋯	⋯	1.73	⋯	⋯	⋯	⋯	⋯	⋯	⋯	⋯	⋯	⋯
48	R UMa	9.04	⋯	⋯	⋯	23.53	13.43	0.89	⋯	⋯	14.45	⋯	⋯	2.09	⋯	⋯	⋯
49	VX UMa	2.51	⋯	⋯	⋯	5.23	14.94	⋯	⋯	0.67	7.68	⋯	0.76	5.74	0.96	⋯	⋯
50	R Crt	455.66	⋯	⋯	1.12	7.22	4.86	⋯	0.86	4.85	12.12	⋯	7.94	2.49	⋯	⋯	⋯
52	AF Leo	12.31	⋯	⋯	⋯	⋯	⋯	⋯	⋯	0.27	1.08	⋯	0.95	⋯	⋯	⋯	⋯
54	S Crt	25.03	⋯	⋯	⋯	⋯	⋯	⋯	⋯	⋯	2.24	⋯	⋯	⋯	⋯	⋯	⋯
55	Z UMa	⋯	⋯	⋯	⋯	1.73	⋯	⋯	⋯	⋯	8.96	⋯	⋯	3.83	⋯	⋯	⋯
56	T Vir	14.53	⋯	⋯	⋯	4.44	4.88	⋯	⋯	⋯	7.60	⋯	⋯	⋯	⋯	⋯	⋯
57	BK Vir	1.82	⋯	⋯	0.25	1.87	1.74	⋯	⋯	1.89	12.39	⋯	3.97	⋯	⋯	⋯	⋯
59	RT Vir	58.60	⋯	⋯	0.75	11.95	0.87	⋯	0.72	4.18	16.03	⋯	8.70	3.06	⋯	⋯	⋯
60	SW Vir	⋯	⋯	⋯	1.01	⋯	⋯	⋯	1.46	5.56	11.12	⋯	10.32	⋯	⋯	⋯	⋯
61	R Hya	1.22	⋯	⋯	0.78	52.50	33.30	⋯	1.09	6.56	92.08	⋯	12.62	3.77	⋯	⋯	⋯
62	W Hya	38.91	1.13	78.48	3.31	1435.39	1269.50	27.36	11.28	23.33	1051.99	⋯	29.25	562.04	227.65	0.68	⋯
63	AY Vir	38.76	⋯	⋯	⋯	⋯	⋯	⋯	⋯	0.94	⋯	⋯	1.13	⋯	⋯	⋯	⋯
64	RU Hya	6.27	⋯	⋯	⋯	24.40	10.83	⋯	⋯	⋯	12.53	⋯	0.57	2.29	⋯	⋯	⋯
65	RX Boo	135.60	⋯	0.43	2.30	4.90	17.28	⋯	1.64	10.82	17.92	⋯	11.47	2.10	⋯	0.51	⋯
66	RS Vir	33.52	⋯	⋯	⋯	8.34	3.36	⋯	⋯	0.94	9.29	⋯	1.51	1.53	⋯	⋯	⋯
68	Y Cen	⋯	⋯	⋯	⋯	0.89	0.56	⋯	⋯	1.04	2.98	⋯	2.39	⋯	⋯	⋯	⋯
70	Y Lib	6.38	⋯	⋯	⋯	7.35	6.60	⋯	⋯	⋯	4.04	⋯	⋯	2.10	⋯	⋯	⋯
71	S CrB	9.38	⋯	⋯	3.46	7.78	35.57	⋯	⋯	2.01	10.97	⋯	3.82	⋯	⋯	⋯	⋯
72	WX Ser	43.71	⋯	⋯	⋯	36.30	21.98	⋯	⋯	1.04	43.06	⋯	1.96	8.16	⋯	⋯	⋯
74	BG Ser	2.78	⋯	⋯	⋯	7.78	6.91	⋯	⋯	0.46	20.24	⋯	0.76	2.68	⋯	⋯	⋯
75	FS Lib	19.57	⋯	⋯	⋯	5.18	3.17	⋯	⋯	⋯	9.27	⋯	⋯	⋯	⋯	⋯	⋯
76	OH345.0+15.7	⋯	⋯	1.15	⋯	2.59	13.25	⋯	0.73	0.46	3.86	⋯	0.57	⋯	⋯	⋯	⋯
77	U Her	414.41	⋯	3.00	1.11	345.32	244.31	15.98	5.62	3.43	329.29	⋯	5.00	62.79	4.60	⋯	⋯
78	R UMi	8.57	⋯	⋯	⋯	2.16	9.65	⋯	⋯	1.70	3.71	⋯	3.44	⋯	⋯	⋯	⋯
79	T Oph	⋯	⋯	⋯	⋯	1.99	1.37	⋯	⋯	⋯	2.42	⋯	0.57	0.76	⋯	⋯	⋯
80	V446 Oph	12.43	⋯	1.37	⋯	11.21	18.92	⋯	⋯	⋯	19.94	⋯	0.38	3.44	4.21	⋯	⋯
81	AH Dra	⋯	⋯	⋯	⋯	⋯	⋯	⋯	⋯	⋯	⋯	⋯	0.96	⋯	⋯	⋯	⋯
82	IRAS 16486–3014	5.37	⋯	⋯	⋯	11.21	8.10	0.56	⋯	⋯	5.51	⋯	⋯	3.56	⋯	⋯	⋯
83	V2108 Oph	8.45	2.51	17.14	2.02	171.79	144.29	12.53	4.19	1.39	268.83	⋯	2.10	107.70	6.12	⋯	⋯
84	V438 Oph	0.68	⋯	⋯	⋯	⋯	⋯	⋯	⋯	0.54	⋯	⋯	0.95	⋯	⋯	⋯	⋯
85	RV Ser	7.75	⋯	⋯	⋯	8.84	15.31	⋯	⋯	⋯	3.91	⋯	⋯	⋯	⋯	⋯	⋯
86	OH358.23+0.11	49.94	⋯	⋯	0.67	15.43	5.22	⋯	1.72	⋯	26.67	⋯	⋯	11.93	⋯	⋯	⋯
87	IRAS 17436-1545	1.37	⋯	0.62	⋯	2.74	1.99	⋯	⋯	⋯	3.23	⋯	⋯	0.76	1.91	⋯	⋯
88	OH13.1+5.1	⋯	⋯	⋯	⋯	1.01	1.73	⋯	⋯	⋯	1.08	⋯	⋯	⋯	⋯	⋯	⋯
89	VV Sgr	20.29	⋯	0.50	⋯	12.20	19.30	1.25	⋯	⋯	7.14	⋯	⋯	1.15	0.76	⋯	⋯
90	OH4.5-0.4	3.31	⋯	⋯	⋯	3.36	2.37	⋯	⋯	⋯	2.56	⋯	⋯	1.15	⋯	⋯	⋯
91	WY Her	15.75	⋯	2.59	⋯	39.46	15.12	⋯	⋯	⋯	29.05	⋯	0.38	4.02	1.72	⋯	⋯
92	V4120 Sgr	0.68	0.38	2.24	1.12	68.48	56.90	0.25	0.43	1.75	44.32	⋯	3.78	6.12	6.69	0.58	⋯
93	IRAS 18034-2441	⋯	⋯	⋯	⋯	2.22	3.00	⋯	⋯	⋯	1.19	⋯	⋯	⋯	⋯	⋯	⋯
94	IRAS 18035-2529	⋯	⋯	⋯	⋯	1.01	1.73	0.72	⋯	⋯	1.70	⋯	⋯	1.34	⋯	⋯	⋯

Table 8
(Continued)

No.	Source	S(peak) (Jy)														
			^{30}SiO	^{29}SiO	SiO J = 1–0			^{29}SiO	SiO J = 2–1			SiO J= 3–2			HCN	SiS
		H_2O	$v = 0$	$v = 0$	$v = 0$	$v = 1$	$v = 2$	$v = 3$	$v = 0$	$v = 0$	$v = 1$	$v = 2$	$v = 0$	$v = 1$	$v = 2$		
(1)	(2)	(3)	(4)	(5)	(6)	(7)	(8)	(9)	(10)	(11)	(12)	(13)	(14)	(15)	(16)	(17)	(18)
95	V2302 Oph	10.49	⋯	0.50	⋯	4.98	9.21	0.75	⋯	⋯	5.25	⋯	0.57	5.93	⋯	⋯	⋯
96	IRAS 18099+3127	1.27	⋯	⋯	⋯	7.78	7.06	0.43	⋯	⋯	5.56	⋯	⋯	⋯	⋯	⋯	⋯
97	IRAS 18172–2305	⋯	⋯	⋯	⋯	2.37	2.49	⋯	⋯	⋯	0.67	⋯	⋯	⋯	⋯	⋯	⋯
98	V2571 Oph	1.39	⋯	⋯	⋯	1.01	1.15	⋯	⋯	⋯	1.24	⋯	⋯	⋯	⋯	⋯	⋯
99	V1111 Oph	2.05	3.38	7.10	1.87	83.91	90.01	⋯	1.01	2.69	85.53	0.72	4.92	40.15	1.34	0.86	⋯
100	IRAS 18395+0130	⋯	⋯	⋯	⋯	1.33	0.78	⋯	⋯	⋯	⋯	⋯	⋯	⋯	⋯	⋯	⋯
101	RW Lyr	4.63	⋯	⋯	⋯	29.09	52.13	⋯	⋯	0.93	21.78	⋯	1.15	3.25	⋯	⋯	⋯
102	V439 Sct	1.27	⋯	⋯	⋯	4.61	4.46	0.72	⋯	⋯	3.55	⋯	0.76	2.10	⋯	⋯	⋯
103	IRAS 18476+0555	⋯	⋯	⋯	⋯	1.67	2.33	⋯	⋯	⋯	⋯	⋯	⋯	⋯	⋯	⋯	⋯
104	IRAS 18525+0210	⋯	⋯	⋯	⋯	7.22	8.44	⋯	⋯	⋯	⋯	⋯	⋯	⋯	⋯	⋯	⋯
106	V1366 Aql	39.84	0.38	1.30	0.58	10.08	69.84	0.72	1.27	1.55	29.66	⋯	3.82	11.48	1.91	⋯	⋯
107	IRAS 18578+0831	⋯	⋯	⋯	⋯	2.30	3.60	⋯	⋯	⋯	1.39	⋯	⋯	⋯	⋯	⋯	⋯
108	IRAS 19010+1307	2.05	⋯	⋯	⋯	1.25	2.99	⋯	⋯	⋯	0.67	⋯	⋯	⋯	⋯	⋯	⋯
109	V1367 Aql	⋯	⋯	⋯	⋯	2.99	4.86	⋯	⋯	⋯	⋯	⋯	⋯	⋯	⋯	⋯	⋯
110	OH43.9+1.2	2.32	⋯	0.56	⋯	3.22	5.22	0.89	⋯	⋯	0.89	⋯	⋯	⋯	2.09	⋯	⋯
111	V3880 Sgr	33.09	⋯	1.33	0.67	68.49	48.73	⋯	⋯	0.60	33.53	⋯	1.52	5.86	3.56	⋯	⋯
112	OH43.8+0.5	⋯	⋯	⋯	⋯	⋯	1.73	⋯	⋯	⋯	⋯	⋯	⋯	⋯	⋯	⋯	⋯
113	IRAS 19081+0322	⋯	⋯	⋯	⋯	0.50	1.74	⋯	⋯	⋯	1.62	⋯	⋯	1.15	⋯	⋯	⋯
114	IRAS 19183+1148	0.69	⋯	⋯	⋯	2.30	2.16	⋯	⋯	⋯	⋯	⋯	⋯	⋯	⋯	⋯	⋯
115	OH12.11-17.19	⋯	1.47	4.33	⋯	12.77	17.54	⋯	⋯	0.75	12.67	⋯	1.52	7.95	⋯	⋯	⋯
116	IRAS 19186+0315	1.74	⋯	⋯	⋯	2.74	3.02	0.58	⋯	⋯	1.24	⋯	⋯	1.91	⋯	⋯	⋯
117	OH44.79-2.31	11.84	⋯	1.22	0.33	14.54	11.32	⋯	⋯	0.75	6.71	⋯	1.31	6.70	⋯	⋯	⋯
118	OH49.8-0.8	1.83	0.34	0.44	⋯	5.88	6.11	0.33	⋯	⋯	3.87	⋯	⋯	⋯	⋯	⋯	⋯
119	IRAS 19261+1435	⋯	⋯	⋯	⋯	0.86	0.58	⋯	⋯	⋯	1.08	⋯	⋯	⋯	⋯	⋯	⋯
120	IRAS 19265+3116	2.43	⋯	⋯	⋯	2.59	2.59	⋯	⋯	⋯	2.32	⋯	⋯	⋯	⋯	⋯	⋯
121	OH55.0+0.7	⋯	⋯	⋯	1.22	1.78	17.54	1.22	4.06	⋯	1.34	⋯	⋯	⋯	⋯	⋯	⋯
122	OH63.5+5.3	⋯	⋯	0.44	⋯	1.00	1.22	⋯	⋯	⋯	2.38	⋯	⋯	2.09	⋯	⋯	⋯
123	UV Cyg	34.28	⋯	⋯	⋯	1.30	⋯	⋯	⋯	0.62	3.86	⋯	0.76	1.72	⋯	⋯	⋯
124	RT Aql	6.14	⋯	⋯	0.72	94.46	101.23	5.04	⋯	0.93	65.04	⋯	1.34	17.60	3.06	⋯	⋯
125	IRAS 19395+1827	0.73	⋯	⋯	⋯	0.56	0.56	⋯	⋯	⋯	⋯	⋯	⋯	⋯	⋯	⋯	⋯
126	IRAS 19422+3506	9.46	⋯	1.12	0.37	31.00	35.11	3.24	⋯	0.40	6.20	⋯	0.95	2.87	1.34	⋯	⋯
127	OH65.5+1.3	0.57	⋯	⋯	⋯	3.11	2.49	⋯	⋯	⋯	3.77	⋯	⋯	0.96	⋯	⋯	⋯
128	IRAS 19495+0835	0.91	⋯	⋯	⋯	6.97	5.98	⋯	⋯	⋯	2.96	⋯	⋯	1.15	⋯	⋯	⋯
129	RR Aql	22.47	0.50	16.42	1.87	524.88	356.83	1.44	⋯	2.47	222.48	⋯	4.02	19.51	4.78	⋯	⋯
130	IRAS 19579+3223	⋯	⋯	0.56	⋯	5.22	3.55	0.44	⋯	⋯	3.73	⋯	⋯	1.67	⋯	⋯	⋯
131	Z Cyg	2.78	⋯	⋯	⋯	1.01	6.34	⋯	⋯	⋯	0.93	⋯	⋯	⋯	⋯	⋯	⋯
132	V718 Cyg	2.85	⋯	⋯	⋯	1.62	0.62	⋯	⋯	⋯	3.23	⋯	⋯	1.15	⋯	⋯	⋯
133	IRAS 20043+2653	⋯	⋯	⋯	⋯	2.37	3.49	0.62	⋯	⋯	2.56	⋯	⋯	⋯	⋯	⋯	⋯
134	SY Aql	14.90	⋯	⋯	⋯	4.11	1.55	⋯	⋯	⋯	7.90	⋯	⋯	⋯	⋯	⋯	⋯
135	AC Cyg	1.04	⋯	⋯	⋯	⋯	⋯	⋯	⋯	1.08	⋯	⋯	2.49	⋯	⋯	⋯	⋯
136	IRAS 20123+0429	4.67	⋯	⋯	⋯	4.23	1.74	⋯	⋯	⋯	5.39	⋯	⋯	1.53	⋯	⋯	⋯
137	T Mic	6.02	⋯	⋯	⋯	373.54	42.62	⋯	⋯	2.32	23.64	⋯	4.40	⋯	⋯	⋯	⋯

Table 8
(Continued)

No.	Source	S(peak) (Jy)															
			^{30}SiO	^{29}SiO	SiO J = 1–0				^{29}SiO	SiO J = 2–1			SiO J= 3–2			HCN	SiS
		H_2O	$v = 0$	$v = 0$	$v = 0$	$v = 1$	$v = 2$	$v = 3$	$v = 0$	$v = 0$	$v = 1$	$v = 2$	$v = 0$	$v = 1$	$v = 2$		
(1)	(2)	(3)	(4)	(5)	(6)	(7)	(8)	(9)	(10)	(11)	(12)	(13)	(14)	(15)	(16)	(17)	(18)
138	OH63.3–10.2	1.82	0.38	1.87	0.25	13.32	15.56	⋯	⋯	⋯	10.78	⋯	⋯	4.59	5.74	⋯	⋯
139	RU Cap	2.51	⋯	⋯	⋯	6.85	3.74	⋯	⋯	⋯	1.48	⋯	⋯	⋯	⋯	⋯	⋯
140	IRAS 20381+5001	4.67	⋯	0.37	⋯	4.48	3.11	⋯	⋯	⋯	5.25	⋯	⋯	2.87	⋯	⋯	⋯
141	IRAS 20403+3700	1.71	⋯	0.44	⋯	13.21	10.32	0.78	⋯	⋯	7.00	⋯	⋯	2.72	⋯	⋯	⋯
142	OH73.8-6.3	⋯	⋯	⋯	⋯	1.25	1.12	⋯	⋯	⋯	⋯	⋯	⋯	⋯	⋯	⋯	⋯
143	V Aqr	⋯	⋯	⋯	⋯	0.62	⋯	⋯	⋯	⋯	0.94	⋯	0.38	⋯	⋯	⋯	⋯
144	OH83.42-0.89	5.37	⋯	⋯	⋯	7.66	9.10	⋯	⋯	⋯	3.13	⋯	⋯	⋯	⋯	⋯	⋯
145	V363 Cep	7.75	⋯	0.87	0.25	26.77	13.07	⋯	⋯	⋯	9.83	⋯	⋯	3.25	3.06	⋯	⋯
147	TU Peg	32.49	⋯	⋯	⋯	15.06	11.95	⋯	⋯	⋯	7.27	⋯	⋯	1.91	⋯	⋯	⋯
148	EP Aqr	⋯	⋯	⋯	1.33	⋯	⋯	⋯	1.56	5.96	2.83	⋯	11.97	⋯	⋯	⋯	⋯
149	SV Peg	4.52	⋯	⋯	0.58	⋯	0.58	⋯	⋯	2.01	3.40	⋯	2.87	⋯	⋯	⋯	⋯
150	CU Cep	26.74	⋯	⋯	⋯	30.30	12.10	⋯	⋯	⋯	39.34	⋯	⋯	12.77	⋯	⋯	⋯
151	OH104.9+2.4	⋯	⋯	0.87	0.37	4.86	21.91	⋯	⋯	0.40	1.08	⋯	0.38	0.96	⋯	⋯	⋯
152	V627 Cas	9.92	⋯	0.50	⋯	16.19	8.59	⋯	1.15	⋯	15.09	⋯	⋯	3.82	0.96	⋯	⋯
153	R Peg	2.43	⋯	⋯	⋯	25.34	21.31	1.44	⋯	0.93	11.59	⋯	1.91	3.06	⋯	⋯	⋯
154	BU And	0.58	⋯	1.30	⋯	32.98	26.35	⋯	1.27	1.08	18.54	⋯	1.34	8.23	6.12	⋯	⋯
155	R Cas	1.51	1.76	37.73	3.17	168.34	87.41	⋯	2.00	14.83	319.35	⋯	21.80	112.48	42.28	1.19	⋯

Note. Peak flux desities of 144 sources excluding 11 sources with no detection among the 19 molecular lines.

(This table is available in machine-readable form in the online article.)

Table 9
Integrated Flux Density

No.	Source	$\int S\,d\nu$ (Jy km s^{-1})															
			^{30}SiO	^{29}SiO	SiO				^{29}SiO	SiO			SiO			HCN	SiS
		H_2O	J = 1–0						J = 2–1				J= 3–2				
(1)	(2)	(3)	$v = 0$ (4)	$v = 0$ (5)	$v = 0$ (6)	$v = 1$ (7)	$v = 2$ (8)	$v = 3$ (9)	$v = 0$ (10)	$v = 0$ (11)	$v = 1$ (12)	$v = 2$ (13)	$v = 0$ (14)	$v = 1$ (15)	$v = 2$ (16)	(17)	(18)
1	Y Cas	8.91	⋯	3.10	2.55	133.20	157.62	1.18	⋯	7.60	95.81	⋯	10.44	47.72	⋯	⋯	⋯
2	SY Scl	18.30	⋯	⋯	⋯	62.50	72.29	1.87	⋯	⋯	24.87	⋯	⋯	10.33	⋯	⋯	⋯
3	WX Psc	1447.50	52.17	104.98	39.02	1022.40	856.80	18.00	104.83	140.44	401.70	⋯	250.66	101.39	104.45	31.62	16.44
5	V669 Cas	⋯	⋯	⋯	⋯	⋯	17.14	⋯	⋯	⋯	5.56	⋯	⋯	⋯	⋯	⋯	⋯
6	SV Psc	⋯	⋯	⋯	⋯	⋯	⋯	⋯	⋯	8.81	⋯	⋯	11.85	⋯	⋯	⋯	⋯
7	V370 And	⋯	⋯	⋯	10.66	2.22	2.00	⋯	8.90	35.02	23.84	⋯	68.11	⋯	⋯	⋯	⋯
8	omi Cet	⋯	⋯	⋯	1.44	192.96	39.02	⋯	⋯	6.64	673.62	⋯	13.38	105.02	⋯	⋯	⋯
9	YY Ari	7.81	⋯	⋯	⋯	⋯	⋯	⋯	⋯	⋯	⋯	⋯	⋯	⋯	⋯	⋯	⋯
11	T Ari	2.81	⋯	⋯	⋯	37.63	10.99	⋯	⋯	⋯	35.02	⋯	2.83	⋯	⋯	⋯	⋯
12	OH138.0+7.2	⋯	⋯	1.01	⋯	3.17	8.35	⋯	⋯	⋯	5.72	⋯	⋯	⋯	⋯	⋯	⋯
13	IK Tau	571.14	5.89	50.05	45.07	1643.40	1319.70	23.78	21.86	162.99	801.47	⋯	287.43	256.21	72.46	47.38	13.64
14	WZ Eri	⋯	⋯	⋯	⋯	5.33	8.44	⋯	⋯	⋯	2.68	⋯	⋯	⋯	⋯	⋯	⋯
15	IR Per	⋯	⋯	⋯	⋯	1.49	8.09	⋯	⋯	⋯	6.06	⋯	⋯	⋯	⋯	⋯	⋯
16	R Tau	16.10	⋯	⋯	⋯	161.28	169.92	⋯	⋯	3.24	150.79	⋯	7.93	12.13	⋯	⋯	⋯
17	IU Tau	⋯	⋯	2.11	⋯	21.42	23.42	⋯	⋯	⋯	46.64	18.58	6.75	2.30	10.05	⋯	⋯
18	RX Tau	14.36	⋯	⋯	⋯	64.12	26.15	⋯	⋯	3.23	78.53	⋯	4.73	40.53	1.91	⋯	⋯
19	BX Eri	47.54	⋯	⋯	⋯	⋯	1.99	⋯	⋯	3.77	2.29	⋯	6.43	⋯	⋯	⋯	⋯
20	BZ Tau	⋯	⋯	⋯	⋯	16.70	18.14	⋯	⋯	⋯	35.07	⋯	⋯	15.50	⋯	⋯	⋯
21	TX Cam	⋯	4.52	48.51	40.29	517.26	265.29	⋯	5.15	153.47	998.30	0.62	245.89	466.74	119.51	67.36	4.64
22	NV Aur(230918)	⋯	4.52	25.86	17.76	213.12	224.22	22.87	12.80	41.12	88.66	4.84	66.37	17.79	46.67	27.47	⋯
	NV Aur(231013)	1.10	4.75	27.97	18.20	207.57	220.89	17.32	13.27	37.10	85.08	1.87	63.54	19.46	42.70	15.04	⋯
23	RX Lep	⋯	⋯	⋯	⋯	⋯	⋯	⋯	⋯	⋯	2.69	⋯	⋯	⋯	⋯	⋯	⋯
24	IRAS 05131+4530	⋯	⋯	⋯	⋯	4.55	7.88	⋯	⋯	⋯	⋯	⋯	⋯	⋯	⋯	⋯	⋯
25	BW Cam	11.58	0.50	2.45	3.60	159.84	139.97	0.58	⋯	13.60	54.85	⋯	25.05	12.05	2.10	⋯	⋯
26	GP Tau	13.43	⋯	⋯	⋯	13.68	3.74	⋯	⋯	⋯	29.05	⋯	⋯	⋯	⋯	⋯	⋯
27	RW Lep	45.97	⋯	⋯	⋯	21.02	8.93	⋯	⋯	⋯	44.19	⋯	⋯	⋯	⋯	⋯	⋯
28	BX Cam	19.95	3.51	13.07	18.92	141.93	37.85	0.75	5.46	26.40	219.56	⋯	72.05	94.26	48.37	14.40	⋯
29	S Col	29.99	⋯	⋯	⋯	46.80	27.36	⋯	⋯	⋯	56.55	⋯	⋯	11.29	⋯	⋯	⋯
30	AW Tau	13.79	⋯	⋯	⋯	7.97	15.06	1.00	⋯	⋯	10.10	⋯	⋯	3.44	⋯	⋯	⋯
31	U Ori	4.52	⋯	3.89	2.33	473.97	124.32	⋯	⋯	7.75	627.29	⋯	12.84	86.02	38.51	⋯	⋯
32	U Lyn	4.52	⋯	⋯	⋯	145.44	168.48	7.20	⋯	5.41	58.56	⋯	8.41	23.53	⋯	⋯	⋯
33	IRC-10151	15.75	⋯	⋯	⋯	37.30	32.52	⋯	⋯	⋯	22.65	⋯	⋯	2.72	⋯	⋯	⋯
34	IRAS 07153-2411	⋯	⋯	1.00	⋯	2.74	1.12	⋯	⋯	⋯	4.09	⋯	⋯	⋯	⋯	⋯	⋯
35	IRAS 07180-1314	17.95	⋯	1.11	⋯	30.19	36.41	2.55	⋯	⋯	18.33	⋯	⋯	⋯	⋯	⋯	⋯
36	Z Pup	15.39	⋯	⋯	2.24	119.52	90.39	⋯	⋯	11.05	61.15	⋯	7.75	11.85	9.56	⋯	⋯
37	S Gem	11.93	⋯	⋯	⋯	12.10	12.38	⋯	⋯	⋯	10.35	⋯	⋯	4.59	⋯	⋯	⋯
38	R Cnc	10.65	⋯	2.02	2.88	211.68	240.48	⋯	⋯	7.57	363.08	⋯	10.13	118.03	8.42	⋯	⋯
39	RT Hya	⋯	⋯	⋯	⋯	⋯	1.12	⋯	⋯	⋯	2.02	⋯	1.89	⋯	⋯	⋯	⋯
40	V429 Hya	8.91	⋯	⋯	⋯	⋯	⋯	⋯	⋯	1.64	⋯	⋯	⋯	⋯	⋯	⋯	⋯
42	W Cnc	2.96	⋯	⋯	⋯	109.68	69.60	⋯	⋯	6.06	108.03	⋯	6.43	35.95	⋯	⋯	⋯
43	X Hya	85.34	⋯	⋯	⋯	105.84	65.81	⋯	⋯	3.09	133.02	⋯	6.69	26.78	10.71	⋯	⋯
44	IW Hya	11.11	⋯	4.77	3.22	419.58	342.99	5.44	5.62	20.12	90.59	⋯	46.13	29.30	4.19	⋯	⋯
45	R LMi	16.19	⋯	⋯	3.98	128.24	123.88	0.37	⋯	16.03	180.50	⋯	27.04	66.54	4.21	⋯	⋯

Table 9
(Continued)

No.	Source	$\int S\,d\nu$ (Jy km s^{-1})														
			^{30}SiO	^{29}SiO	SiO J = 1–0				^{29}SiO	SiO J = 2–1			SiO J= 3–2			HCN	SiS
		H_2O															
			$v = 0$	$v = 0$	$v = 0$	$v = 1$	$v = 2$	$v = 3$	$v = 0$	$v = 0$	$v = 1$	$v = 2$	$v = 0$	$v = 1$	$v = 2$		
(1)	(2)	(3)	(4)	(5)	(6)	(7)	(8)	(9)	(10)	(11)	(12)	(13)	(14)	(15)	(16)	(17)	(18)
46	R Leo	2.81	⋯	1.44	7.55	985.68	728.16	11.99	7.65	204.13	907.41	⋯	127.51	92.09	133.32	3.92	⋯
47	V Leo	⋯	⋯	⋯	⋯	⋯	2.88	⋯	⋯	⋯	⋯	⋯	⋯	⋯	⋯	⋯	⋯
48	R UMa	15.75	⋯	⋯	⋯	49.73	26.64	0.78	⋯	⋯	41.42	⋯	⋯	4.60	⋯	⋯	⋯
49	VX UMa	6.95	⋯	⋯	⋯	23.66	34.86	⋯	⋯	3.50	28.29	⋯	5.67	12.81	1.53	⋯	⋯
50	R Crt	1311.00	⋯	⋯	17.93	23.03	22.66	⋯	12.22	65.33	90.92	⋯	106.09	14.15	⋯	⋯	⋯
52	AF Leo	19.04	⋯	⋯	⋯	⋯	⋯	⋯	⋯	3.10	3.91	⋯	4.35	⋯	⋯	⋯	⋯
54	S Crt	51.77	⋯	⋯	⋯	⋯	⋯	⋯	⋯	⋯	9.09	⋯	⋯	⋯	⋯	⋯	⋯
55	Z UMa	⋯	⋯	⋯	⋯	3.02	⋯	⋯	⋯	⋯	16.22	⋯	⋯	5.74	⋯	⋯	⋯
56	T Vir	17.46	⋯	⋯	⋯	11.99	11.99	⋯	⋯	⋯	21.46	⋯	⋯	⋯	⋯	⋯	⋯
57	BK Vir	2.28	⋯	⋯	4.36	4.73	4.61	⋯	⋯	9.70	43.91	⋯	22.31	⋯	⋯	⋯	⋯
59	RT Vir	221.16	⋯	⋯	8.96	28.39	2.99	⋯	8.20	43.10	70.45	⋯	80.56	4.59	⋯	⋯	⋯
60	SW Vir	⋯	⋯	⋯	10.08	⋯	⋯	⋯	15.29	56.55	38.16	⋯	100.38	⋯	⋯	⋯	⋯
61	R Hya	2.08	⋯	⋯	3.77	194.25	79.14	⋯	3.43	36.95	306.94	⋯	72.24	11.72	⋯	⋯	⋯
62	W Hya	135.49	1.88	135.36	20.59	5313.60	6105.60	46.80	32.21	168.41	3229.05	⋯	217.97	1369.71	621.73	10.71	⋯
63	AY Vir	88.46	⋯	⋯	⋯	⋯	⋯	⋯	⋯	4.31	⋯	⋯	5.29	⋯	⋯	⋯	⋯
64	RU Hya	11.06	⋯	⋯	⋯	74.70	26.15	⋯	⋯	⋯	64.39	⋯	2.65	8.99	⋯	⋯	⋯
65	RX Boo	178.33	⋯	2.88	25.49	20.30	48.67	⋯	19.47	110.93	200.85	⋯	137.09	9.18	⋯	7.14	⋯
66	RS Vir	46.63	⋯	⋯	⋯	27.02	12.20	⋯	⋯	3.23	31.79	⋯	6.81	2.49	⋯	⋯	⋯
68	Y Cen	⋯	⋯	⋯	⋯	2.33	1.55	⋯	⋯	7.75	12.22	⋯	16.54	⋯	⋯	⋯	⋯
70	Y Lib	8.66	⋯	⋯	⋯	13.94	8.59	⋯	⋯	⋯	10.37	⋯	⋯	4.78	⋯	⋯	⋯
71	S CrB	19.34	⋯	⋯	3.46	23.18	71.86	⋯	⋯	12.98	30.90	⋯	26.00	⋯	⋯	⋯	⋯
72	WX Ser	74.24	⋯	⋯	⋯	101.90	83.81	⋯	⋯	7.90	92.53	⋯	14.14	19.26	⋯	⋯	⋯
74	BG Ser	8.11	⋯	⋯	⋯	33.26	28.08	⋯	⋯	4.33	93.63	⋯	4.21	12.05	⋯	⋯	⋯
75	FS Lib	20.84	⋯	⋯	⋯	12.96	12.96	⋯	⋯	⋯	29.20	⋯	⋯	⋯	⋯	⋯	⋯
76	OH345.0+15.7	⋯	⋯	2.30	⋯	8.06	40.32	⋯	3.28	8.65	8.96	⋯	9.18	⋯	⋯	⋯	⋯
77	U Her	750.92	⋯	4.55	16.43	1343.10	945.72	30.53	13.11	22.20	815.03	⋯	27.20	217.67	6.07	⋯	⋯
78	R UMi	13.32	⋯	⋯	⋯	7.34	25.78	⋯	⋯	8.34	16.53	⋯	17.02	⋯	⋯	⋯	⋯
79	T Oph	⋯	⋯	⋯	⋯	6.23	3.98	⋯	⋯	⋯	6.74	⋯	1.32	1.15	⋯	⋯	⋯
80	V446 Oph	21.20	⋯	1.99	⋯	64.86	45.57	⋯	⋯	⋯	69.24	⋯	4.16	11.47	13.77	⋯	⋯
81	AH Dra	⋯	⋯	⋯	⋯	⋯	⋯	⋯	⋯	⋯	⋯	⋯	6.69	⋯	⋯	⋯	⋯
82	IRAS 16486–3014	12.94	⋯	⋯	⋯	42.96	46.84	3.11	⋯	⋯	20.71	⋯	⋯	7.12	⋯	⋯	⋯
83	V2108 Oph	35.20	3.76	26.93	6.91	684.00	614.88	36.86	15.29	21.17	651.99	⋯	42.06	250.60	10.52	⋯	⋯
84	V438 Oph	3.88	⋯	⋯	⋯	⋯	⋯	⋯	⋯	1.62	⋯	⋯	5.11	⋯	⋯	⋯	⋯
85	RV Ser	12.31	⋯	⋯	⋯	16.19	25.77	⋯	⋯	⋯	11.72	⋯	⋯	⋯	⋯	⋯	⋯
86	OH358.23+0.11	190.48	⋯	⋯	3.33	148.74	36.52	⋯	5.46	⋯	248.83	⋯	⋯	82.88	⋯	⋯	⋯
87	IRAS 17436-1545	2.74	⋯	1.12	⋯	10.33	8.96	⋯	⋯	⋯	8.22	⋯	⋯	1.34	1.72	⋯	⋯
88	OH13.1+5.1	⋯	⋯	⋯	⋯	2.45	4.75	⋯	⋯	⋯	1.55	⋯	⋯	⋯	⋯	⋯	⋯
89	VV Sgr	18.81	⋯	0.50	⋯	55.28	39.22	1.49	⋯	⋯	35.70	⋯	⋯	3.44	1.53	⋯	⋯
90	OH4.5-0.4	9.58	⋯	⋯	⋯	13.20	12.82	⋯	⋯	⋯	10.51	⋯	⋯	1.53	⋯	⋯	⋯
91	WY Her	34.62	⋯	3.17	⋯	107.57	55.30	⋯	⋯	⋯	67.83	⋯	7.07	12.24	3.63	⋯	⋯
92	V4120 Sgr	0.80	0.50	5.10	6.85	417.08	270.17	0.37	7.33	29.77	175.11	⋯	60.70	44.93	12.43	15.26	⋯
93	IRAS 18034-2441	⋯	⋯	⋯	⋯	1.55	5.77	⋯	⋯	⋯	1.49	⋯	⋯	⋯	⋯	⋯	⋯
94	IRAS 18035-2529	⋯	⋯	⋯	⋯	2.16	5.62	1.15	⋯	⋯	2.47	⋯	⋯	1.53	⋯	⋯	⋯

Table 9
(Continued)

No.	Source	$\int S\,d\nu$ (Jy km s^{-1})														
			^{30}SiO	^{29}SiO	SiO J = 1–0				^{29}SiO	SiO J = 2–1			SiO J= 3–2			HCN	SiS
		H_2O	$v = 0$	$v = 0$	$v = 0$	$v = 1$	$v = 2$	$v = 3$	$v = 0$	$v = 0$	$v = 1$	$v = 2$	$v = 0$	$v = 1$	$v = 2$		
(1)	(2)	(3)	(4)	(5)	(6)	(7)	(8)	(9)	(10)	(11)	(12)	(13)	(14)	(15)	(16)	(17)	(18)
95	V2302 Oph	24.17	⋯	1.37	⋯	16.68	23.16	1.00	⋯	⋯	18.45	⋯	9.83	13.38	⋯	⋯	⋯
96	IRAS 18099+3127	4.40	⋯	⋯	⋯	22.90	21.31	0.58	⋯	⋯	15.14	⋯	⋯	⋯	⋯	⋯	⋯
97	IRAS 18172–2305	⋯	⋯	⋯	⋯	6.97	5.98	⋯	⋯	⋯	5.79	⋯	⋯	⋯	⋯	⋯	⋯
98	V2571 Oph	1.62	⋯	⋯	⋯	3.02	4.46	⋯	⋯	⋯	4.02	⋯	⋯	⋯	⋯	⋯	⋯
99	V1111 Oph	11.51	7.64	15.56	18.05	357.32	402.14	⋯	22.15	53.34	258.62	1.44	99.09	80.50	0.96	22.32	⋯
100	IRAS 18395+0130	⋯	⋯	⋯	⋯	4.33	2.66	⋯	⋯	⋯	⋯	⋯	⋯	⋯	⋯	⋯	⋯
101	RW Lyr	7.53	⋯	⋯	⋯	77.76	116.93	⋯	⋯	4.17	56.55	⋯	6.69	3.25	⋯	⋯	⋯
102	V439 Sct	3.47	⋯	⋯	⋯	16.70	18.58	1.01	⋯	⋯	7.26	⋯	16.25	6.50	⋯	⋯	⋯
103	IRAS 18476+0555	⋯	⋯	⋯	⋯	4.77	6.33	⋯	⋯	⋯	⋯	⋯	⋯	⋯	⋯	⋯	⋯
104	IRAS 18525+0210	⋯	⋯	⋯	⋯	15.65	29.86	⋯	⋯	⋯	⋯	⋯	⋯	⋯	⋯	⋯	⋯
106	V1366 Aql	91.48	0.38	2.74	9.36	51.41	195.84	2.88	6.37	36.15	75.24	⋯	86.61	30.03	3.83	⋯	⋯
107	IRAS 18578+0831	⋯	⋯	⋯	⋯	9.65	12.96	⋯	⋯	⋯	4.02	⋯	⋯	⋯	⋯	⋯	⋯
108	IRAS 19010+1307	4.79	⋯	⋯	⋯	4.86	5.23	⋯	⋯	⋯	3.23	⋯	⋯	⋯	⋯	⋯	⋯
109	V1367 Aql	⋯	⋯	⋯	⋯	6.85	13.57	⋯	⋯	⋯	⋯	⋯	⋯	⋯	⋯	⋯	⋯
110	OH43.9+1.2	3.66	⋯	1.22	⋯	11.21	18.65	1.44	⋯	⋯	5.66	⋯	⋯	⋯	1.47	⋯	⋯
111	V3880 Sgr	68.74	⋯	2.11	4.22	136.53	120.99	⋯	⋯	10.13	91.34	⋯	26.55	14.02	9.21	⋯	⋯
112	OH43.8+0.5	⋯	⋯	⋯	⋯	⋯	4.90	⋯	⋯	⋯	⋯	⋯	⋯	⋯	⋯	⋯	⋯
113	IRAS 19081+0322	⋯	⋯	⋯	⋯	1.00	4.36	⋯	⋯	⋯	3.23	⋯	⋯	2.29	⋯	⋯	⋯
114	IRAS 19183+1148	0.69	⋯	⋯	⋯	5.04	6.77	⋯	⋯	⋯	⋯	⋯	⋯	⋯	⋯	⋯	⋯
115	OH12.11-17.19	⋯	2.60	7.33	⋯	56.28	57.61	⋯	⋯	18.03	38.14	⋯	36.34	10.05	⋯	⋯	⋯
116	IRAS 19186+0315	3.59	⋯	⋯	⋯	13.54	14.40	1.87	⋯	⋯	5.56	⋯	⋯	5.55	⋯	⋯	⋯
117	OH44.79-2.31	26.13	⋯	1.89	6.55	54.95	42.07	⋯	⋯	14.90	19.82	⋯	27.85	17.58	⋯	⋯	⋯
118	OH49.8-0.8	4.27	0.34	0.78	⋯	17.87	16.98	0.44	⋯	⋯	9.09	⋯	⋯	⋯	⋯	⋯	⋯
119	IRAS 19261+1435	⋯	⋯	⋯	⋯	1.15	1.15	⋯	⋯	⋯	2.63	⋯	⋯	⋯	⋯	⋯	⋯
120	IRAS 19265+3116	10.31	⋯	⋯	⋯	8.64	7.34	⋯	⋯	⋯	9.27	⋯	⋯	⋯	⋯	⋯	⋯
121	OH55.0+0.7	⋯	⋯	⋯	2.78	4.66	42.40	3.55	5.00	⋯	1.64	⋯	⋯	⋯	⋯	⋯	⋯
122	OH63.5+5.3	⋯	⋯	0.33	⋯	3.89	5.77	⋯	⋯	⋯	6.85	⋯	⋯	3.98	⋯	⋯	⋯
123	UV Cyg	70.52	⋯	⋯	⋯	1.44	⋯	⋯	⋯	17.46	24.10	⋯	12.62	12.82	⋯	⋯	⋯
124	RT Aql	15.63	⋯	⋯	1.01	201.60	216.00	9.22	⋯	4.94	134.57	⋯	5.35	36.54	3.06	⋯	⋯
125	IRAS 19395+1827	1.59	⋯	⋯	⋯	1.78	2.33	⋯	⋯	⋯	⋯	⋯	⋯	⋯	⋯	⋯	⋯
126	IRAS 19422+3506	20.98	⋯	2.99	1.49	82.54	61.63	3.24	⋯	9.43	33.54	⋯	18.91	6.50	3.63	⋯	⋯
127	OH65.5+1.3	1.14	⋯	⋯	⋯	10.33	10.33	⋯	⋯	⋯	10.24	⋯	⋯	3.25	⋯	⋯	⋯
128	IRAS 19495+0835	2.39	⋯	⋯	⋯	19.92	16.31	⋯	⋯	⋯	11.18	⋯	⋯	1.53	⋯	⋯	⋯
129	RR Aql	40.07	1.13	26.78	8.50	1336.32	964.80	1.73	⋯	16.53	542.30	⋯	27.34	50.12	12.05	⋯	⋯
130	IRAS 19579+3223	⋯	⋯	0.78	⋯	22.76	15.32	0.44	⋯	⋯	13.56	⋯	⋯	5.02	⋯	⋯	⋯
131	Z Cyg	2.08	⋯	⋯	⋯	2.02	6.91	⋯	⋯	⋯	1.39	⋯	⋯	⋯	⋯	⋯	⋯
132	V718 Cyg	7.07	⋯	⋯	⋯	9.84	1.74	⋯	⋯	⋯	23.44	⋯	⋯	9.37	⋯	⋯	⋯
133	IRAS 20043+2653	⋯	⋯	⋯	⋯	6.85	10.48	0.75	⋯	⋯	4.71	⋯	⋯	⋯	⋯	⋯	⋯
134	SY Aql	16.97	⋯	⋯	⋯	14.32	9.21	⋯	⋯	⋯	15.05	⋯	⋯	⋯	⋯	⋯	⋯
135	AC Cyg	1.51	⋯	⋯	⋯	⋯	⋯	⋯	⋯	7.26	⋯	⋯	8.80	⋯	⋯	⋯	⋯
136	IRAS 20123+0429	7.41	⋯	⋯	⋯	12.45	4.73	⋯	⋯	⋯	11.85	⋯	⋯	3.44	⋯	⋯	⋯
137	T Mic	16.79	⋯	⋯	⋯	42.62	19.15	⋯	⋯	12.82	93.94	⋯	18.93	⋯	⋯	⋯	⋯

Table 9
(Continued)

No.	Source	$\int S\,d\nu$ (Jy km s^{-1})															
			^{30}SiO	^{29}SiO	SiO				^{29}SiO	SiO			SiO			HCN	SiS
		H_2O	$J = 1$–0						$J = 2$–1				$J = 3$–2				
			$v = 0$	$v = 0$	$v = 0$	$v = 1$	$v = 2$	$v = 3$	$v = 0$	$v = 0$	$v = 1$	$v = 2$	$v = 0$	$v = 1$	$v = 2$		
(1)	(2)	(3)	(4)	(5)	(6)	(7)	(8)	(9)	(10)	(11)	(12)	(13)	(14)	(15)	(16)	(17)	(18)
138	OH63.3–10.2	3.08	0.88	4.73	3.24	44.94	52.91	⋯	⋯	⋯	26.67	⋯	⋯	7.07	9.18	⋯	⋯
139	RU Cap	2.96	⋯	⋯	⋯	11.58	1.62	⋯	⋯	⋯	4.18	⋯	⋯	⋯	⋯	⋯	⋯
140	IRAS 20381+5001	20.63	⋯	0.75	⋯	21.17	14.44	⋯	⋯	⋯	19.80	⋯	⋯	5.93	⋯	⋯	⋯
141	IRAS 20403+3700	4.88	⋯	0.89	⋯	36.52	27.08	1.67	⋯	⋯	27.12	⋯	⋯	7.33	⋯	⋯	⋯
142	OH73.8-6.3	⋯	⋯	⋯	⋯	4.86	2.61	⋯	⋯	⋯	⋯	⋯	⋯	⋯	⋯	⋯	⋯
143	V Aqr	⋯	⋯	⋯	⋯	1.00	⋯	⋯	⋯	⋯	1.08	⋯	1.51	⋯	⋯	⋯	⋯
144	OH83.42-0.89	28.82	⋯	⋯	⋯	27.64	31.30	⋯	⋯	⋯	10.28	⋯	⋯	⋯	⋯	⋯	⋯
145	V363 Cep	19.72	⋯	2.37	3.86	122.01	77.81	⋯	⋯	⋯	61.42	⋯	⋯	13.77	5.93	⋯	⋯
147	TU Peg	49.48	⋯	⋯	⋯	37.10	27.14	⋯	⋯	⋯	43.10	⋯	⋯	5.54	⋯	⋯	⋯
148	EP Aqr	⋯	⋯	⋯	11.54	⋯	⋯	⋯	12.80	59.60	13.26	⋯	116.63	⋯	⋯	⋯	⋯
149	SV Peg	6.25	⋯	⋯	3.46	⋯	0.72	⋯	⋯	17.46	23.64	⋯	21.41	⋯	⋯	⋯	⋯
150	CU Cep	47.99	⋯	⋯	⋯	140.97	43.40	⋯	⋯	⋯	305.45	⋯	⋯	123.28	⋯	⋯	⋯
151	OH104.9+2.4	⋯	⋯	1.62	1.49	10.46	40.71	⋯	⋯	9.43	3.23	⋯	9.08	0.76	⋯	⋯	⋯
152	V627 Cas	57.00	⋯	0.87	⋯	121.01	59.01	⋯	3.60	⋯	104.26	⋯	⋯	25.62	2.10	⋯	⋯
153	R Peg	4.17	⋯	⋯	⋯	66.82	68.54	2.16	⋯	6.74	39.40	⋯	11.09	9.18	⋯	⋯	⋯
154	BU And	0.69	⋯	4.32	⋯	151.20	82.08	⋯	7.10	7.42	122.83	⋯	10.52	39.98	14.16	⋯	⋯
155	R Cas	3.36	1.63	49.82	25.20	714.24	321.12	⋯	18.56	146.00	1378.14	⋯	237.09	424.69	141.37	9.35	⋯

Note. Integrated flux densities of 144 sources excluding 11 sources with no detection among the 19 molecular lines.

(This table is available in machine-readable form in the online article.)

Table 10
Intensity Ratios of Peak and Integrated Flux Densities w.r.t. SiO11 Maser

No.	Source Name	$\frac{P.F(H_2O)}{P.F(SiO11)}$	$\frac{P.F(SiO21)}{P.F(SiO11)}$	$\frac{P.F(SiO12)}{P.F(SiO11)}$	$\frac{P.F(SiO13)}{P.F(SiO11)}$	$\frac{I.F(H_2O)}{I.F(SiO11)}$	$\frac{I.F(SiO21)}{I.F(SiO11)}$	$\frac{I.F(SiO12)}{I.F(SiO11)}$	$\frac{I.F(SiO13)}{I.F(SiO11)}$
1	Y Cas	0.07	0.75	0.58	0.39	0.07	1.18	0.72	0.36
2	SY Scl	0.37	1.02	0.29	0.29	0.29	1.16	0.40	0.17
3	WX Psc	3.01	0.85	0.54	0.12	1.42	0.84	0.39	0.10
5	V669 Cas	⋯	⋯	⋯	⋯	⋯	⋯	⋯	⋯
6	SV Psc	⋯	⋯	⋯	⋯	⋯	⋯	⋯	⋯
7	V370 And	⋯	1.75	7.05	⋯	⋯	0.90	10.74	⋯
8	omi Cet	⋯	0.34	2.62	0.84	⋯	0.20	3.49	0.54
9	YY Ari	⋯	⋯	⋯	⋯	⋯	⋯	⋯	⋯
11	T Ari	0.07	0.51	1.04	⋯	0.07	0.29	0.93	⋯
12	OH138.0+7.2	⋯	4.57	2.15	⋯	⋯	2.64	1.80	⋯
13	IK Tau	0.25	0.98	0.40	0.14	0.35	0.80	0.49	0.16
14	WZ Eri	⋯	1.00	1.14	⋯	⋯	1.58	0.50	⋯
15	IR Per	⋯	5.33	3.25	⋯	⋯	5.42	4.06	⋯
16	R Tau	0.10	0.77	1.06	0.07	0.10	1.05	0.93	0.08
17	IU Tau	⋯	0.90	1.09	0.19	⋯	1.09	2.18	0.11
18	RX Tau	0.56	0.56	1.08	0.76	0.22	0.41	1.22	0.63
19	BX Eri	⋯	⋯	⋯	⋯	⋯	⋯	⋯	⋯
20	BZ Tau	⋯	1.06	2.08	0.80	⋯	1.09	2.10	0.93
21	TX Cam	⋯	0.67	2.58	1.42	⋯	0.51	1.93	0.90
22	NV Aur(230918)	...	0.96	0.49	0.12	...	1.05	0.42	0.08
	NV Aur(231013)	0.01	0.96	0.41	0.14	0.01	1.06	0.41	0.09
23	RX Lep	⋯	⋯	⋯	⋯	⋯	⋯	⋯	⋯
24	IRAS 05131+4530	⋯	1.15	⋯	⋯	⋯	1.73	⋯	⋯
25	BW Cam	0.19	1.15	0.52	0.07	0.07	0.88	0.34	0.08
26	GP Tau	2.30	0.22	0.98	⋯	0.98	0.27	2.12	⋯
27	RW Lep	8.60	1.17	1.81	⋯	2.19	0.42	2.10	⋯
28	BX Cam	0.28	0.93	1.67	0.86	0.14	0.27	1.55	0.66
29	S Col	1.52	0.56	2.29	0.50	0.64	0.58	1.21	0.24
30	AW Tau	1.83	2.00	0.70	0.54	1.73	1.89	1.27	0.43
31	U Ori	0.02	0.22	1.43	0.16	0.01	0.26	1.32	0.18
32	U Lyn	0.04	1.24	0.17	0.16	0.03	1.16	0.40	0.16
33	IRC-10151	0.26	1.01	0.51	0.13	0.42	0.87	0.61	0.07
34	IRAS 07153-2411	⋯	0.50	1.35	⋯	⋯	0.41	1.50	⋯
35	IRAS 07180-1314	0.56	0.86	0.43	⋯	0.59	1.21	0.61	⋯
36	Z Pup	0.48	0.59	0.61	0.14	0.13	0.76	0.51	0.10
37	S Gem	1.97	0.89	0.42	0.59	0.99	1.02	0.86	0.38
38	R Cnc	0.15	2.21	2.36	1.01	0.05	1.14	1.72	0.56
39	RT Hya	⋯	⋯	⋯	⋯	⋯	⋯	⋯	⋯
40	V429 Hya	⋯	⋯	⋯	⋯	⋯	⋯	⋯	⋯
42	W Cnc	0.10	0.83	1.32	0.82	0.03	0.63	0.98	0.33
43	X Hya	1.55	1.05	1.35	0.43	0.81	0.62	1.26	0.25
44	IW Hya	0.07	0.75	0.33	0.13	0.03	0.82	0.22	0.07
45	R LMi	0.29	1.21	1.05	0.31	0.13	0.97	1.41	0.52
46	R Leo	0.01	1.35	1.17	0.15	0.00	0.74	0.92	0.09
47	V Leo	⋯	⋯	⋯	⋯	⋯	⋯	⋯	⋯
48	R UMa	0.38	0.57	0.61	0.09	0.32	0.54	0.83	0.09
49	VX UMa	0.48	2.86	1.47	1.10	0.29	1.47	1.20	0.54
50	R Crt	63.10	0.67	1.68	0.34	56.92	0.98	3.95	0.61
52	AF Leo	⋯	⋯	⋯	⋯	⋯	⋯	⋯	⋯
54	S Crt	⋯	⋯	⋯	⋯	⋯	⋯	⋯	⋯
55	Z UMa	⋯	⋯	5.19	2.21	⋯	⋯	5.36	1.90
56	T Vir	3.27	1.10	1.71	⋯	1.46	1.00	1.79	⋯
57	BK Vir	0.98	0.93	6.64	⋯	0.48	0.97	9.28	⋯
59	RT Vir	4.90	0.07	1.34	0.26	7.79	0.11	2.48	0.16
60	SW Vir	⋯	⋯	⋯	⋯	⋯	⋯	⋯	⋯
61	R Hya	0.02	0.63	1.75	0.07	0.01	0.41	1.58	0.06
62	W Hya	0.03	0.88	0.73	0.39	0.03	1.15	0.61	0.26
63	AY Vir	⋯	⋯	⋯	⋯	⋯	⋯	⋯	⋯
64	RU Hya	0.26	0.44	0.51	0.09	0.15	0.35	0.86	0.12
65	RX Boo	27.70	3.53	3.66	0.43	8.78	2.40	9.89	0.45
66	RS Vir	4.02	0.40	1.11	0.18	1.73	0.45	1.18	0.09
68	Y Cen	⋯	0.63	3.36	⋯	⋯	0.67	5.24	⋯
70	Y Lib	0.87	0.90	0.55	0.29	0.62	0.62	0.74	0.34
71	S CrB	1.21	4.57	1.41	⋯	0.83	3.10	1.33	⋯

Table 10
(Continued)

No.	Source Name	$\frac{P.F(H_2O)}{P.F(SiO11)}$	$\frac{P.F(SiO21)}{P.F(SiO11)}$	$\frac{P.F(SiO12)}{P.F(SiO11)}$	$\frac{P.F(SiO13)}{P.F(SiO11)}$	$\frac{I.F(H_2O)}{I.F(SiO11)}$	$\frac{I.F(SiO21)}{I.F(SiO11)}$	$\frac{I.F(SiO12)}{I.F(SiO11)}$	$\frac{I.F(SiO13)}{I.F(SiO11)}$
72	WX Ser	1.20	0.61	1.19	0.22	0.73	0.82	0.91	0.19
74	BG Ser	0.36	0.89	2.60	0.34	0.24	0.84	2.81	0.36
75	FS Lib	3.78	0.61	1.79	⋯	1.61	1.00	2.25	⋯
76	OH345.0+15.7	⋯	5.11	1.49	⋯	⋯	5.00	1.11	⋯
77	U Her	1.20	0.71	0.95	0.18	0.56	0.70	0.61	0.16
78	R UMi	3.97	4.47	1.72	⋯	1.81	3.51	2.25	⋯
79	T Oph	⋯	0.69	1.22	0.38	⋯	0.64	1.08	0.18
80	V446 Oph	1.11	1.69	1.78	0.31	0.33	0.70	1.07	0.18
81	AH Dra	⋯	⋯	⋯	⋯	⋯	⋯	⋯	⋯
82	IRAS 16486–3014	0.48	0.72	0.49	0.32	0.30	1.09	0.48	0.17
83	V2108 Oph	0.05	0.84	1.56	0.63	0.05	0.90	0.95	0.37
84	V438 Oph	⋯	⋯	⋯	⋯	⋯	⋯	⋯	⋯
85	RV Ser	0.88	1.73	0.44	⋯	0.76	1.59	0.72	⋯
86	OH358.23+0.11	3.24	0.34	1.73	0.77	1.28	0.25	1.67	0.56
87	IRAS 17436-1545	0.50	0.73	1.18	0.28	0.26	0.87	0.80	0.13
88	OH13.1+5.1	⋯	1.71	1.07	⋯	⋯	1.94	0.63	⋯
89	VV Sgr	1.66	1.58	0.59	0.09	0.34	0.71	0.65	0.06
90	OH4.5-0.4	0.98	0.70	0.76	0.34	0.73	0.97	0.80	0.12
91	WY Her	0.40	0.38	0.74	0.10	0.32	0.51	0.63	0.11
92	V4120 Sgr	0.01	0.83	0.65	0.09	0.00	0.65	0.42	0.11
93	IRAS 18034-2441	⋯	1.35	0.54	⋯	⋯	3.71	0.96	⋯
94	IRAS 18035-2529	⋯	1.71	1.69	1.33	⋯	2.60	1.14	0.71
95	V2302 Oph	2.11	1.85	1.05	1.19	1.45	1.39	1.11	0.80
96	IRAS 18099+3127	0.16	0.91	0.72	⋯	0.19	0.93	0.66	⋯
97	IRAS 18172–2305	⋯	1.05	0.28	⋯	⋯	0.86	0.83	⋯
98	V2571 Oph	1.38	1.14	1.23	⋯	0.54	1.48	1.33	⋯
99	V1111 Oph	0.02	1.07	1.02	0.48	0.03	1.13	0.72	0.23
100	IRAS 18395+0130	⋯	0.58	⋯	⋯	⋯	0.62	⋯	⋯
101	RW Lyr	0.16	1.79	0.75	0.11	0.10	1.50	0.73	0.04
102	V439 Sct	0.28	0.97	0.77	0.46	0.21	1.11	0.43	0.39
103	IRAS 18476+0555	⋯	1.40	⋯	⋯	⋯	1.33	⋯	⋯
104	IRAS 18525+0210	⋯	1.17	⋯	⋯	⋯	1.91	⋯	⋯
106	V1366 Aql	3.95	6.93	2.94	1.14	1.78	3.81	1.46	0.58
107	IRAS 18578+0831	⋯	1.56	0.60	⋯	⋯	1.34	0.42	⋯
108	IRAS 19010+1307	1.65	2.40	0.54	⋯	0.99	1.08	0.67	⋯
109	V1367 Aql	⋯	1.63	⋯	⋯	⋯	1.98	⋯	⋯
110	OH43.9+1.2	0.72	1.62	0.28	⋯	0.33	1.66	0.51	⋯
111	V3880 Sgr	0.48	0.71	0.49	0.09	0.50	0.89	0.67	0.10
112	OH43.8+0.5	⋯	⋯	⋯	⋯	⋯	⋯	⋯	⋯
113	IRAS 19081+0322	⋯	3.50	3.25	2.30	⋯	4.38	3.25	2.30
114	IRAS 19183+1148	0.30	0.94	⋯	⋯	0.14	1.34	⋯	⋯
115	OH12.11-17.19	⋯	1.37	0.99	0.62	⋯	1.02	0.68	0.18
116	IRAS 19186+0315	0.63	1.11	0.45	0.70	0.27	1.06	0.41	0.41
117	OH44.79-2.31	0.81	0.78	0.46	0.46	0.48	0.77	0.36	0.32
118	OH49.8-0.8	0.31	1.04	0.66	⋯	0.24	0.95	0.51	⋯
119	IRAS 19261+1435	⋯	0.67	1.25	⋯	⋯	1.00	2.28	⋯
120	IRAS 19265+3116	0.94	1.00	0.89	⋯	1.19	0.85	1.07	⋯
121	OH55.0+0.7	⋯	9.88	0.76	⋯	⋯	9.10	0.35	⋯
122	OH63.5+5.3	⋯	1.22	2.39	2.10	⋯	1.49	1.76	1.02
123	UV Cyg	26.45	⋯	2.98	1.33	48.97	⋯	16.74	8.90
124	RT Aql	0.06	1.07	0.69	0.19	0.08	1.07	0.67	0.18
125	IRAS 19395+1827	1.32	1.00	⋯	⋯	0.89	1.31	⋯	⋯
126	IRAS 19422+3506	0.31	1.13	0.20	0.09	0.25	0.75	0.41	0.08
127	OH65.5+1.3	0.18	0.80	1.21	0.31	0.11	1.00	0.99	0.31
128	IRAS 19495+0835	0.13	0.86	0.43	0.16	0.12	0.82	0.56	0.08
129	RR Aql	0.04	0.68	0.42	0.04	0.03	0.72	0.41	0.04
130	IRAS 19579+3223	⋯	0.68	0.71	0.32	⋯	0.67	0.60	0.22
131	Z Cyg	2.76	6.29	0.92	⋯	1.03	3.43	0.69	⋯
132	V718 Cyg	1.76	0.38	2.00	0.71	0.72	0.18	2.38	0.95
133	IRAS 20043+2653	⋯	1.47	1.08	⋯	⋯	1.53	0.69	⋯
134	SY Aql	3.63	0.38	1.92	⋯	1.19	0.64	1.05	⋯
135	AC Cyg	⋯	⋯	⋯	⋯	⋯	⋯	⋯	⋯
136	IRAS 20123+0429	1.10	0.41	1.27	0.36	0.60	0.38	0.95	0.28
137	T Mic	0.02	0.11	0.06	⋯	0.39	0.45	2.20	⋯

Table 10
(Continued)

No.	Source Name	$\frac{\text{P.F}(H_2O)}{\text{P.F(SiO11)}}$	$\frac{\text{P.F(SiO21)}}{\text{P.F(SiO11)}}$	$\frac{\text{P.F(SiO12)}}{\text{P.F(SiO11)}}$	$\frac{\text{P.F(SiO13)}}{\text{P.F(SiO11)}}$	$\frac{\text{I.F}(H_2O)}{\text{I.F(SiO11)}}$	$\frac{\text{I.F(SiO21)}}{\text{I.F(SiO11)}}$	$\frac{\text{I.F(SiO12)}}{\text{I.F(SiO11)}}$	$\frac{\text{I.F(SiO13)}}{\text{I.F(SiO11)}}$
138	OH63.3–10.2	0.14	1.17	0.81	0.34	0.07	1.18	0.59	0.16
139	RU Cap	0.37	0.55	0.22	⋯	0.26	0.14	0.36	⋯
140	IRAS 20381+5001	1.04	0.69	1.17	0.64	0.97	0.68	0.94	0.28
141	IRAS 20403+3700	0.13	0.78	0.53	0.21	0.13	0.74	0.74	0.20
142	OH73.8-6.3	⋯	0.90	⋯	⋯	⋯	0.54	⋯	⋯
143	V Aqr	⋯	⋯	1.51	⋯	⋯	⋯	1.08	⋯
144	OH83.42-0.89	0.70	1.19	0.41	⋯	1.04	1.13	0.37	⋯
145	V363 Cep	0.29	0.49	0.37	0.12	0.16	0.64	0.50	0.11
147	TU Peg	2.16	0.79	0.48	0.13	1.33	0.73	1.16	0.15
148	EP Aqr	⋯	⋯	⋯	⋯	⋯	⋯	⋯	⋯
149	SV Peg	⋯	⋯	⋯	⋯	⋯	⋯	⋯	⋯
150	CU Cep	0.88	0.40	1.30	0.42	0.34	0.31	2.17	0.87
151	OH104.9+2.4	⋯	4.51	0.22	0.20	⋯	3.89	0.31	0.07
152	V627 Cas	0.61	0.53	0.93	0.24	0.47	0.49	0.86	0.21
153	R Peg	0.10	0.84	0.46	0.12	0.06	1.03	0.59	0.14
154	BU And	0.02	0.80	0.56	0.25	0.00	0.54	0.81	0.26
155	R Cas	0.01	0.52	1.90	0.67	0.00	0.45	1.93	0.59

3.3. OH/IR Stars

No. 3. WX Psc (OH/IR, $\phi = 0.74$): Both blueshifted and redshifted components of the H_2O maser (peak velocities of –4.3 and 20.6 km s^{-1}) with respect to the stellar velocity ($V_{LSR} = 8.5$ km s^{-1}) were detected with peak intensities of 38.96 and 46.16 Jy on 2009 June 22 by J. Kim et al. (2010). In our observations, the blueshifted component, which peaked at –4.8 km s^{-1}, was detected showing a high intensity of 605.98 Jy. However the redshifted component, which peaked at 20.6 km s^{-1}, was detected showing 1.97 Jy (Figure 1). VLBI observations by N. Inomata et al. (2007) exhibited a polar-on bipolar outflow. The ^{29}SiO01, ^{29}SiO02, and ^{30}SiO01 appeared as a typical maser emission with triple spikes. The KaVA, which is the combined network of the KVN and VLBI Exploration of Radio Astrometry (VERA), integrated intensity maps of the SiO11 and SiO21 masers presented a typical ring-like structure (Y. Yun et al. 2016). The ring sizes of the SiO11 and SiO21 masers were measured to be about 0.66 mas (corresponding to 0.39 au at a distance of 590 pc), although the $v = 2$ maser spots are distributed a little further inward compared to those of the $v = 1$ (Y. Yun et al. 2016). ALMA ATOMIUM data (^{12}CO $J = 2$–1) exhibited a spiral-like structure and more evolved wind morphology as ATOMIUM Class III based on the binary interactions of stellar companions (L. Decin et al. 2020).

No. 106. V1366 Aql (OH/IR): This object shows both blueshifted and redshifted components of the H_2O maser (peak velocities of 9.0 and 33.1 km s^{-1}) with respect to the stellar velocity ($V_{LSR} = 20.4$ km s^{-1}) with similar peak intensities of 38.75 and 46.49 Jy on 2009 June 21 by J. Kim et al. (2010). In our observations, the redshifted component was detected with a high intensity of 39.84 Jy, while the blueshifted component was detected at 0.58 Jy (Figure 1). The ^{29}SiO01, ^{29}SiO02, and ^{30}SiO01 lines show a typical maser feature. The SiO23 maser was redshifted with respect to the peak emission of other masers, which appeared at the stellar velocity.

No. 117. OH44.79-2.31 (OH/IR): The H_2O maser shows a blueshifted component peaked at –80.7 km s^{-1} (OH maser: –84.7 km s^{-1}; D. Engels et al. 1986) with a peak intensity of 11.84 Jy and a redshifted component peaked at 60.8 km s^{-1} (OH maser: –60 km s^{-1}; D. Engels et al. 1986) with a peak intensity of 1.34 Jy. On 2009 June 21, the H_2O maser was not detected within 3σ levels of 1.66 Jy (J. Kim et al. 2010). The SiO11, SiO21, SiO12, SiO13, and ^{29}SiO01 masers show the blueshifted peak emission with respect to the stellar velocity, $V_{LSR} = -67.0$ km s^{-1}. The SiO01 does not show a spiky weak maser feature on the pedestal, while the 2014 July–August data by P. De Vicente et al. (2016) showed the spiky maser feature at –71.2 km s^{-1}. We changed the stellar velocity from –67.0 km s^{-1} (P. J. Benson et al. 1990) to –71.9 km s^{-1} based on Gaussian fitting of the SiO01, SiO02, and SiO03 lines and indicated it with a vertical solid line in Figure 1.

4. Discussion

In the statistical analysis, the following factors contribute to the uncertainty of the results: (1) As mentioned in the Introduction, stellar pulsation and maser variability are closely linked. Therefore, dividing the sources into Miras (with regular periods), SRs (semiregular), and OH/IR stars (with unknown periods) introduces limitations when comparing their maser properties. (2) Since the observations are snapshots taken at different optical phases rather than at a common pulsation phase for the entire sample, the resulting variability across the cycle may not be fully represented. (3) In sources with strong H_2O/SiO masers, the intensity ratio may be affected by saturation effects (M. J. Reid & J. M. Moran 1981). Nevertheless, the statistical approach based on simultaneous four-band KVN observations of about 50 objects in each class (SR, Mira, OH/IR) is expected to mitigate some of these uncertainties. Additionally, because the sample selection prioritized sources with relatively strong H_2O/SiO maser emission, the representativeness with respect to metallicity and Galactic location may be limited.

4.1. Ratios of the Peak and Integrated Flux Densities between SiO and H_2O Masers According to SRs, Miras, and OH/IR Stars

We analyzed the maser properties of SRs, Miras, and OH/IR stars of the ratios of the peak flux density (P.F) and integrated

Table 11
Peak Velocity

No.	Source	V_{peak} (km s^{-1})														
			^{30}SiO	^{29}SiO	SiO		^{29}SiO	SiO								
		H_2O	$J = 1$–0						$J = 2$–1				$J = 3$–2			HCN	SiS
(1)	(2)	(3)	$v = 0$ (4)	$v = 0$ (5)	$v = 0$ (6)	$v = 1$ (7)	$v = 2$ (8)	$v = 3$ (9)	$v = 0$ (10)	$v = 0$ (11)	$v = 1$ (12)	$v = 2$ (13)	$v = 0$ (14)	$v = 1$ (15)	$v = 2$ (16)	(17)	(18)
1	Y Cas	−18.3	⋯	−18.9	−15.8	−17.8	−18.5	−16.8	⋯	−16.2	−18.6	⋯	−14.8	−17.2	⋯	⋯	⋯
2	SY Scl	21.7	⋯	⋯	⋯	21.1	21.7	21.5	⋯	⋯	20.8	⋯	⋯	20.6	⋯	⋯	⋯
3	WX Psc	−4.8	10.6	−4.3	8.8	8.2	8.4	8.4	8.4	9.0	8.0	⋯	9.3	9.0	7.9	10.6	11.8
5	V669 Cas	⋯	⋯	⋯	⋯	⋯	−56.7	⋯	⋯	⋯	−56.7	⋯	⋯	⋯	⋯	⋯	⋯
6	SV Psc	⋯	⋯	⋯	⋯	⋯	⋯	⋯	⋯	6.1	⋯	⋯	5.9	⋯	⋯	⋯	⋯
7	V370 And	⋯	⋯	⋯	−1.2	−5.6	1.0	⋯	−1.7	−1.0	0.7	⋯	−1.9	⋯	⋯	⋯	⋯
8	omi Cet	⋯	⋯	⋯	46.5	47.3	46.9	⋯	⋯	46.3	46.9	⋯	47.3	46.5	⋯	⋯	⋯
9	YY Ari	−51.4	⋯	⋯	⋯	⋯	⋯	⋯	⋯	⋯	⋯	⋯	⋯	⋯	⋯	⋯	⋯
11	T Ari	−0.4	⋯	⋯	⋯	−1.6	−2.6	⋯	⋯	⋯	−1.3	⋯	−1.2	⋯	⋯	⋯	⋯
12	OH138.0+7.2	⋯	⋯	−38.7	⋯	−39.3	−36.6	⋯	⋯	⋯	−38.7	⋯	⋯	⋯	⋯	⋯	⋯
13	IK Tau	45.5	33.4	31.9	32.3	32.9	32.3	32.9	30.4	33.2	32.7	⋯	34.4	32.5	32.5	34.2	31.9
14	WZ Eri	⋯	⋯	⋯	⋯	10.0	9.7	⋯	⋯	⋯	9.7	⋯	⋯	⋯	⋯	⋯	⋯
15	IR Per	⋯	⋯	⋯	⋯	−20.7	−21.6	⋯	⋯	⋯	−21.6	⋯	−25.0	⋯	⋯	⋯	⋯
16	R Tau	13.2	⋯	⋯	⋯	14.7	15.4	⋯	⋯	12.9	14.5	⋯	14.1	15.0	⋯	⋯	⋯
17	IU Tau	⋯	⋯	−2.6	⋯	−2.1	−2.6	⋯	⋯	⋯	−2.6	−1.7	−0.8	0.1	−1.7	⋯	⋯
18	RX Tau	−43.8	⋯	⋯	⋯	−43.0	−44.1	⋯	⋯	−45.1	−42.4	⋯	−43.2	−39.2	−44.5	⋯	⋯
19	BX Eri	1.3	⋯	⋯	⋯	⋯	−2.4	⋯	⋯	0.8	−0.7	⋯	0.5	⋯	⋯	⋯	⋯
20	BZ Tau	⋯	⋯	⋯	⋯	15.3	14.9	⋯	⋯	⋯	15.6	⋯	⋯	13.9	⋯	⋯	⋯
21	TX Cam	⋯	9.9	9.1	10.5	9.3	9.1	⋯	6.8	10.5	10.1	12.8	10.9	10.1	12.8	14.6	13.3
22	NV Aur(230918)	⋯	1.3	2.6	1.0	3.6	2.1	4.5	4.1	2.4	0.5	2.8	4.5	0.3	2.5	8.3	⋯
	NV Aur(231013)	14.6	1.6	2.4	0.3	3.3	3.5	5.1	4.1	2.6	0.7	2.4	3.7	0.3	2.4	1.8	⋯
23	RX Lep	⋯	⋯	⋯	⋯	⋯	⋯	⋯	⋯	⋯	36.4	⋯	⋯	⋯	⋯	⋯	⋯
24	IRAS 05131+4530	⋯	⋯	⋯	⋯	−32.0	−32.5	⋯	⋯	⋯	⋯	⋯	⋯	⋯	⋯	⋯	⋯
25	BW Cam	46.9	49.9	50.5	49.4	48.4	47.9	47.5	⋯	48.7	48.8	⋯	50.5	50.5	47.5	⋯	⋯
26	GP Tau	3.9	⋯	⋯	⋯	0.1	0.1	⋯	⋯	⋯	3.5	⋯	⋯	⋯	⋯	⋯	⋯
27	RW Lep	−57.2	⋯	⋯	⋯	−57.0	−63.5	⋯	⋯	⋯	−58.0	⋯	⋯	⋯	⋯	⋯	⋯
28	BX Cam	−9.2	−0.3	−1.0	−3.1	−2.8	−1.0	0.3	−1.8	−1.7	−1.4	⋯	−0.9	−1.4	1.6	1.7	⋯
29	S Col	62.0	⋯	⋯	⋯	62.4	63.3	⋯	⋯	⋯	62.4	⋯	⋯	62.9	⋯	⋯	⋯
30	AW Tau	−8.8	⋯	⋯	⋯	−8.2	−8.8	−8.8	⋯	⋯	−7.1	⋯	⋯	−12.6	⋯	⋯	⋯
31	U Ori	−38.9	⋯	−36.7	−39.2	−35.3	−34.4	⋯	⋯	−38.9	−35.0	⋯	−37.5	−36.4	−35.3	⋯	⋯
32	U Lyn	−10.6	⋯	⋯	⋯	−12.6	−13.0	−12.6	⋯	−10.3	−10.3	⋯	−11.3	−9.9	⋯	⋯	⋯
33	IRC-10151	51.5	⋯	⋯	⋯	48.4	48.4	⋯	⋯	⋯	50.3	⋯	⋯	50.1	⋯	⋯	⋯
34	IRAS 07153-2411	⋯	⋯	58.2	⋯	62.0	59.9	⋯	⋯	⋯	58.6	⋯	⋯	⋯	⋯	⋯	⋯
35	IRAS 07180-1314	48.0	⋯	56.1	⋯	56.4	57.2	60.9	⋯	⋯	56.8	⋯	⋯	⋯	⋯	⋯	⋯
36	Z Pup	1.4	⋯	⋯	3.2	5.9	8.4	⋯	⋯	4.9	4.9	⋯	3.7	5.1	3.8	⋯	⋯
37	S Gem	94.3	⋯	⋯	⋯	97.6	98.6	⋯	⋯	⋯	98.0	⋯	⋯	92.0	⋯	⋯	⋯
38	R Cnc	14.5	⋯	15.1	13.4	17.2	17.6	⋯	⋯	14.1	14.1	⋯	14.3	13.8	16.8	⋯	⋯
39	RT Hya	⋯	⋯	⋯	⋯	⋯	24.6	⋯	⋯	⋯	25.5	⋯	27.0	⋯	⋯	⋯	⋯
40	V429 Hya	6.8	⋯	⋯	⋯	⋯	⋯	⋯	⋯	5.7	⋯	⋯	⋯	⋯	⋯	⋯	⋯
42	W Cnc	33.3	⋯	⋯	⋯	33.7	34.0	⋯	⋯	35.4	35.8	⋯	35.8	35.4	⋯	⋯	⋯
43	X Hya	27.7	⋯	⋯	⋯	24.0	28.7	⋯	⋯	27.5	26.2	⋯	27.7	26.4	28.9	⋯	⋯
44	IW Hya	45.6	⋯	39.7	39.1	40.5	40.0	43.3	44.4	39.9	39.9	⋯	39.8	39.1	37.5	⋯	⋯
45	R LMi	0.7	⋯	⋯	−0.6	6.0	5.6	0.3	⋯	−0.1	−1.5	⋯	0.9	−1.3	6.0	⋯	⋯

Table 11
(Continued)

No.	Source	V_{peak} (km s^{-1})														
			^{30}SiO	^{29}SiO	SiO		^{29}SiO	SiO							HCN	SiS
		H_2O			J = 1–0				J = 2–1				J = 3–2			
			$v = 0$	$v = 0$	$v = 0$	$v = 1$	$v = 2$	$v = 3$	$v = 0$	$v = 0$	$v = 1$	$v = 2$	$v = 0$	$v = 1$	$v = 2$	
(1)	(2)	(3)	(4)	(5)	(6)	(7)	(8)	(9)	(10)	(11)	(12)	(13)	(14)	(15)	(16)	(17)	(18)
46	R Leo	−0.3	⋯	−0.5	−0.5	−0.1	−9.9	−1.5	−1.1	1.9	1.5	⋯	−0.7	−1.1	1.1	0.2	⋯
47	V Leo	⋯	⋯	⋯	⋯	⋯	−30.5	⋯	⋯	⋯	⋯	⋯	⋯	⋯	⋯	⋯	⋯
48	R UMa	39.1	⋯	⋯	⋯	36.4	36.4	37.8	⋯	⋯	37.0	⋯	⋯	35.8	⋯	⋯	⋯
49	VX UMa	−49.6	⋯	⋯	⋯	−48.6	−48.6	⋯	⋯	−48.2	−51.5	⋯	−47.6	−51.9	−50.2	⋯	⋯
50	R Crt	10.4	⋯	⋯	10.9	15.0	14.4	⋯	11.8	11.5	13.6	⋯	11.7	14.6	⋯	⋯	⋯
52	AF Leo	8.5	⋯	⋯	⋯	⋯	⋯	⋯	⋯	9.4	−1.8	⋯	7.3	⋯	⋯	⋯	⋯
54	S Crt	42.8	⋯	⋯	⋯	⋯	⋯	⋯	⋯	⋯	38.1	⋯	⋯	⋯	⋯	⋯	⋯
55	Z UMa	⋯	⋯	⋯	⋯	−45.8	⋯	⋯	⋯	⋯	−45.2	⋯	⋯	−45.2	⋯	⋯	⋯
56	T Vir	7.8	⋯	⋯	⋯	7.2	6.4	⋯	⋯	⋯	7.2	⋯	⋯	⋯	⋯	⋯	⋯
57	BK Vir	17.6	⋯	⋯	15.8	19.0	18.6	⋯	⋯	17.2	15.0	⋯	17.8	⋯	⋯	⋯	⋯
59	RT Vir	16.9	⋯	⋯	17.3	12.3	11.3	⋯	18.6	18.3	12.1	⋯	18.2	12.9	⋯	⋯	⋯
60	SW Vir	⋯	⋯	⋯	−8.9	⋯	⋯	⋯	−15.0	−7.9	−8.9	⋯	−10.6	⋯	⋯	⋯	⋯
61	R Hya	−10.9	⋯	⋯	−10.5	−11.7	−6.2	⋯	−10.5	−10.1	−8.7	⋯	−9.7	−11.3	⋯	⋯	⋯
62	W Hya	43.9	41.5	40.2	39.0	41.4	41.1	40.2	44.7	40.8	41.5	⋯	40.2	41.3	41.3	38.5	⋯
63	AY Vir	−45.0	⋯	⋯	⋯	⋯	⋯	⋯	⋯	−39.5	⋯	⋯	−40.7	⋯	⋯	⋯	⋯
64	RU Hya	−3.8	⋯	⋯	⋯	−2.8	−3.8	⋯	⋯	⋯	−3.8	⋯	−3.7	−4.4	⋯	⋯	⋯
65	RX Boo	2.1	⋯	3.5	0.6	−2.0	0.2	⋯	0.1	1.5	−2.8	⋯	1.3	−4.6	⋯	3.0	⋯
66	RS Vir	−13.8	⋯	⋯	⋯	−9.5	−7.7	⋯	⋯	−14.2	−12.4	⋯	−13.2	−13.2	⋯	⋯	⋯
68	Y Cen	⋯	⋯	⋯	⋯	1.3	0.2	⋯	⋯	−0.8	0.4	⋯	−1.0	⋯	⋯	⋯	⋯
70	Y Lib	14.0	⋯	⋯	⋯	14.0	13.1	⋯	⋯	⋯	14.8	⋯	⋯	15.8	⋯	⋯	⋯
71	S CrB	−0.2	⋯	⋯	1.2	0.4	0.4	⋯	⋯	1.2	3.0	⋯	1.2	⋯	⋯	⋯	⋯
72	WX Ser	0.3	⋯	⋯	⋯	2.5	2.1	⋯	⋯	7.2	2.9	⋯	7.6	5.0	⋯	⋯	⋯
74	BG Ser	−2.9	⋯	⋯	⋯	−0.9	1.7	⋯	⋯	−2.4	−0.9	⋯	−1.3	−2.7	⋯	⋯	⋯
75	FS Lib	−3.3	⋯	⋯	⋯	−2.7	−3.1	⋯	⋯	⋯	−4.8	⋯	⋯	⋯	⋯	⋯	⋯
76	OH345.0+15.7	⋯	⋯	−2.3	⋯	−1.9	−2.7	⋯	1.8	−4.9	−2.3	⋯	−2.0	⋯	⋯	⋯	⋯
77	U Her	−16.6	⋯	−17.3	−16.2	−18.5	−19.1	−19.1	−17.7	−13.8	−16.3	⋯	−14.6	−17.3	−19.1	⋯	⋯
78	R UMi	−8.7	⋯	⋯	⋯	−6.0	−7.7	⋯	⋯	−7.7	−9.5	⋯	−8.5	⋯	⋯	⋯	⋯
79	T Oph	⋯	⋯	⋯	⋯	−30.3	−33.5	⋯	⋯	⋯	−32.7	⋯	−31.7	−32.9	⋯	⋯	⋯
80	V446 Oph	9.7	⋯	7.7	⋯	7.7	13.1	⋯	⋯	⋯	8.1	⋯	10.4	11.3	14.8	⋯	⋯
81	AH Dra	⋯	⋯	⋯	⋯	⋯	⋯	⋯	⋯	⋯	⋯	⋯	74.7	⋯	⋯	⋯	⋯
82	IRAS 16486–3014	49.4	⋯	⋯	⋯	52.1	53.1	57.1	⋯	⋯	52.1	⋯	⋯	50.9	⋯	⋯	⋯
83	V2108 Oph	8.7	14.0	13.3	15.2	13.9	9.9	12.5	11.7	16.9	13.9	⋯	16.9	14.2	17.4	⋯	⋯
84	V438 Oph	19.0	⋯	⋯	⋯	⋯	⋯	⋯	⋯	10.1	⋯	⋯	9.9	⋯	⋯	⋯	⋯
85	RV Ser	1.6	⋯	⋯	⋯	2.0	1.6	⋯	⋯	⋯	2.4	⋯	⋯	⋯	⋯	⋯	⋯
86	OH358.23+0.11	−3.1	⋯	⋯	−5.7	−11.8	−4.9	⋯	−3.9	⋯	−13.2	⋯	⋯	−10.8	⋯	⋯	⋯
87	IRAS 17436-1545	6.4	⋯	12.9	⋯	11.1	15.0	⋯	⋯	⋯	13.7	⋯	⋯	12.9	13.9	⋯	⋯
88	OH13.1+5.1	⋯	⋯	⋯	⋯	−64.6	−67.7	⋯	⋯	⋯	−65.2	⋯	⋯	⋯	⋯	⋯	⋯
89	VV Sgr	54.5	⋯	54.5	⋯	57.7	55.5	55.9	⋯	⋯	55.1	⋯	⋯	56.9	58.7	⋯	⋯
90	OH4.5-0.4	−141.3	⋯	⋯	⋯	−124.0	−123.8	⋯	⋯	⋯	−126.4	⋯	⋯	−124.8	⋯	⋯	⋯
91	WY Her	1.7	⋯	3.1	⋯	3.9	3.5	⋯	⋯	⋯	3.9	⋯	4.6	2.3	−0.9	⋯	⋯
92	V4120 Sgr	9.0	12.5	11.9	12.9	11.9	11.5	9.8	10.7	13.0	11.9	⋯	13.5	12.5	9.0	13.5	⋯
93	IRAS 18034-2441	⋯	⋯	⋯	⋯	5.6	5.0	⋯	⋯	⋯	9.3	⋯	⋯	⋯	⋯	⋯	⋯
94	IRAS 18035-2529	⋯	⋯	⋯	⋯	6.2	5.0	5.3	⋯	⋯	3.9	⋯	⋯	3.7	⋯	⋯	⋯

Table 11
(Continued)

No.	Source	V_{peak} (km s^{-1})														
			^{30}SiO	^{29}SiO	SiO		^{29}SiO	SiO							HCN	SiS
		H_2O			J = 1–0				J = 2–1				J = 3–2			
			$v = 0$	$v = 0$	$v = 0$	$v = 1$	$v = 2$	$v = 3$	$v = 0$	$v = 0$	$v = 1$	$v = 2$	$v = 0$	$v = 1$	$v = 2$	
(1)	(2)	(3)	(4)	(5)	(6)	(7)	(8)	(9)	(10)	(11)	(12)	(13)	(14)	(15)	(16)	(17)	(18)
95	V2302 Oph	−25.2	⋯	−15.7	⋯	−13.6	−13.6	−13.6	⋯	⋯	−15.3	⋯	−13.5	−15.4	⋯	⋯	⋯
96	IRAS 18099+3127	20.8	⋯	⋯	⋯	24.3	23.5	23.9	⋯	⋯	23.5	⋯	⋯	⋯	⋯	⋯	⋯
97	IRAS 18172–2305	⋯	⋯	⋯	⋯	10.1	9.7	⋯	⋯	⋯	10.3	⋯	⋯	⋯	⋯	⋯	⋯
98	V2571 Oph	−40.0	⋯	⋯	⋯	−38.6	−39.4	⋯	⋯	⋯	−36.3	⋯	⋯	⋯	⋯	⋯	⋯
99	V1111 Oph	−26.8	−29.1	−31.8	−31.3	−29.3	−29.1	⋯	−28.5	−31.0	−30.9	−25.2	−30.9	−31.3	−33.4	−29.3	⋯
100	IRAS 18395+0130	⋯	⋯	⋯	⋯	45.5	44.6	⋯	⋯	⋯	⋯	⋯	⋯	⋯	⋯	⋯	⋯
101	RW Lyr	−20.3	⋯	⋯	⋯	−20.7	−21.1	⋯	⋯	−21.1	−21.1	⋯	−21.9	−20.7	⋯	⋯	⋯
102	V439 Sct	29.3	⋯	⋯	⋯	48.4	45.4	48.0	⋯	⋯	44.8	⋯	43.4	44.6	⋯	⋯	⋯
103	IRAS 18476+0555	⋯	⋯	⋯	⋯	51.6	50.2	⋯	⋯	⋯	⋯	⋯	⋯	⋯	⋯	⋯	⋯
104	IRAS 18525+0210	⋯	⋯	⋯	⋯	66.6	66.2	⋯	⋯	⋯	⋯	⋯	⋯	⋯	⋯	⋯	⋯
106	V1366 Aql	34.9	20.7	20.7	17.5	18.9	19.9	27.0	22.4	20.2	21.1	⋯	20.0	20.3	26.6	⋯	⋯
107	IRAS 18578+0831	⋯	⋯	⋯	⋯	48.1	47.5	⋯	⋯	⋯	50.5	⋯	⋯	⋯	⋯	⋯	⋯
108	IRAS 19010+1307	44.9	⋯	⋯	⋯	57.9	57.9	⋯	⋯	⋯	59.5	⋯	⋯	⋯	⋯	⋯	⋯
109	V1367 Aql	⋯	⋯	⋯	⋯	146.4	146.0	⋯	⋯	⋯	⋯	⋯	⋯	⋯	⋯	⋯	⋯
110	OH43.9+1.2	38.0	⋯	46.9	⋯	52.6	52.2	53.0	⋯	⋯	46.5	⋯	⋯	⋯	47.5	⋯	⋯
111	V3880 Sgr	11.0	⋯	20.1	21.3	20.9	20.1	⋯	⋯	19.7	20.4	⋯	22.7	21.5	22.3	⋯	⋯
112	OH43.8+0.5	⋯	⋯	⋯	⋯	⋯	5.7	⋯	⋯	⋯	⋯	⋯	⋯	⋯	⋯	⋯	⋯
113	IRAS 19081+0322	⋯	⋯	⋯	⋯	41.8	41.0	41.4	⋯	⋯	42.2	⋯	⋯	42.4	⋯	⋯	⋯
114	IRAS 19183+1148	22.9	⋯	⋯	⋯	32.9	32.5	⋯	⋯	⋯	⋯	⋯	⋯	⋯	⋯	⋯	⋯
115	OH12.11-17.19	⋯	4.6	3.6	⋯	7.9	7.5	⋯	⋯	5.7	4.0	⋯	3.0	5.3	⋯	⋯	⋯
116	IRAS 19186+0315	−10.8	⋯	⋯	⋯	−20.3	−20.7	−19.9	⋯	⋯	−21.7	⋯	⋯	−20.3	⋯	⋯	⋯
117	OH44.79-2.31	−80.7	⋯	−72.0	−71.1	−72.8	−73.6	⋯	⋯	−72.4	−71.4	⋯	−72.3	−71.4	⋯	⋯	⋯
118	OH49.8-0.8	66.9	75.4	74.8	⋯	75.2	74.8	80.0	⋯	⋯	75.0	⋯	⋯	⋯	⋯	⋯	⋯
119	IRAS 19261+1435	⋯	⋯	⋯	⋯	46.9	46.2	⋯	⋯	⋯	46.9	⋯	⋯	⋯	⋯	⋯	⋯
120	IRAS 19265+3116	30.3	⋯	⋯	⋯	27.9	32.7	⋯	⋯	⋯	28.3	⋯	⋯	⋯	⋯	⋯	⋯
121	OH55.0+0.7	⋯	⋯	⋯	27.0	27.0	26.6	27.4	27.4	⋯	28.2	⋯	⋯	⋯	⋯	⋯	⋯
122	OH63.5+5.3	⋯	⋯	−39.9	⋯	−39.1	−41.3	⋯	⋯	⋯	−39.5	⋯	⋯	−40.3	⋯	⋯	⋯
123	UV Cyg	9.3	⋯	⋯	⋯	23.5	⋯	⋯	⋯	20.3	24.8	⋯	18.3	27.0	⋯	⋯	⋯
124	RT Aql	−29.1	⋯	⋯	−34.6	−30.3	−30.7	−30.7	⋯	−28.5	−29.5	⋯	−28.9	−29.7	−25.4	⋯	⋯
125	IRAS 19395+1827	−8.9	⋯	⋯	⋯	2.1	1.1	⋯	⋯	⋯	⋯	⋯	⋯	⋯	⋯	⋯	⋯
126	IRAS 19422+3506	−61.9	⋯	−51.1	−50.3	−49.5	−49.9	−49.5	⋯	−48.9	−50.3	⋯	−44.2	−49.9	−51.1	⋯	⋯
127	OH65.5+1.3	−16.2	⋯	⋯	⋯	−20.6	−19.4	⋯	⋯	⋯	−22.9	⋯	⋯	−23.7	⋯	⋯	⋯
128	IRAS 19495+0835	44.7	⋯	⋯	⋯	45.9	45..09	⋯	⋯	⋯	44.9	⋯	⋯	45.1	⋯	⋯	⋯
129	RR Aql	28.4	28.1	28.6	27.7	29.0	28.6	28.6	⋯	27.3	27.7	⋯	29.0	27.7	29.9	⋯	⋯
130	IRAS 19579+3223	⋯	⋯	3.8	⋯	4.9	4.5	6.3	⋯	⋯	4.9	⋯	⋯	5.5	⋯	⋯	⋯
131	Z Cyg	−148.1	⋯	⋯	⋯	−148.9	−148.9	⋯	⋯	⋯	−149.4	⋯	⋯	⋯	⋯	⋯	⋯
132	V718 Cyg	23.0	⋯	⋯	⋯	28.6	24.1	⋯	⋯	⋯	20.7	⋯	⋯	25.9	⋯	⋯	⋯
133	IRAS 20043+2653	⋯	⋯	⋯	⋯	−4.5	−5.7	−4.7	⋯	⋯	−5.5	⋯	⋯	⋯	⋯	⋯	⋯
134	SY Aql	−47.1	⋯	⋯	⋯	−47.3	−46.2	⋯	⋯	⋯	−47.5	⋯	⋯	⋯	⋯	⋯	⋯
135	AC Cyg	−28.8	⋯	⋯	⋯	⋯	⋯	⋯	⋯	−33.1	⋯	⋯	−32.9	⋯	⋯	⋯	⋯
136	IRAS 20123+0429	−17.0	⋯	⋯	⋯	−15.7	−16.4	⋯	⋯	⋯	−15.3	⋯	⋯	−15.5	⋯	⋯	⋯
137	T Mic	24.1	⋯	⋯	⋯	26.2	21.0	⋯	⋯	24.5	25.5	⋯	24.7	⋯	⋯	⋯	⋯

Table 11
(Continued)

No.	Source	V_{peak} (km s^{-1})															
			^{30}SiO	^{29}SiO	SiO		^{29}SiO	SiO								HCN	SiS
		H_2O	$J = 1$–0						$J = 2$–1				$J = 3$–2				
			$v = 0$	$v = 0$	$v = 0$	$v = 1$	$v = 2$	$v = 3$	$v = 0$	$v = 0$	$v = 1$	$v = 2$	$v = 0$	$v = 1$	$v = 2$		
(1)	(2)	(3)	(4)	(5)	(6)	(7)	(8)	(9)	(10)	(11)	(12)	(13)	(14)	(15)	(16)	(17)	(18)
138	OH63.3–10.2	−85.0	−72.5	−72.5	−76.0	−73.0	−72.5	⋯	⋯	⋯	−72.5	⋯	⋯	−72.8	−72.4	⋯	⋯
139	RU Cap	7.5	⋯	⋯	⋯	5.0	4.1	⋯	⋯	⋯	9.0	⋯	⋯	⋯	⋯	⋯	⋯
140	IRAS 20381+5001	−29.3	⋯	−40.6	⋯	−41.0	−41.4	⋯	⋯	⋯	−39.7	⋯	⋯	−40.1	⋯	⋯	⋯
141	IRAS 20403+3700	−58.4	⋯	−53.1	⋯	−53.4	−54.4	−53.5	⋯	⋯	−54.0	⋯	⋯	−52.7	⋯	⋯	⋯
142	OH73.8-6.3	⋯	⋯	⋯	⋯	−13.9	−14.8	⋯	⋯	⋯	⋯	⋯	⋯	⋯	⋯	⋯	⋯
143	V Aqr	⋯	⋯	⋯	⋯	29.9	⋯	⋯	⋯	⋯	−29.9	⋯	−26.4	⋯	⋯	⋯	⋯
144	OH83.42-0.89	−25.4	⋯	⋯	⋯	−38.6	−40.7	⋯	⋯	⋯	−40.3	⋯	⋯	⋯	⋯	⋯	⋯
145	V363 Cep	−29.4	⋯	−33.4	−37.2	−33.8	−34.4	⋯	⋯	⋯	−27.5	⋯	⋯	−32.9	−27.3	⋯	⋯
147	TU Peg	9.7	⋯	⋯	⋯	9.1	9.1	⋯	⋯	⋯	9.1	⋯	⋯	10.1	⋯	⋯	⋯
148	EP Aqr	⋯	⋯	⋯	−34.6	⋯	⋯	⋯	−33.6	−33.4	−34.1	⋯	−32.4	⋯	⋯	⋯	⋯
149	SV Peg	4.6	⋯	⋯	2.9	⋯	3.2	⋯	⋯	5.5	3.9	⋯	5.5	⋯	⋯	⋯	⋯
150	CU Cep	−47.6	⋯	⋯	⋯	−43.6	−43.6	⋯	⋯	⋯	−45.4	⋯	⋯	−40.9	⋯	⋯	⋯
151	OH104.9+2.4	⋯	⋯	−28.1	−26.8	−24.2	−25.7	⋯	⋯	−24.2	−25.1	⋯	−27.3	−24.7	⋯	⋯	⋯
152	V627 Cas	−52.2	⋯	−54.3	⋯	−53.5	−62.4	⋯	−53.3	⋯	−53.3	⋯	⋯	−52.3	−53.3	⋯	⋯
153	R Peg	24.0	⋯	⋯	⋯	24.9	25.1	19.3	⋯	24.4	25.1	⋯	23.5	25.1	⋯	⋯	⋯
154	BU And	−0.9	⋯	−4.7	⋯	−4.2	−5.1	⋯	−6.8	−3.3	−3.0	⋯	−3.7	0.7	−6.8	⋯	⋯
155	R Cas	24.7	24.7	23.9	24.7	23.3	22.2	⋯	28.7	25.6	24.2	⋯	25.1	27.7	26.5	29.6	⋯

Note. Peak velocity of 144 sources excluding 11 sources with no detection among the 19 molecular lines.

(This table is available in machine-readable form in the online article.)

Table 12
Full Width at Zero Power (FWZP)

No.	Source	FWZP															
			^{30}SiO	^{29}SiO	SiO				^{29}SiO	SiO			SiO				
					$J = 1$–0					$J = 2$–1			$J = 3$–2				
		H_2O	$v = 0$	$v = 0$	$v = 0$	$v = 1$	$v = 2$	$v = 3$	$v = 0$	$v = 0$	$v = 1$	$v = 2$	$v = 0$	$v = 1$	$v = 2$	HCN	SiS
(1)	(2)	(3)	(4)	(5)	(6)	(7)	(8)	(9)	(10)	(11)	(12)	(13)	(14)	(15)	(16)	(17)	(18)
1	Y Cas	7.11	⋯	3.10	10.75	13.86	13.68	7.11	⋯	14.77	11.30	⋯	15.73	6.19	⋯	⋯	⋯
2	SY Scl	4.74	⋯	⋯	⋯	10.39	9.12	2.74	⋯	⋯	7.80	⋯	⋯	6.56	⋯	⋯	⋯
3	WX Psc	35.00	10.94	11.31	37.01	16.59	19.33	13.68	18.23	40.65	15.49	⋯	40.62	15.65	11.70	44.12	41.98
5	V669 Cas	⋯	⋯	⋯	⋯	⋯	7.84	⋯	⋯	⋯	11.86	⋯	⋯	⋯	⋯	⋯	⋯
6	SV Psc	⋯	⋯	⋯	⋯	⋯	⋯	⋯	⋯	18.42	⋯	⋯	15.86	⋯	⋯	⋯	⋯
7	V370 And	⋯	⋯	⋯	19.88	12.94	6.76	⋯	16.59	19.33	18.59	⋯	19.88	⋯	⋯	⋯	⋯
8	omi Cet	⋯	⋯	⋯	3.64	16.04	5.02	⋯	⋯	9.48	19.14	⋯	8.20	11.85	⋯	⋯	⋯
9	YY Ari	6.68	⋯	⋯	⋯	⋯	⋯	⋯	⋯	⋯	⋯	⋯	⋯	⋯	⋯	⋯	⋯
11	T Ari	7.47	⋯	⋯	⋯	12.39	7.11	⋯	⋯	⋯	8.96	⋯	8.21	⋯	⋯	⋯	⋯
12	OH138.0+7.2	⋯	⋯	3.10	⋯	8.39	8.75	⋯	⋯	⋯	4.38	⋯	⋯	⋯	⋯	⋯	⋯
13	IK Tau	29.53	5.47	10.21	42.11	14.77	20.60	8.39	29.9	43.21	14.58	⋯	43.75	11.85	17.14	43.94	37.93
14	WZ Eri	⋯	⋯	⋯	⋯	13.49	13.13	⋯	⋯	⋯	5.65	⋯	⋯	⋯	⋯	⋯	⋯
15	IR Per	⋯	⋯	⋯	⋯	7.48	15.32	⋯	⋯	⋯	12.58	⋯	33.55	⋯	⋯	⋯	⋯
16	R Tau	6.20	⋯	⋯	⋯	9.48	10.40	⋯	⋯	6.38	9.48	⋯	12.22	6.01	⋯	⋯	⋯
17	IU Tau	⋯	⋯	5.65	⋯	9.11	15.68	⋯	⋯	⋯	12.21	14.95	10.39	7.29	4.01	⋯	⋯
18	RX Tau	4.48	⋯	⋯	⋯	17.25	11.14	⋯	⋯	14.19	20.31	⋯	10.58	13.63	3.62	⋯	⋯
19	BX Eri	6.78	⋯	⋯	⋯	⋯	5.55	⋯	⋯	⋯	5.55	⋯	19.12	⋯	⋯	⋯	⋯
20	BZ Tau	⋯	⋯	⋯	⋯	7.40	5.86	⋯	⋯	⋯	10.48	⋯	⋯	6.94	⋯	⋯	⋯
21	TX Cam	⋯	2.54	7.40	39.31	21.51	24.06	⋯	38.17	43.48	18.51	4.39	43.01	18.97	14.57	49.03	41.85
22	NV Aur(230918)	⋯	8.63	8.96	42.45	10.85	11.41	9.46	9.88	45.51	8.48	5.28	38.14	7.47	10.38	54.55	⋯
	NV Aur(231013)	3.24	7.17	10.64	36.08	12.72	11.33	8.32	14.10	36.31	8.78	3.93	39.09	6.02	11.10	41.17	⋯
23	RX Lep	⋯	⋯	⋯	⋯	⋯	⋯	⋯	⋯	⋯	11.48	⋯	11.56	⋯	⋯	⋯	⋯
24	IRAS 05131+4530	⋯	⋯	⋯	⋯	6.96	6.75	⋯	⋯	⋯	⋯	⋯	⋯	⋯	⋯	⋯	⋯
25	BW Cam	7.36	5.48	6.96	11.22	11.3	7.92	4.53	⋯	24.87	10.44	⋯	27.31	10.95	4.00	⋯	⋯
26	GP Tau	2.78	⋯	⋯	⋯	7.93	7.09	⋯	⋯	⋯	12.74	⋯	⋯	⋯	⋯	⋯	⋯
27	RW Lep	8.49	⋯	⋯	⋯	20.46	5.74	⋯	⋯	⋯	15.76	⋯	⋯	⋯	⋯	⋯	⋯
28	BX Cam	11.69	5.49	9.32	43.42	12.8	9.39	5.84	33.57	37.3	13.78	⋯	38.48	11.84	11.21	37.57	⋯
29	S Col	5.94	⋯	⋯	⋯	13.02	14.26	⋯	⋯	⋯	14.4	⋯	⋯	4.94	⋯	⋯	⋯
30	AW Tau	5.19	⋯	⋯	⋯	17.18	16.46	16.18	⋯	⋯	19.06	⋯	⋯	17.5	⋯	⋯	⋯
31	U Ori	5.56	⋯	4.49	5.01	14.87	18.37	⋯	⋯	9.08	15.03	⋯	12.63	14.09	3.75	⋯	⋯
32	U Lyn	7.69	⋯	⋯	⋯	16.43	12.39	5.24	⋯	18.67	17.57	⋯	16.39	8.97	⋯	⋯	⋯
33	IRC-10151	29.00	⋯	⋯	⋯	9.78	9.67	⋯	⋯	⋯	11.61	⋯	⋯	3.30	⋯	⋯	⋯
34	IRAS 07153-2411	⋯	⋯	7.28	⋯	11.12	10.52	⋯	⋯	⋯	7.88	⋯	⋯	⋯	⋯	⋯	⋯
35	IRAS 07180-1314	28.11	⋯	7.08	⋯	10.92	10.37	8.29	⋯	⋯	10.92	⋯	⋯	⋯	⋯	⋯	⋯
36	Z Pup	6.14	⋯	⋯	9.70	15.47	16.61	⋯	⋯	27.50	12.13	⋯	24.27	6.47	9.10	⋯	⋯
37	S Gem	6.87	⋯	⋯	⋯	18.60	11.12	⋯	⋯	⋯	18.6	⋯	⋯	5.06	⋯	⋯	⋯
38	R Cnc	5.05	⋯	3.98	10.92	13.43	11.15	⋯	⋯	9.90	14.56	⋯	8.87	8.65	5.12	⋯	⋯
39	RT Hya	⋯	⋯	⋯	⋯	⋯	10.11	⋯	⋯	⋯	8.90	⋯	8.29	⋯	⋯	⋯	⋯
40	V429 Hya	6.87	⋯	⋯	⋯	⋯	⋯	⋯	⋯	14.96	⋯	⋯	⋯	⋯	⋯	⋯	⋯
42	W Cnc	2.83	⋯	⋯	⋯	12.74	15.37	⋯	⋯	21.24	14.16	⋯	17.99	14.36	⋯	⋯	⋯
43	X Hya	5.06	⋯	⋯	⋯	11.50	10.49	⋯	⋯	16.79	10.05	⋯	11.53	7.28	9.92	⋯	⋯
44	IW Hya	4.05	⋯	5.66	25.28	11.32	12.34	9.50	27.51	29.12	14.16	⋯	31.75	13.35	7.88	⋯	⋯
45	R LMi	5.46	⋯	⋯	15.37	16.58	11.32	3.84	⋯	15.98	15.37	⋯	17.59	18.81	11.32	⋯	⋯

Table 12
(Continued)

No.	Source	FWZP														
			^{30}SiO	^{29}SiO	SiO				^{29}SiO	SiO			SiO			
		H_2O			$J = 1$–0					$J = 2$–1			$J = 3$–2			HCN	SiS
			$v = 0$	$v = 0$	$v = 0$	$v = 1$	$v = 2$	$v = 3$	$v = 0$	$v = 0$	$v = 1$	$v = 2$	$v = 0$	$v = 1$	$v = 2$		
(1)	(2)	(3)	(4)	(5)	(6)	(7)	(8)	(9)	(10)	(11)	(12)	(13)	(14)	(15)	(16)	(17)	(18)
46	R Leo	7.69	⋯	14.77	11.88	14.11	11.17	8.58	12.63	13.95	11.63	⋯	15.98	17.39	12.13	12.95	⋯
47	V Leo	⋯	⋯	⋯	⋯	⋯	6.47	⋯	⋯	⋯	⋯	⋯	⋯	⋯	⋯	⋯	⋯
48	R UMa	6.07	⋯	⋯	⋯	13.76	5.66	2.42	⋯	⋯	11.73	⋯	⋯	4.25	⋯	⋯	⋯
49	VX UMa	5.66	⋯	⋯	⋯	17.60	11.73	⋯	⋯	20.83	15.37	⋯	10.18	9.10	5.06	⋯	⋯
50	R Crt	10.62	⋯	⋯	22.04	19.42	17.44	⋯	23.28	21.92	23.58	⋯	23.06	27.30	⋯	⋯	⋯
52	AF Leo	14.16	⋯	⋯	⋯	⋯	⋯	⋯	⋯	21.42	11.32	⋯	14.10	⋯	⋯	⋯	⋯
54	S Crt	11.93	⋯	⋯	⋯	⋯	⋯	⋯	⋯	⋯	12.14	⋯	⋯	⋯	⋯	⋯	⋯
55	Z UMa	⋯	⋯	⋯	⋯	7.08	⋯	⋯	⋯	⋯	9.91	⋯	⋯	3.44	⋯	⋯	⋯
56	T Vir	4.66	⋯	⋯	⋯	8.29	7.89	⋯	⋯	⋯	9.51	⋯	⋯	⋯	⋯	⋯	⋯
57	BK Vir	7.08	⋯	⋯	32.96	9.31	6.68	⋯	⋯	12.54	18.41	⋯	21.44	⋯	⋯	⋯	⋯
59	RT Vir	13.35	⋯	⋯	20.62	8.09	14.36	⋯	15.17	22.84	21.23	⋯	22.44	5.87	⋯	⋯	⋯
60	SW Vir	⋯	⋯	⋯	17.8	⋯	⋯	⋯	21.64	17.4	16.58	⋯	19.82	⋯	⋯	⋯	⋯
61	R Hya	10.92	⋯	⋯	18.67	14.43	8.29	⋯	11.27	17.29	10.47	⋯	16.24	10.77	⋯	⋯	⋯
62	W Hya	10.36	8.22	6.69	15.74	10.62	13.91	8.85	8.97	14.16	16.5	⋯	15.11	10.68	12.01	25.57	⋯
63	AY Vir	14.86	⋯	⋯	⋯	⋯	⋯	⋯	⋯	14.56	⋯	⋯	9.91	⋯	⋯	⋯	⋯
64	RU Hya	5.83	⋯	⋯	⋯	17.49	11.83	⋯	⋯	⋯	15.95	⋯	12.58	17.33	⋯	⋯	⋯
65	RX Boo	8.70	⋯	20.76	19.21	27.96	7.95	⋯	19.90	23.33	27.10	⋯	19.04	16.30	⋯	24.01	⋯
66	RS Vir	4.95	⋯	⋯	⋯	10.84	8.84	⋯	⋯	10.81	11.45	⋯	14.79	8.40	⋯	⋯	⋯
68	Y Cen	⋯	⋯	⋯	⋯	14.58	8.40	⋯	⋯	17.50	13.21	⋯	16.99	⋯	⋯	⋯	⋯
70	Y Lib	8.24	⋯	⋯	⋯	9.65	6.11	⋯	⋯	⋯	6.70	⋯	⋯	7.29	⋯	⋯	⋯
71	S CrB	7.03	⋯	⋯	14.41	14.40	7.03	⋯	⋯	19.21	14.76	⋯	17.32	⋯	⋯	⋯	⋯
72	WX Ser	15.78	⋯	⋯	⋯	13.83	18.44	⋯	⋯	23.84	12.22	⋯	20.41	8.92	⋯	⋯	⋯
74	BG Ser	6.86	⋯	⋯	⋯	14.06	12.87	⋯	⋯	18.01	20.41	⋯	16.64	13.20	⋯	⋯	⋯
75	FS Lib	7.72	⋯	⋯	⋯	15.68	16.12	⋯	⋯	⋯	10.98	⋯	⋯	⋯	⋯	⋯	⋯
76	OH345.0+15.7	⋯	⋯	6.00	⋯	7.03	9.77	⋯	7.03	32.08	15.95	⋯	30.02	⋯	⋯	⋯	⋯
77	U Her	10.66	⋯	4.21	20.88	18.46	20.04	8.40	9.29	12.83	13.66	⋯	13.14	9.13	5.50	⋯	⋯
78	R UMi	8.06	⋯	⋯	⋯	8.74	6.51	⋯	⋯	11.15	10.29	⋯	9.6	⋯	⋯	⋯	⋯
79	T Oph	⋯	⋯	⋯	⋯	8.92	14.75	⋯	⋯	⋯	11.32	⋯	7.72	5.15	⋯	⋯	⋯
80	V446 Oph	14.21	⋯	5.49	⋯	15.61	22.13	⋯	⋯	⋯	13.38	⋯	17.16	11.66	13.90	⋯	⋯
81	AH Dra	⋯	⋯	⋯	⋯	⋯	⋯	⋯	⋯	⋯	⋯	⋯	14.07	⋯	⋯	⋯	⋯
82	IRAS 16486–3014	14.93	⋯	⋯	⋯	12.52	12.01	15.44	⋯	⋯	11.84	⋯	⋯	6.34	⋯	⋯	⋯
83	V2108 Oph	25.21	5.66	7.29	1.24	14.15	15.92	12.01	14.36	41.28	11.10	⋯	41.00	9.91	4.80	⋯	⋯
84	V438 Oph	23.15	⋯	⋯	⋯	⋯	⋯	⋯	⋯	13.48	⋯	⋯	16.83	⋯	⋯	⋯	⋯
85	RV Ser	15.78	⋯	⋯	⋯	6.06	5.79	⋯	⋯	⋯	18.35	⋯	⋯	⋯	⋯	⋯	⋯
86	OH358.23+0.11	24.02	⋯	⋯	16.74	39.97	31.90	⋯	11.94	⋯	40.13	⋯	⋯	24.02	⋯	⋯	⋯
87	IRAS 17436-1545	28.98	⋯	10.57	⋯	11.84	11.12	⋯	⋯	⋯	6.19	⋯	⋯	7.65	9.66	⋯	⋯
88	OH13.1+5.1	⋯	⋯	⋯	⋯	7.20	7.89	⋯	⋯	⋯	6.01	⋯	⋯	⋯	⋯	⋯	⋯
89	VV Sgr	4.46	⋯	3.51	⋯	16.82	10.58	2.74	⋯	⋯	12.99	⋯	⋯	12.70	14.75	⋯	⋯
90	OH4.5-0.4	11.15	⋯	⋯	⋯	13.04	12.01	⋯	⋯	⋯	16.47	⋯	⋯	9.60	⋯	⋯	⋯
91	WY Her	8.74	⋯	3.43	⋯	13.26	10.85	⋯	⋯	⋯	14.18	⋯	30.02	9.44	16.12	⋯	⋯
92	V4120 Sgr	3.43	3.95	4.59	28.47	13.72	14.93	4.81	29.16	31.56	21.1	⋯	39.1	19.73	17.50	48.72	⋯
93	IRAS 18034-2441	⋯	⋯	⋯	⋯	5.84	5.83	⋯	⋯	⋯	13.90	⋯	⋯	⋯	⋯	⋯	⋯
94	IRAS 18035-2529	⋯	⋯	⋯	⋯	11.15	8.06	4.97	⋯	⋯	7.04	⋯	⋯	5.49	⋯	⋯	⋯

Table 12
(Continued)

No.	Source	FWZP														
			^{30}SiO	^{29}SiO	SiO			^{29}SiO	SiO			SiO			HCN	SiS
		H_2O	$J = 1$–0					$J = 2$–1				$J = 3$–2				
			$v = 0$	$v = 0$	$v = 0$	$v = 1$	$v = 2$	$v = 3$	$v = 0$	$v = 0$	$v = 1$	$v = 2$	$v = 0$	$v = 1$	$v = 2$		
(1)	(2)	(3)	(4)	(5)	(6)	(7)	(8)	(9)	(10)	(11)	(12)	(13)	(14)	(15)	(16)	(17)	(18)
95	V2302 Oph	9.75	⋯	7.12	⋯	10.30	9.17	4.40	⋯	⋯	7.61	⋯	38.77	6.91	⋯	⋯	⋯
96	IRAS 18099+3127	12.35	⋯	⋯	⋯	10.46	9.60	3.77	⋯	⋯	8.92	⋯	⋯	⋯	⋯	⋯	⋯
97	IRAS 18172–2305	⋯	⋯	⋯	⋯	6.18	9.78	⋯	⋯	⋯	27.61	⋯	⋯	⋯	⋯	⋯	⋯
98	V2571 Oph	4.29	⋯	⋯	⋯	9.78	12.35	⋯	⋯	⋯	15.91	⋯	⋯	⋯	⋯	⋯	⋯
99	V1111 Oph	27.27	11.32	9.99	37.40	14.5	11.92	⋯	40.64	41.52	13.59	6.35	38.12	7.20	3.01	49.70	⋯
100	IRAS 18395+0130	⋯	⋯	⋯	⋯	13.38	10.29	⋯	⋯	⋯	⋯	⋯	⋯	⋯	⋯	⋯	⋯
101	RW Lyr	5.32	⋯	⋯	⋯	20.42	12.86	⋯	⋯	10.30	16.98	⋯	15.09	10.97	⋯	⋯	⋯
102	V439 Sct	10.63	⋯	⋯	⋯	9.95	13.55	5.66	⋯	⋯	7.03	⋯	32.59	8.92	⋯	⋯	⋯
103	IRAS 18476+0555	⋯	⋯	⋯	⋯	11.49	8.23	⋯	⋯	⋯	⋯	⋯	⋯	⋯	⋯	⋯	⋯
104	IRAS 18525+0210	⋯	⋯	⋯	⋯	7.21	12.18	⋯	⋯	⋯	⋯	⋯	⋯	⋯	⋯	⋯	⋯
106	V1366 Aql	32.87	5.14	5.98	45.63	12.28	14.15	12.03	15.61	36.54	9.61	⋯	38.43	7.89	7.27	⋯	⋯
107	IRAS 18578+0831	⋯	⋯	⋯	⋯	10.80	13.21	⋯	⋯	⋯	8.41	⋯	⋯	⋯	⋯	⋯	⋯
108	IRAS 19010+1307	10.11	⋯	⋯	⋯	12.33	9.51	⋯	⋯	⋯	8.7	⋯	⋯	⋯	⋯	⋯	⋯
109	V1367 Aql	⋯	⋯	⋯	⋯	8.23	8.05	⋯	⋯	⋯	⋯	⋯	⋯	⋯	⋯	⋯	⋯
110	OH43.9+1.2	25.89	⋯	8.29	⋯	11.13	10.11	4.86	⋯	⋯	8.49	⋯	⋯	⋯	8.59	⋯	⋯
111	V3880 Sgr	13.76	⋯	4.57	25.68	8.85	10.11	⋯	⋯	37.61	8.99	⋯	28.11	5.86	6.88	⋯	⋯
112	OH43.8+0.5	⋯	⋯	⋯	⋯	⋯	7.28	⋯	⋯	⋯	⋯	⋯	⋯	⋯	⋯	⋯	⋯
113	IRAS 19081+0322	⋯	⋯	⋯	⋯	7.49	5.65	⋯	⋯	⋯	3.85	⋯	⋯	3.64	⋯	⋯	⋯
114	IRAS 19183+1148	5.16	⋯	⋯	⋯	7.98	8.19	⋯	⋯	⋯	⋯	⋯	⋯	⋯	⋯	⋯	⋯
115	OH12.11-17.19	⋯	7.88	8.69	⋯	15.37	15.78	⋯	⋯	46.92	11.33	⋯	42.28	5.46	⋯	⋯	⋯
116	IRAS 19186+0315	6.07	⋯	⋯	⋯	10.11	10.92	9.51	⋯	⋯	11.94	⋯	⋯	14.15	⋯	⋯	⋯
117	OH44.79-2.31	8.29	⋯	3.28	36.81	9.91	10.41	⋯	⋯	35.39	7.68	⋯	36.40	6.37	⋯	⋯	⋯
118	OH49.8-0.8	5.58	3.60	4.67	⋯	12.28	13.42	4.21	⋯	⋯	7.28	⋯	⋯	⋯	⋯	⋯	⋯
119	IRAS 19261+1435	⋯	⋯	⋯	⋯	7.89	6.88	⋯	⋯	⋯	11.73	⋯	⋯	⋯	⋯	⋯	⋯
120	IRAS 19265+3116	13.14	⋯	⋯	⋯	10.05	9.50	⋯	⋯	⋯	10.05	⋯	⋯	⋯	⋯	⋯	⋯
121	OH55.0+0.7	⋯	⋯	⋯	4.45	9.09	8.70	7.28	7.49	⋯	4.86	⋯	⋯	⋯	⋯	⋯	⋯
122	OH63.5+5.3	⋯	⋯	3.52	⋯	7.89	10.11	⋯	⋯	⋯	6.47	⋯	⋯	2.11	⋯	⋯	⋯
123	UV Cyg	18.61	⋯	⋯	⋯	8.09	⋯	⋯	⋯	42.67	20.63	⋯	26.7	23.66	⋯	⋯	⋯
124	RT Aql	10.72	⋯	⋯	3.23	14.35	14.35	9.71	⋯	27.30	12.89	⋯	9.64	6.91	3.01	⋯	⋯
125	IRAS 19395+1827	11.73	⋯	⋯	⋯	10.32	9.71	⋯	⋯	⋯	⋯	⋯	⋯	⋯	⋯	⋯	⋯
126	IRAS 19422+3506	7.68	⋯	9.10	17.59	15.78	15.57	2.63	⋯	41.05	12.74	⋯	35.05	11.21	9.97	⋯	⋯
127	OH65.5+1.3	6.07	⋯	⋯	⋯	10.51	12.94	⋯	⋯	⋯	6.68	⋯	⋯	11.53	⋯	⋯	⋯
128	IRAS 19495+0835	12.13	⋯	⋯	⋯	14.75	13.76	⋯	⋯	⋯	12.34	⋯	⋯	4.05	⋯	⋯	⋯
129	RR Aql	6.87	5.05	4.24	17.39	10.54	13.14	4.05	⋯	14.1	8.42	⋯	15.09	9.25	6.18	⋯	⋯
130	IRAS 19579+3223	⋯	⋯	4.65	⋯	14.16	14.15	2.02	⋯	⋯	8.29	⋯	⋯	7.89	⋯	⋯	⋯
131	Z Cyg	3.03	⋯	⋯	⋯	4.86	4.04	⋯	⋯	⋯	4.77	⋯	⋯	⋯	⋯	⋯	⋯
132	V718 Cyg	11.73	⋯	⋯	⋯	17.39	11.12	⋯	⋯	⋯	19.88	⋯	⋯	25.77	⋯	⋯	⋯
133	IRAS 20043+2653	⋯	⋯	⋯	⋯	5.46	7.08	3.04	⋯	⋯	3.44	⋯	⋯	⋯	⋯	⋯	⋯
134	SY Aql	4.45	⋯	⋯	⋯	9.1	8.29	⋯	⋯	⋯	8.69	⋯	⋯	⋯	⋯	⋯	⋯
135	AC Cyg	3.04	⋯	⋯	⋯	⋯	⋯	⋯	⋯	10.52	⋯	⋯	9.30	⋯	⋯	⋯	⋯
136	IRAS 20123+0429	3.84	⋯	⋯	⋯	10.92	8.5	⋯	⋯	⋯	9.91	⋯	⋯	6.27	⋯	⋯	⋯
137	T Mic	6.68	⋯	⋯	⋯	15.16	12.34	⋯	⋯	10.92	15.57	⋯	11.32	⋯	⋯	⋯	⋯

Table 12
(Continued)

No.	Source	FWZP															
			^{30}SiO	^{29}SiO	SiO				^{29}SiO	SiO			SiO			HCN	SiS
		H_2O	$J = 1$–0							$J = 2$–1			$J = 3$–2				
			$v = 0$	$v = 0$	$v = 0$	$v = 1$	$v = 2$	$v = 3$	$v = 0$	$v = 0$	$v = 1$	$v = 2$	$v = 0$	$v = 1$	$v = 2$		
(1)	(2)	(3)	(4)	(5)	(6)	(7)	(8)	(9)	(10)	(11)	(12)	(13)	(14)	(15)	(16)	(17)	(18)
138	OH63.3–10.2	11.33	5.05	7.39	38.22	10.57	11.88	⋯	⋯	⋯	7.69	⋯	⋯	5.06	4.04	⋯	⋯
139	RU Cap	3.64	⋯	⋯	⋯	9.50	13.35	⋯	⋯	⋯	12.33	⋯	⋯	⋯	⋯	⋯	⋯
140	IRAS 20381+5001	27.10	⋯	30.53	⋯	16.79	12.94	⋯	⋯	⋯	9.91	⋯	⋯	6.67	⋯	⋯	⋯
141	IRAS 20403+3700	12.34	⋯	6.07	⋯	12.94	10.11	7.89	⋯	⋯	12.14	⋯	⋯	6.27	⋯	⋯	⋯
142	OH73.8-6.3	⋯	⋯	⋯	⋯	11.33	6.07	⋯	⋯	⋯	⋯	⋯	⋯	⋯	⋯	⋯	⋯
143	V Aqr	⋯	⋯	⋯	⋯	4.07	⋯	⋯	⋯	⋯	2.75	⋯	6.87	⋯	⋯	⋯	⋯
144	OH83.42-0.89	31.15	⋯	⋯	⋯	13.98	11.94	⋯	⋯	⋯	7.43	⋯	⋯	⋯	⋯	⋯	⋯
145	V363 Cep	15.98	⋯	9.51	23.86	17.19	16.98	⋯	⋯	⋯	20.02	⋯	⋯	15.77	5.86	⋯	⋯
147	TU Peg	4.45	⋯	⋯	⋯	12.34	7.08	⋯	⋯	⋯	12.14	⋯	⋯	7.07	⋯	⋯	⋯
148	EP Aqr	⋯	⋯	⋯	19.82	⋯	⋯	⋯	18.81	24.47	18.21	⋯	24.47	⋯	⋯	⋯	⋯
149	SV Peg	6.47	⋯	⋯	15.78	⋯	7.89	⋯	⋯	14.16	17.19	⋯	13.75	⋯	⋯	⋯	⋯
150	CU Cep	14.97	⋯	⋯	⋯	34.79	11.73	⋯	⋯	⋯	37.82	⋯	⋯	31.95	⋯	⋯	⋯
151	OH104.9+2.4	⋯	⋯	7.08	26.29	10.92	6.27	⋯	⋯	48.73	6.88	⋯	34.86	10.52	⋯	⋯	⋯
152	V627 Cas	15.77	⋯	6.27	⋯	21.44	18.40	⋯	8.29	⋯	18.81	⋯	⋯	18.6	8.29	⋯	⋯
153	R Peg	6.07	⋯	⋯	⋯	13.75	12.94	2.63	⋯	11.93	13.55	⋯	13.55	11.93	⋯	⋯	⋯
154	BU And	8.30	⋯	6.27	⋯	16.49	15.78	⋯	23.86	17.39	19.22	⋯	14.56	17.19	12.14	⋯	⋯
155	R Cas	5.87	3.03	7.78	19.72	15.62	19.15	⋯	22.29	29.73	14.95	⋯	30.13	18.00	21.93	26.49	⋯

Note. FWZP of 144 sources excluding 11 sources with no detection among the 19 molecular lines.

(This table is available in machine-readable form in the online article.)

Table 13
Best-fit Period and Optical Phase

No.	Source	Date	Period*	Best-fit Period	Best-fit Period	Phase (ϕ) Error ($\pm$)	Amplitude	R^2
1	Y Cas	230310	413.5	408.8	17.4	0.30	1.91	0.72
2	SY Scl	230918	411.0	416.5	4.3	0.86	1.84	0.65
4	V465 Cas	230326	60.0	866.7	83.3	0.38	0.25	0.26
8	omi Cet	230310	332.0	331.9	12.1	0.67	2.73	0.90
11	T Ari	230402	340.0	317.1	14.1	0.44	0.95	0.76
13	IK Tau	230310	470.0	461.2	5.0	0.15	1.54	0.55
16	R Tau	230310	320.9	325.7	11.9	0.46	2.40	0.72
18	RX Tau	230310	331.8	325.8	11.9	0.05	1.73	0.85
21	TX Cam	230301	557.4	552.8	7.0	0.64	1.56	0.57
28	BX Cam	230228	⋯	450.7	12.7	0.55	2.15	0.88
29	S Col	230430	325.9	325.7	8.3	0.85	2.08	0.81
31	U Ori	230301	368.3	374.2	10.9	0.66	2.65	0.75
32	U Lyn	230402	433.6	432.7	14.7	0.24	1.92	0.82
36	Z Pup	230415	508.6	515.8	18.1	0.90	2.86	0.80
37	S Gem	230326	293.2	294.8	6.0	0.15	2.01	0.68
38	R Cnc	230302	361.6	363.2	9.0	0.58	1.82	0.75
39	RT Hya	230326	290.0	252.4	1.4	0.88	0.39	0.29
41	RT Cnc	230302	60.0	509.7	35.3	0.82	2.84	0.68
42	W Cnc	230402	393.2	390.0	22.4	0.26	2.52	0.72
43	X Hya	230227	301.1	293.2	12.5	0.00	1.58	0.83
45	R LMi	230310	372.2	378.1	15.5	0.60	2.33	0.74
46	R Leo	230301	310.0	310.0	12.7	0.71	1.85	0.87
47	V Leo	230310	273.4	272.7	9.9	0.33	2.25	0.82
48	R UMa	230415	301.6	295.1	12.1	0.99	2.64	0.86
49	VX UMa	230415	215.2	388.6	11.6	0.08	2.23	0.80
55	Z UMa	230427	196.0	196.8	6.9	0.99	0.88	0.68
56	T Vir	230310	339.5	345.5	13.1	0.18	1.83	0.73
57	BK Vir	230415	150.0	250.3	7.1	0.00	0.29	0.43
61	R Hya	230415	388.9	361.1	14.2	0.07	1.04	0.71
62	W Hya	230326	361.0	383.1	24.8	0.02	1.53	0.80
64	RU Hya	230326	331.5	335.5	12.2	0.88	2.49	0.75
66	RS Vir	230419	354.0	359.0	14.1	0.37	2.04	0.81
67	V Boo	230430	257.0	267.0	6.4	0.69	0.65	0.60
71	S CrB	230430	360.3	359.5	14.1	0.72	3.13	0.71
72	WX Ser	230415	425.1	428.2	12.4	0.03	1.95	0.84
74	BG Ser	230326	143.0	381.9	7.6	0.19	0.82	0.79
77	U Her	230310	406.1	402.7	15.2	0.07	2.05	0.86
78	R UMi	230430	325.7	316.0	14.1	0.80	0.31	0.31
79	T Oph	230402	366.8	369.1	5.2	0.47	2.32	0.80
81	AH Dra	230430	158.0	193.4	1.4	0.20	0.22	0.19
85	RV Ser	230415	269.9	269.0	6.2	0.29	2.35	0.87
91	WY Her	230427	376.0	377.0	5.0	0.02	2.05	0.68
101	RW Lyr	230430	503.8	505.9	9.5	0.77	1.98	0.67
105	R Lyr	230430	46.0	46.6	0.3	0.74	0.06	0.10
124	RT Aql	230326	327.1	328.6	6.6	0.03	2.37	0.75
129	RR Aql	230310	394.8	400.6	10.2	0.93	2.19	0.78
131	Z Cyg	230427	263.7	263.4	4.3	0.57	2.25	0.82
134	SY Aql	230310	355.9	364.8	8.2	0.59	2.11	0.63
139	RU Cap	230326	347.4	347.2	3.3	0.74	1.87	0.74
143	V Aqr	230402	249.1	244.7	1.3	0.07	0.18	0.12
147	TU Peg	230515	321.6	323.4	5.6	0.34	2.12	0.77
149	SV Peg	230513	144.6	300.9	3.3	0.08	2.71	0.86
152	V627 Cas	230310	⋯	431.6	6.2	0.19		
153	R Peg	230415	378.1	380.8	19.6	0.75	2.09	0.88
154	BU And	230402	378.0	394.2	6.1	0.49	1.75	0.72
155	R Cas	230310	430.5	431.2	20.1	0.92	2.44	0.86

Note. Period*: existing period in Table 1. Best-fit period: using the optical data from the AAVSO, it is calculated by the Lomb–Scragle periodogram method. R^2: coefficient of determination.

Table 14
Noise rms Level

Source	Noise rms (Jy)																				
		^{30}SiO	^{29}SiO	SiO				^{29}SiO	SiO			SiO									
	H_2O	J = 1–0						J = 2–1				J = 3–2			HCN	SiS	SO_2	SO	CS	Tel.	Date
		v = 0	v = 0	v = 0	v = 1	v = 2	v = 3	v = 0	v = 0	v = 1	v = 2	v = 0	v = 1	v = 2							YYMMDD
(1)	(2)	(3)	(4)	(5)	(6)	(7)	(8)	(9)	(10)	(11)	(12)	(13)	(14)	(15)	(16)	(17)	(18)	(19)	(20)	(21)	(22)
Y Cas	0.20	0.09	0.11	0.11	0.11	0.11	0.09	0.22	0.22	0.22	0.22	0.39	0.44	0.44	0.25	0.22	0.22	0.22	0.17	YS	230310
SY Scl	0.41	0.14	0.23	0.24	0.22	0.27	0.17	0.73	0.59	0.59	0.66	2.06	1.93	2.22	0.65	0.58	0.41	2.43	0.40	US	230918
WX Psc	0.14	0.09	0.12	0.12	0.10	0.12	0.07	0.24	0.19	0.23	0.24	0.17	0.19	0.17	0.17	0.18	0.14	0.22	0.17	US	230302
V465 Cas	0.15	0.08	0.09	0.09	0.09	0.09	0.04	0.14	0.13	0.16	0.16	0.15	0.17	0.15	0.17	0.15	0.13	0.15	0.16	TN	230326
V669 Cas	0.12	0.08	0.10	0.12	0.12	0.12	0.07	0.24	0.19	0.22	0.24	0.17	0.19	0.17	0.20	0.15	0.11	0.20	0.17	US	230326
SV Psc	0.13	0.08	0.12	0.12	0.12	0.12	0.07	0.24	0.19	0.22	0.24	0.21	0.23	0.21	0.19	0.17	0.15	0.20	0.17	US	230326
V370 And	0.15	0.07	0.09	0.10	0.09	0.10	0.07	0.17	0.16	0.18	0.17	0.28	0.25	0.27	0.18	0.18	0.12	0.19	0.13	YS	230326
omi Cet	0.17	0.09	0.13	0.14	0.16	0.13	0.07	0.31	0.25	0.28	0.31	0.38	0.44	0.34	0.26	0.23	0.19	0.28	0.22	US	230310
YY Ari	0.10	0.08	0.10	0.10	0.09	0.09	0.08	0.20	0.16	0.21	0.19	0.26	0.25	0.29	0.20	0.18	0.15	0.19	0.14	YS	230402
Z Eri	0.22	0.14	0.22	0.21	0.24	0.21	0.14	0.37	0.38	0.39	0.39	0.55	0.55	0.63	0.39	0.37	0.26	0.44	0.35	TN	230923
T Ari	0.15	0.08	0.10	0.10	0.09	0.10	0.07	0.17	0.15	0.19	0.17	0.22	0.25	0.25	0.16	0.16	0.15	0.19	0.14	YS	230402
OH138.0+7.2	0.13	0.08	0.13	0.13	0.13	0.13	0.09	0.25	0.22	0.23	0.25	0.27	0.25	0.25	0.22	0.18	0.17	0.23	0.19	US	230402
IK Tau	0.16	0.08	0.07	0.15	0.09	0.07	0.04	0.17	0.15	0.16	0.17	0.17	0.19	0.17	0.17	0.18	0.15	0.16	0.16	TN	230310
WZ Eri	0.15	0.10	0.10	0.12	0.12	0.11	0.08	0.20	0.19	0.21	0.20	0.35	0.31	0.31	0.20	0.19	0.18	0.21	0.18	YS	230402
IR Per	0.15	0.08	0.09	0.09	0.09	0.09	0.04	0.16	0.13	0.16	0.16	0.15	0.17	0.13	0.16	0.17	0.15	0.15	0.14	TN	230402
R Tau	0.16	0.09	0.13	0.13	0.13	0.13	0.09	0.25	0.23	0.28	0.31	0.33	0.34	0.25	0.24	0.23	0.19	0.25	0.19	US	230310
IU Tau	0.16	0.08	0.10	0.11	0.11	0.11	0.08	0.20	0.21	0.22	0.22	0.35	0.36	0.36	0.20	0.25	0.17	0.21	0.14	YS	230310
RX Tau	0.16	0.09	0.09	0.10	0.10	0.10	0.05	0.16	0.15	0.18	0.16	0.19	0.19	0.17	0.17	0.18	0.15	0.18	0.17	TN	230310
BX Eri	0.25	0.09	0.10	0.10	0.10	0.10	0.05	0.17	0.16	0.16	0.17	0.17	0.17	0.17	0.17	0.17	0.14	0.16	0.17	TN	230326
BZ Tau	0.28	0.18	0.29	0.29	0.29	0.27	0.19	0.55	0.46	0.46	0.53	0.76	0.69	0.69	0.46	0.45	0.31	0.46	0.39	US	230310
TX Cam	0.15	0.08	0.10	0.09	0.09	0.10	0.07	0.11	0.18	0.19	0.09	0.28	0.29	0.31	0.18	0.18	0.15	0.21	0.16	YS	230301
NV Aur	0.44	0.38	0.11	0.11	0.13	0.13	0.14	0.17	0.24	0.34	0.36	0.59	0.50	0.50	0.41	0.40	0.63	0.69	0.69	YS	230918
	0.16	0.07	0.08	0.09	0.08	0.08	0.07	0.20	0.19	0.19	0.20	0.41	0.40	0.38	0.21	0.18	0.13	0.19	0.13	YS	231013
RX Lep	0.17	0.10	0.11	0.12	0.12	0.11	0.06	0.20	0.18	0.18	0.20	0.21	0.23	0.23	0.20	0.21	0.16	0.19	0.24	TN	230326
IRAS 05131+4530	0.15	0.08	0.09	0.10	0.10	0.09	0.07	0.19	0.16	0.19	0.17	0.22	0.27	0.27	0.20	0.19	0.15	0.19	0.14	YS	230402
BW Cam	0.13	0.08	0.12	0.13	0.13	0.13	0.07	0.25	0.17	0.22	0.22	0.17	0.19	0.17	0.19	0.17	0.14	0.23	0.20	US	230302
GP Tau	0.16	0.10	0.14	0.16	0.16	0.14	0.10	0.38	0.29	0.32	0.36	0.54	0.50	0.50	0.29	0.28	0.18	0.32	0.22	US	230326
RW Lep	0.19	0.10	0.16	0.16	0.29	0.14	0.10	0.33	0.28	0.28	0.35	0.38	0.40	0.34	0.26	0.23	0.19	0.29	0.24	US	230402
BX Cam	0.15	0.08	0.10	0.10	0.09	0.10	0.06	0.19	0.18	0.19	0.19	0.23	0.23	0.21	0.19	0.18	0.14	0.19	0.17	TN	230228
S Col	0.22	0.13	0.20	0.22	0.20	0.19	0.13	0.38	0.32	0.34	0.38	0.55	0.63	0.52	0.32	0.28	0.25	0.34	0.39	US	230430
AW Tau	0.16	0.08	0.09	0.09	0.10	0.09	0.05	0.17	0.15	0.18	0.17	0.13	0.19	0.17	0.17	0.17	0.15	0.18	0.19	TN	230310
U Ori	0.16	0.10	0.11	0.11	0.12	0.10	0.09	0.22	0.21	0.22	0.22	0.37	0.36	0.40	0.23	0.21	0.15	0.21	0.16	YS	230301
U Lyn	0.15	0.09	0.13	0.14	0.13	0.13	0.09	0.31	0.23	0.25	0.29	0.34	0.34	0.33	0.22	0.22	0.16	0.26	0.22	US	230402
IRC-10151	0.18	0.11	0.13	0.10	0.13	0.13	0.10	0.33	0.28	0.33	0.33	0.44	0.48	0.48	0.31	0.24	0.17	0.34	0.21	YS	230415
IRAS 07153-2411	0.19	0.10	0.11	0.10	0.11	0.10	0.06	0.19	0.19	0.20	0.19	0.25	0.25	0.27	0.17	0.19	0.18	0.18	0.22	TN	230415
IRAS 07180-1314	0.24	0.12	0.16	0.14	0.16	0.14	0.10	0.30	0.28	0.33	0.31	0.59	0.57	0.57	0.33	0.30	0.23	0.30	0.24	YS	230415
Z Pup	0.16	0.09	0.10	0.10	0.10	0.10	0.07	0.19	0.16	0.18	0.19	0.21	0.23	0.25	0.17	0.19	0.16	0.19	0.22	TN	230415
S Gem	0.19	0.10	0.19	0.19	0.20	0.19	0.10	0.42	0.32	0.37	0.40	0.54	0.52	0.55	0.34	0.28	0.22	0.36	0.27	US	230326
R Cnc	0.10	0.06	0.12	0.12	0.12	0.12	0.07	0.09	0.22	0.22	0.07	0.21	0.19	0.19	0.19	0.17	0.13	0.20	0.17	US	230302
RT Hya	0.17	0.10	0.10	0.10	0.10	0.10	0.06	0.17	0.16	0.18	0.19	0.19	0.17	0.19	0.19	0.18	0.15	0.18	0.22	TN	230326
V429 Hya	0.17	0.10	0.11	0.12	0.12	0.12	0.10	0.23	0.21	0.24	0.23	0.41	0.38	0.42	0.23	0.21	0.21	0.24	0.21	YS	230402
RT Cnc	0.14	0.08	0.07	0.09	0.09	0.07	0.04	0.16	0.15	0.15	0.14	0.13	0.13	0.13	0.13	0.15	0.13	0.15	0.14	TN	230302
W Cnc	0.14	0.06	0.09	0.09	0.07	0.09	0.05	0.14	0.13	0.15	0.16	0.15	0.15	0.13	0.14	0.17	0.15	0.13	0.14	TN	230402

Table 14
(Continued)

Source	Noise rms																				(Jy)
		^{30}SiO	^{29}SiO	SiO				^{29}SiO	SiO			SiO									
	H_2O	J = 1–0						J = 2–1				J = 3–2			HCN	SiS	SO_2	SO	CS	Tel.	Date
		$v = 0$	$v = 0$	$v = 0$	$v = 1$	$v = 2$	$v = 3$	$v = 0$	$v = 0$	$v = 1$	$v = 2$	$v = 0$	$v = 1$	$v = 2$							YYMMDD
(1)	(2)	(3)	(4)	(5)	(6)	(7)	(8)	(9)	(10)	(11)	(12)	(13)	(14)	(15)	(16)	(17)	(18)	(19)	(20)	(21)	(22)
X Hya	0.12	0.08	0.14	0.13	0.13	0.13	0.09	0.25	0.22	0.22	0.24	0.17	0.17	0.17	0.19	0.17	0.13	0.22	0.22	US	230227
IW Hya	0.17	0.11	0.13	0.12	0.12	0.12	0.10	0.22	0.18	0.21	0.22	0.30	0.31	0.31	0.20	0.21	0.16	0.24	0.23	YS	230227
R LMi	0.15	0.08	0.07	0.09	0.20	0.09	0.05	0.14	0.13	0.15	0.16	0.15	0.15	0.15	0.16	0.17	0.14	0.15	0.16	TN	230310
R Leo	0.15	0.09	0.11	0.11	0.12	0.11	0.09	0.19	0.19	0.19	0.19	0.24	0.25	0.29	0.20	0.16	0.13	0.19	0.20	YS	230301
V Leo	0.42	0.28	0.43	0.43	0.40	0.42	0.32	0.73	0.63	0.65	0.71	0.94	0.94	0.80	0.61	0.54	0.41	0.63	0.50	US	230310
R UMa	0.20	0.11	0.11	0.11	0.11	0.11	0.09	0.23	0.24	0.25	0.23	0.48	0.44	0.44	0.23	0.24	0.22	0.27	0.18	YS	230415
VX UMa	0.15	0.09	0.09	0.10	0.09	0.09	0.05	0.16	0.15	0.18	0.16	0.19	0.19	0.19	0.16	0.18	0.15	0.16	0.16	TN	230415
R Crt	0.19	0.10	0.12	0.12	0.12	0.12	0.07	0.22	0.20	0.19	0.20	0.25	0.25	0.23	0.20	0.19	0.17	0.19	0.26	TN	230310
ST UMa	0.21	0.10	0.12	0.12	0.12	0.12	0.09	0.22	0.22	0.24	0.23	0.41	0.44	0.44	0.25	0.24	0.20	0.27	0.16	YS	230415
AF Leo	0.14	0.08	0.09	0.10	0.09	0.09	0.05	0.17	0.18	0.16	0.14	0.15	0.15	0.15	0.17	0.17	0.15	0.15	0.14	TN	230415
II Hya	0.28	0.14	0.17	0.18	0.17	0.17	0.12	0.33	0.33	0.33	0.36	0.81	0.86	0.84	0.34	0.34	0.28	0.34	0.32	YS	230902
S Crt	0.15	0.09	0.10	0.09	0.10	0.11	0.08	0.19	0.18	0.21	0.20	0.22	0.29	0.29	0.20	0.19	0.16	0.21	0.18	YS	230227
Z UMa	0.14	0.08	0.13	0.12	0.13	0.12	0.07	0.24	0.20	0.23	0.25	0.19	0.21	0.19	0.20	0.17	0.15	0.22	0.17	US	230427
T Vir	0.23	0.12	0.16	0.17	0.17	0.17	0.11	0.30	0.30	0.31	0.28	0.52	0.54	0.52	0.36	0.30	0.23	0.31	0.24	YS	230310
BK Vir	0.15	0.08	0.09	0.09	0.09	0.09	0.05	0.17	0.13	0.15	0.16	0.17	0.15	0.15	0.16	0.17	0.14	0.15	0.14	TN	230415
TU CVn	0.11	0.13	0.12	0.12	0.12	0.12	0.12	0.14	0.13	0.13	0.14	0.19	0.19	0.19	0.14	0.14	0.11	0.13	0.14	TN	230430
RT Vir	0.15	0.08	0.10	0.10	0.11	0.10	0.05	0.22	0.18	0.20	0.20	0.19	0.19	0.21	0.19	0.22	0.15	0.19	0.22	TN	230430
SW Vir	0.21	0.13	0.22	0.22	0.20	0.20	0.14	0.38	0.32	0.34	0.40	0.44	0.48	0.48	0.32	0.32	0.23	0.36	0.29	US	230415
R Hya	0.22	0.11	0.14	0.14	0.13	0.14	0.11	0.30	0.25	0.28	0.28	0.52	0.54	0.52	0.31	0.27	0.23	0.28	0.27	YS	230415
W Hya	0.20	0.14	0.22	0.23	0.22	0.22	0.16	0.38	0.36	0.34	0.44	0.52	0.55	0.52	0.34	0.31	0.21	0.36	0.40	US	230326
AY Vir	0.16	0.09	0.10	0.10	0.09	0.09	0.05	0.16	0.15	0.16	0.17	0.17	0.17	0.19	0.17	0.18	0.15	0.19	0.19	TN	230310
RU Hya	0.19	0.11	0.11	0.12	0.12	0.12	0.07	0.20	0.19	0.19	0.20	0.23	0.25	0.25	0.19	0.19	0.19	0.19	0.26	TN	230326
RX Boo	0.15	0.09	0.12	0.14	0.13	0.13	0.07	0.29	0.25	0.25	0.29	0.27	0.29	0.25	0.22	0.18	0.16	0.22	0.17	US	230402
RS Vir	0.21	0.09	0.09	0.09	0.10	0.09	0.05	0.20	0.19	0.19	0.19	0.32	0.33	0.34	0.19	0.22	0.19	0.19	1.58	TN	230419
V Boo	0.42	0.24	0.30	0.31	0.29	0.29	0.24	0.62	0.58	0.57	0.55	0.89	0.96	1.07	0.60	0.58	0.42	0.52	0.41	YS	230430
Y Cen	0.23	0.12	0.16	0.14	0.14	0.16	0.12	0.28	0.27	0.31	0.27	0.54	0.50	0.57	0.28	0.27	0.22	0.27	0.30	YS	230402
RR UMi	0.15	0.09	0.12	0.13	0.13	0.13	0.07	0.27	0.22	0.26	0.27	0.29	0.31	0.31	0.22	0.20	0.16	0.26	0.17	US	230402
Y Lib	0.14	0.09	0.09	0.09	0.10	0.09	0.05	0.14	0.13	0.16	0.16	0.15	0.15	0.15	0.16	0.17	0.14	0.15	0.17	TN	230402
S CrB	0.16	0.08	0.13	0.12	0.13	0.12	0.09	0.27	0.23	0.25	0.29	0.25	0.25	0.23	0.22	0.22	0.17	0.23	0.17	US	230430
WX Ser	0.18	0.10	0.10	0.11	0.11	0.11	0.08	0.22	0.19	0.24	0.22	0.35	0.40	0.38	0.21	0.19	0.17	0.24	0.17	YS	230415
RR CrB	0.43	0.25	0.24	0.27	0.26	0.27	0.27	0.84	0.86	0.94	0.89	1.72	1.80	1.97	0.90	0.87	0.39	0.91	0.49	YS	230430
BG Ser	0.13	0.08	0.13	0.13	0.13	0.13	0.09	0.24	0.19	0.22	0.25	0.19	0.21	0.19	0.20	0.18	0.14	0.23	0.22	US	230326
FS Lib	0.38	0.29	0.43	0.40	0.40	0.40	0.35	1.04	0.60	0.63	0.75	0.88	0.90	0.88	0.60	0.54	0.42	0.63	0.56	US	230415
OH345.0+15.7	0.17	0.11	0.17	0.20	0.19	0.19	0.13	0.33	0.25	0.25	0.31	0.29	0.33	0.31	0.24	0.23	0.18	0.26	0.37	US	230326
U Her	0.31	0.20	0.21	0.22	0.23	0.24	0.19	0.44	0.42	0.48	0.47	0.83	0.80	0.84	0.47	0.43	0.32	0.46	0.34	YS	230310
R UMi	0.20	0.10	0.13	0.14	0.14	0.16	0.10	0.29	0.28	0.28	0.33	0.38	0.40	0.38	0.26	0.25	0.23	0.28	0.24	US	230430
T Oph	0.15	0.09	0.10	0.15	0.10	0.09	0.06	0.16	0.15	0.15	0.16	0.13	0.15	0.15	0.16	0.17	0.13	0.16	0.16	TN	230402
V446 Oph	0.16	0.09	0.10	0.10	0.10	0.10	0.05	0.17	0.16	0.16	0.16	0.17	0.19	0.17	0.17	0.18	0.16	0.16	0.17	TN	230326
AH Dra	0.17	0.11	0.16	0.17	0.16	0.16	0.12	0.33	0.26	0.29	0.31	0.46	0.46	0.40	0.27	0.28	0.22	0.28	0.27	US	230430
IRAS 16486–3014	0.28	0.14	0.18	0.19	0.19	0.18	0.13	0.39	0.34	0.39	0.37	0.98	1.00	0.96	0.39	0.39	0.28	0.40	0.31	YS	230415
V2108 Oph	0.12	0.08	0.13	0.14	0.13	0.13	0.07	0.24	0.22	0.22	0.25	0.17	0.19	0.19	0.19	0.18	0.13	0.22	0.22	US	230326
V438 Oph	0.15	0.08	0.09	0.09	0.09	0.09	0.05	0.16	0.15	0.15	0.16	0.15	0.17	0.15	0.16	0.17	0.15	0.16	0.14	TN	230402
RV Ser	0.18	0.09	0.10	0.10	0.10	0.10	0.06	0.20	0.19	0.18	0.19	0.25	0.23	0.23	0.22	0.17	0.17	0.18	0.20	TN	230415

Table 14
(Continued)

Source	Noise rms																				(Jy)
		^{30}SiO	^{29}SiO	SiO				^{29}SiO	SiO			SiO									
	H_2O	J = 1–0						J = 2–1				J = 3–2			HCN	SiS	SO_2	SO	CS	Tel.	Date
		$v = 0$	$v = 0$	$v = 0$	$v = 1$	$v = 2$	$v = 3$	$v = 0$	$v = 0$	$v = 1$	$v = 2$	$v = 0$	$v = 1$	$v = 2$							YYMMDD
(1)	(2)	(3)	(4)	(5)	(6)	(7)	(8)	(9)	(10)	(11)	(12)	(13)	(14)	(15)	(16)	(17)	(18)	(19)	(20)	(21)	(22)
OH358.23+0.11	0.26	0.12	0.16	0.17	0.16	0.13	0.13	0.30	0.25	0.30	0.25	0.52	0.54	0.52	0.28	0.28	0.22	0.27	0.32	YS	230402
IRAS 17436-1545	0.18	0.09	0.10	0.11	0.10	0.10	0.06	0.17	0.18	0.19	0.19	0.23	0.21	0.23	0.22	0.21	0.17	0.19	0.20	TN	230402
OH13.1+5.1	0.16	0.10	0.16	0.16	0.14	0.16	0.12	0.31	0.29	0.28	0.33	0.36	0.38	0.40	0.24	0.25	0.18	0.29	0.24	US	230402
VV Sgr	0.18	0.10	0.10	0.12	0.11	0.10	0.06	0.19	0.18	0.19	0.17	0.21	0.19	0.21	0.20	0.19	0.16	0.19	0.20	TN	230326
OH4.5-0.4	0.22	0.10	0.12	0.12	0.12	0.12	0.07	0.20	0.19	0.20	0.23	0.25	0.29	0.31	0.20	0.22	0.21	0.20	0.23	TN	230415
WY Her	0.14	0.09	0.16	0.14	0.16	0.16	0.09	0.31	0.25	0.25	0.27	0.23	0.23	0.23	0.24	0.22	0.16	0.25	0.20	US	230427
V4120 Sgr	0.16	0.09	0.10	0.10	0.10	0.10	0.06	0.17	0.16	0.16	0.17	0.19	0.19	0.19	0.17	0.18	0.16	0.19	0.23	TN	230310
IRAS 18034-2441	0.28	0.14	0.17	0.19	0.16	0.18	0.14	0.36	0.33	0.33	0.37	0.67	0.73	0.77	0.29	0.33	0.29	0.36	0.32	YS	230310
IRAS 18035-2529	0.17	0.14	0.20	0.20	0.20	0.20	0.14	0.38	0.28	0.32	0.38	0.33	0.38	0.33	0.29	0.25	0.21	0.29	0.32	US	230427
V2302 Oph	0.17	0.09	0.10	0.11	0.09	0.10	0.06	0.17	0.16	0.18	0.16	0.19	0.21	0.21	0.19	0.19	0.16	0.19	0.19	TN	230430
IRAS 18099+3127	0.15	0.08	0.13	0.13	0.13	0.13	0.07	0.25	0.20	0.23	0.25	0.29	0.27	0.27	0.22	0.18	0.17	0.25	0.17	US	230430
IRAS 18172–2305	0.16	0.10	0.11	0.12	0.12	0.12	0.07	0.19	0.18	0.18	0.19	0.19	0.21	0.21	0.20	0.19	0.16	0.19	0.24	TN	230402
V2571 Oph	0.22	0.13	0.20	0.22	0.20	0.20	0.17	0.42	0.34	0.37	0.44	0.50	0.54	0.50	0.37	0.32	0.22	0.34	0.32	US	230310
V1111 Oph	0.16	0.08	0.09	0.09	0.09	0.07	0.05	0.17	0.15	0.18	0.16	0.17	0.17	0.17	0.17	0.17	0.15	0.16	0.17	TN	230310
IRAS 18395+0130	0.24	0.10	0.13	0.13	0.13	0.14	0.09	0.25	0.27	0.27	0.25	0.52	0.46	0.50	0.29	0.27	0.23	0.27	0.23	YS	230310
RW Lyr	0.15	0.08	0.12	0.12	0.12	0.12	0.07	0.27	0.22	0.23	0.25	0.21	0.25	0.21	0.20	0.18	0.16	0.23	0.17	US	230430
V439 Sct	0.19	0.11	0.19	0.19	0.19	0.19	0.13	0.35	0.28	0.29	0.36	0.36	0.40	0.36	0.32	0.28	0.19	0.31	0.30	US	230501
IRAS 18476+0555	0.33	0.19	0.22	0.23	0.21	0.24	0.18	0.52	0.43	0.48	0.50	0.81	0.75	0.84	0.47	0.51	0.34	0.46	0.32	YS	230430
IRAS 18525+0210	0.33	0.20	0.24	0.26	0.24	0.26	0.22	0.50	0.46	0.51	0.47	0.89	0.88	0.96	0.59	0.43	0.33	0.48	0.47	YS	230430
R Lyr	0.16	0.08	0.09	0.09	0.09	0.09	0.05	0.19	0.15	0.15	0.17	0.17	0.19	0.19	0.19	0.17	0.11	0.16	0.14	TN	230430
V1366 Aql	0.15	0.08	0.12	0.13	0.12	0.12	0.09	0.27	0.23	0.23	0.27	0.23	0.25	0.23	0.24	0.18	0.16	0.22	0.17	US	230430
IRAS 18578+0831	0.15	0.09	0.14	0.16	0.14	0.14	0.10	0.31	0.25	0.26	0.29	0.29	0.31	0.29	0.22	0.22	0.18	0.26	0.22	US	230430
IRAS 19010+1307	0.19	0.09	0.10	0.10	0.10	0.10	0.06	0.20	0.19	0.20	0.20	0.23	0.23	0.19	0.20	0.21	0.16	0.19	0.19	TN	230430
V1367 Aql	0.17	0.08	0.10	0.09	0.09	0.09	0.05	0.17	0.18	0.18	0.19	0.17	0.21	0.17	0.17	0.18	0.16	0.18	0.16	TN	230430
OH43.9+1.2	0.16	0.09	0.10	0.10	0.10	0.09	0.07	0.20	0.18	0.19	0.19	0.26	0.31	0.31	1.68	0.18	0.15	0.19	0.16	YS	230501
V3880 Sgr	0.21	0.10	0.13	0.13	0.13	0.13	0.10	0.23	0.21	0.25	0.22	0.41	0.42	0.42	0.23	0.22	0.21	0.25	0.24	YS	230402
OH43.8+0.5	0.21	0.14	0.23	0.23	0.23	0.22	0.16	0.40	0.34	0.39	0.44	0.44	0.48	0.48	0.36	0.34	0.22	0.39	0.27	US	230501
IRAS 19081+0322	0.19	0.09	0.10	0.10	0.10	0.10	0.05	0.20	0.19	0.20	0.20	0.26	0.29	0.29	0.20	0.21	0.21	0.20	0.17	TN	230415
IRAS 19183+1148	0.15	0.10	0.14	0.14	0.14	0.16	0.10	0.29	0.26	0.29	0.29	0.27	0.27	0.25	0.22	0.23	0.16	0.28	0.19	US	230427
OH12.11-17.19	0.22	0.11	0.12	0.12	0.13	0.13	0.10	0.27	0.24	0.25	0.23	0.46	0.44	0.48	0.25	0.21	0.21	0.25	0.25	YS	230501
IRAS 19186+0315	0.20	0.13	0.20	0.20	0.19	0.19	0.16	0.38	0.31	0.32	0.40	0.29	0.46	0.44	0.31	0.28	0.21	0.31	0.30	US	230501
OH44.79-2.31	0.38	0.10	0.10	0.11	0.11	0.10	0.08	0.30	0.24	0.24	0.28	0.74	0.73	0.75	0.31	0.31	0.32	0.27	0.27	YS	230918
OH49.8-0.8	0.17	0.08	0.09	0.10	0.10	0.10	0.08	0.19	0.18	0.19	0.20	0.30	0.31	0.36	0.21	0.18	0.17	0.21	0.16	YS	230501
IRAS 19261+1435	0.15	0.10	0.14	0.16	0.14	0.14	0.10	0.27	0.25	0.28	0.31	0.31	0.29	0.29	0.24	0.22	0.17	0.25	0.23	US	230427
IRAS 19265+3116	0.19	0.10	0.14	0.16	0.14	0.14	0.10	0.31	0.26	0.26	0.31	0.33	0.34	0.31	0.24	0.20	0.17	0.26	0.24	US	230501
OH55.0+0.7	0.27	0.10	0.11	0.12	0.12	0.11	0.10	0.30	0.27	0.27	0.30	0.65	0.61	0.69	0.28	0.28	0.23	0.27	0.21	YS	230513
OH63.5+5.3	0.18	0.08	0.10	0.10	0.10	0.10	0.07	0.20	0.19	0.21	0.19	0.37	0.40	0.38	0.21	0.21	0.18	0.22	0.14	YS	230513
UV Cyg	0.15	0.09	0.14	0.14	0.14	0.16	0.10	0.29	0.25	0.26	0.31	0.27	0.31	0.29	0.26	0.22	0.17	0.26	0.23	US	230430
RT Aql	0.13	0.08	0.13	0.13	0.13	0.13	0.09	0.24	0.20	0.22	0.24	0.17	0.19	0.19	0.20	0.20	0.13	0.22	0.19	US	230326
IRAS 19395+1827	0.22	0.11	0.13	0.14	0.13	0.13	0.11	0.30	0.27	0.28	0.28	0.57	0.59	0.63	0.29	0.25	0.22	0.30	0.23	YS	230430
IRAS 19422+3506	0.22	0.10	0.09	0.10	0.10	0.11	0.06	0.20	0.18	0.20	0.22	0.34	0.38	0.36	0.20	0.21	0.21	0.20	0.17	TN	230515
OH65.5+1.3	0.16	0.08	0.09	0.09	0.09	0.07	0.05	0.17	0.15	0.15	0.16	0.15	0.23	0.23	0.16	0.15	0.16	0.16	0.14	TN	230513
IRAS 19495+0835	0.18	0.20	0.11	0.11	0.10	0.10	0.06	0.17	0.18	0.19	0.17	0.17	0.23	0.21	0.19	0.19	0.17	0.19	0.22	TN	230310

Table 14
(Continued)

Source	Noise rms																			(Jy)
		^{30}SiO	^{29}SiO	SiO				^{29}SiO	SiO			SiO								
	H_2O	J = 1–0						J = 2–1				J = 3–2			HCN	SiS	SO_2	SO	CS	Tel.	Date
		v = 0	v = 0	v = 0	v = 1	v = 2	v = 3	v = 0	v = 0	v = 1	v = 2	v = 0	v = 1	v = 2							YYMMDD
(1)	(2)	(3)	(4)	(5)	(6)	(7)	(8)	(9)	(10)	(11)	(12)	(13)	(14)	(15)	(16)	(17)	(18)	(19)	(20)	(21)	(22)
RR Aql	0.20	0.10	0.17	0.17	0.16	0.16	0.10	0.36	0.28	0.31	0.35	0.46	0.42	0.44	0.27	0.26	0.19	0.31	0.24	US	230310
IRAS 19579+3223	0.20	0.09	0.11	0.11	0.11	0.11	0.08	0.22	0.21	0.24	0.23	0.44	0.42	0.50	0.25	0.22	0.18	0.22	0.16	YS	230513
Z Cyg	0.16	0.10	0.16	0.16	0.16	0.16	0.10	0.31	0.25	0.29	0.29	0.27	0.29	0.33	0.24	0.23	0.18	0.28	0.24	US	230427
V718 Cyg	0.17	0.09	0.11	0.11	0.11	0.10	0.06	0.19	0.18	0.18	0.19	0.23	0.23	0.25	0.19	0.19	0.18	0.20	0.20	TN	230430
IRAS 20043+2653	0.24	0.11	0.12	0.12	0.14	0.12	0.07	0.23	0.23	0.24	0.22	0.30	0.31	0.31	0.24	0.25	0.23	0.22	0.19	TN	230513
SY Aql	0.28	0.11	0.16	0.17	0.17	0.16	0.13	0.31	0.30	0.30	0.31	0.70	0.69	0.71	0.33	0.30	0.29	0.31	0.30	YS	230310
AC Cyg	0.20	0.11	0.19	0.19	0.17	0.19	0.13	0.38	0.34	0.37	0.38	0.48	0.54	0.54	0.32	0.31	0.23	0.37	0.22	US	230515
IRAS 20123+0429	0.17	0.09	0.10	0.10	0.09	0.10	0.06	0.19	0.18	0.18	0.17	0.21	0.21	0.19	0.17	0.18	0.16	0.19	0.17	TN	230402
T Mic	0.21	0.11	0.17	0.20	0.19	0.19	0.13	0.38	0.34	0.34	0.38	0.52	0.57	0.50	0.31	0.26	0.22	0.34	0.32	US	230402
OH63.3–10.2	0.21	0.09	0.11	0.10	0.10	0.11	0.07	0.23	0.22	0.22	0.19	0.26	0.34	0.36	0.22	0.23	0.18	0.20	0.20	TN	230415
RU Cap	0.17	0.10	0.10	0.11	0.12	0.11	0.06	0.19	0.18	0.19	0.17	0.21	0.23	0.21	0.19	0.21	0.16	0.22	0.23	TN	230326
IRAS 20381+5001	0.22	0.11	0.12	0.12	0.12	0.12	0.07	0.26	0.22	0.23	0.23	0.34	0.34	0.38	0.26	0.23	0.21	0.23	0.23	TN	230415
IRAS 20403+3700	0.18	0.08	0.10	0.10	0.10	0.10	0.08	0.22	0.22	0.22	0.23	0.44	0.44	0.48	0.25	0.22	0.20	0.24	0.16	YS	230513
OH73.8-6.3	0.27	0.13	0.09	0.15	0.14	0.12	0.12	0.27	0.24	0.24	0.22	0.38	0.40	0.40	0.24	0.25	0.27	0.23	0.17	TN	230513
V Aqr	0.15	0.08	0.09	0.09	0.09	0.09	0.05	0.16	0.13	0.15	0.16	0.15	0.15	0.17	0.16	0.15	0.14	0.16	0.16	TN	230402
OH83.42-0.89	0.17	0.07	0.09	0.09	0.09	0.09	0.07	0.17	0.18	0.19	0.19	0.30	0.33	0.38	0.20	0.18	0.15	0.19	0.14	YS	230515
V363 Cep	0.25	0.13	0.14	0.14	0.15	0.12	0.07	0.29	0.26	0.24	0.26	0.47	0.52	0.52	0.29	0.30	0.23	0.26	0.29	TN	230415
W Cyg	0.22	0.10	0.13	0.13	0.14	0.13	0.10	0.27	0.25	0.25	0.27	0.48	0.50	0.54	0.25	0.24	0.21	0.27	0.21	YS	230430
TU Peg	0.18	0.09	0.09	0.10	0.09	0.09	0.06	0.20	0.18	0.20	0.20	0.30	0.29	0.29	0.20	0.19	0.18	0.19	0.16	TN	230515
EP Aqr	0.20	0.09	0.10	0.11	0.10	0.10	0.09	0.22	0.19	0.22	0.22	0.41	0.40	0.44	0.23	0.21	0.18	0.21	0.16	YS	230415
SV Peg	0.22	0.09	0.14	0.13	0.13	0.14	0.09	0.33	0.28	0.29	0.33	0.46	0.52	0.52	0.26	0.26	0.22	0.28	0.22	US	230513
CU Cep	0.17	0.08	0.11	0.10	0.11	0.11	0.11	0.22	0.19	0.22	0.20	0.35	0.38	0.42	0.21	0.21	0.18	0.22	0.16	YS	230415
OH104.9+2.4	0.17	0.09	0.09	0.09	0.10	0.09	0.05	0.17	0.16	0.16	0.16	0.19	0.21	0.19	0.19	0.18	0.17	0.16	0.17	TN	230402
V627 Cas	0.16	0.09	0.09	0.10	0.10	0.09	0.05	0.17	0.15	0.16	0.16	0.15	0.19	0.19	0.16	0.17	0.16	0.16	0.19	TN	230310
R Peg	0.15	0.08	0.13	0.19	0.12	0.13	0.09	0.29	0.19	0.20	0.25	0.25	0.29	0.25	0.22	0.20	0.16	0.23	0.22	US	230415
BU And	0.14	0.08	0.12	0.12	0.13	0.13	0.07	0.25	0.20	0.22	0.27	0.23	0.25	0.21	0.20	0.20	0.16	0.22	0.17	US	230402
R Cas	0.15	0.08	0.12	0.13	0.13	0.12	0.07	0.25	0.23	0.25	0.27	0.27	0.31	0.25	0.22	0.20	0.16	0.25	0.17	US	230310

Note. Column (1): observed source name. Column (2)–(20): noise rms level. Column (21): observed telescopes (Yonsei=YS, Ulsan=US, Tamna=TN). Column (22): observed date. Source list order follows Table 1.

Table 15
Average Values of Peak and Integrated Flux Ratios of H_2O w.r.t. SiO11 and SiO12 Masers

Type(Sample)	$\frac{P.F(H_2O)}{P.F(SiO11)}$		$\frac{I.F(H_2O)}{I.F(SiO11)}$		$\frac{P.F(H_2O)}{P.F(SiO12)}$		$\frac{I.F(H_2O)}{I.F(SiO12)}$	
	Ave.	SD	Ave.	SD	Ave.	SD	Ave.	SD
SR(17)	8.45	16.02	7.68	16.77	4.22	8.73	1.50	3.35
Mira(50)	0.85	1.08	0.45	0.51	0.97	1.16	0.46	0.45
OH/IR(24)	0.93	1.02	0.58	0.47	1.26	1.18	0.89	0.80

Note. Ave.: Average; SD: Standard Deviation.

flux density (I.F) between the H_2O and SiO masers in Tables 9 and 10.

We selected sample sources where the H_2O, SiO11, and SiO12 masers were all detected. These samples included 16 SRs, 50 Miras, and 24 OH/IR stars. The average values and standard deviations (SD) of each ratio were estimated and summarized in Table 15. For the SRs, the ratios $P.F(H_2O)/P.F(SiO11)$ and $I.F(H_2O)/I.F(SiO11)$ are 8.45 and 7.68, respectively, which are significantly larger than those of the Miras ($P.F(H_2O)/P.F(SiO11) = 0.85$, $I.F(H_2O)/I.F(SiO11) = 0.45$) and OH/IR stars ($P.F(H_2O)/P.F(SiO11) = 0.93$, $I.F(H_2O)/I.F(SiO11) = 0.58$), though they show larger SD due to several samples with very high ratios (Figure 2). In the case of the Miras and OH/IR stars, these values are not much different; however, the value of the OH/IR star is slightly larger. These results show the same trend as the early results of J. Kim et al. (2010, 2014). We also estimated the ratios of the H_2O maser to the SiO12, which is strongly emitted in the SRs compared to the SiO11 maser. Similar trends remained unchanged, but in the case of the SRs, the ratios became slightly smaller due to stronger intensities of the SiO12 maser. It is possible to trace the SiO maser properties of variable stars associated with their evolutionary sequences through the period–luminosity (P-L) diagram (P. Wood et al. 1999; M. Trabucchi et al. 2017). A variable star moves the P-L sequence from left to right in the P-L diagram as evolution progresses. The SRs occupy left-side sequences (mainly A and B in Figure 1 of M. Trabucchi et al. 2017) due to the overtone mode and Mira variables being located on sequence C due to the fundamental mode. The overtone mode of SRb becomes gradually stable as it approaches the fundamental mode of Mira variables (M. Trabucchi et al. 2017). Using CO vibrational emission data (K. H. Hinkle et al. 1984), L. A. Willson (2000) reported that Mira variables have larger amplitude and fundamental mode photospheric shocks while SR variables show smaller, overtone shocks. These shocks play an important role for the collisional pumping of SiO masers suggested by E. Humphreys et al. (2002). X. Chen et al. (2007) and J. Su et al. (2012) supported the circumstellar shock model of E. Humphreys et al. (2002) by VLBI observations. Therefore, as SRs evolve into Miras, the strength of the SiO maser may increase due to stronger photospheric shocks, which drive more material outward and raise the gas density, including that of SiO. In addition, based on SiO maser observations on SRs, J. Alcolea et al. (1999) suggested that most SRs with $\Delta m_v < 2.5$ lack the necessary conditions for SiO maser emission because the inner envelope associated with pulsation is not sufficiently developed. For Miras and OH/IR stars, the ratios of $P.F(H_2O)/P.F(SiO11, SiO12)$ and $I.F(H_2O)/I.F(SiO11, SiO12)$ increase in the OH/IR stars shown in Table 15. This is evident in the increased mass loss observed in more evolved OH/IR stars (P. Bowers & W. Hagen 1984). The extended atmosphere and envelope of OH/IR stars may not reach the physical conditions of SiO maser emission, which requires higher density and temperature compared to H_2O masers. Thus, the H_2O maser becomes relatively stronger than the SiO maser. This result was also reported by J. Kim et al. (2014). In addition, J. Kim et al. (2014) reported that the peak intensity of an H_2O maser rapidly increases around optical maximum phases compared to a SiO maser due to a shock wave effect caused by stellar pulsation. In Figure 2, we plot the histograms for number versus $P.F(H_2O)/P.F(SiO11)$ and $I.F(H_2O)/I.F(SiO11)$, and $P.F(H_2O)/P.F(SiO12)$ and $I.F(H_2O)/I.F(SiO12)$ ratios with a bin interval of 0.5 according to the SRs, Miras, and OH/IR stars. These histograms illustrate the distribution of the P.F and I.F ratios. The SRs exhibit a broader distribution compared to the Miras and OH/IR stars. Among the SRs, the optical variability type SRb stars RX Boo, R Crt, and UV Cyg stand out with notably high ratios. R Crt shows a $P.F(H_2O)/P.F(SiO11)$ ratio of 63.1 and an $I.F(H_2O)/I.F(SiO11)$ ratio of 56.92, while RX Boo exhibits a P.F ratio of 27.70 and an I.F ratio of 8.78 and UV Cyg shows a $P.F(H_2O)/P.F(SiO11)$ ratio of 48.97 and an $I.F(H_2O)/I.F(SiO11)$ of 2.93. These values are significantly higher than the SR average P.F and I.F ratios of 8.45 and 7.68, respectively. Additionally, RW Lep (for P.F) and RT Vir (for I.F) are noteworthy for their high ratios. This distribution suggests that the H_2O maser is typically stronger in SRs than in Miras and OH/IR stars. In contrast, the distributions of the P.F and I.F ratios in Miras and OH/IR stars appear similar. However, in the Miras, more than half are distributed between 0 and 0.5 (31/50 in the P.F and 34/50 in the I.F), and in OH/IR, 11/24(45.8%) in the P.F and 14/24(58.3%) in the I.F are distributed between these values. In the case of SR, the SD is approximately twice as large as the average Table 15, which is attributed to the presence of a few specific outliers in Figure 2. The SDs in Mira and OH/IR stars are slightly larger than average values. Therefore, as shown in Figure 2, since the ratios of $P.F(H_2O)/P.F(SiO11)$ and $I.F(H_2O)/I.F(SiO11)$ in both Mira and OH/IR stars are distributed below 5, the averages of only these ratios below 5 in SR (13 samples) is 1.36 and 0.62, respectively. The average values of these ratios in SR are still higher than those in Mira and OH/IR stars suggesting that the H_2O maser in SR is stronger than the SiO maser.

4.2. Different Characteristics in Various SiO Transition Masers according to Evolutionary Phases of SRs, Miras, and OH/IR Stars

Here, we focused on investigating the characteristic change of the intensity ratio in various SiO transition masers according to the evolutionary phases of the SRs, Miras, and OH/IR stars. Table 10 presents the peak and integrated flux ratios of the SiO21, SiO12, and SiO13 masers with respect to the SiO11 maser, regardless of H_2O maser detection. The selected samples included 11 SRs, 46 Miras, and 23 OH/IR stars for the SiO21, SiO12, and SiO13 maser detected sources. We estimated the average values of their peak and integrated flux ratios and summarized them in Table 16, and Figures 4 to 6 present the histograms of the P.F and I.F.

4.2.1. Peak and Integrated Flux Ratios of the SiO21 Maser with Respect to the SiO11 Maser: P.F(SiO21)/P.F(SiO11) and I.F(SiO21)/I.F(SiO11), and the SiO31 Detected Sources

The P.F and I.F ratios of P.F(SiO21)/P.F(SiO11) and I.F(SiO21)/I.F(SiO11) in the OH/IR stars are much larger than

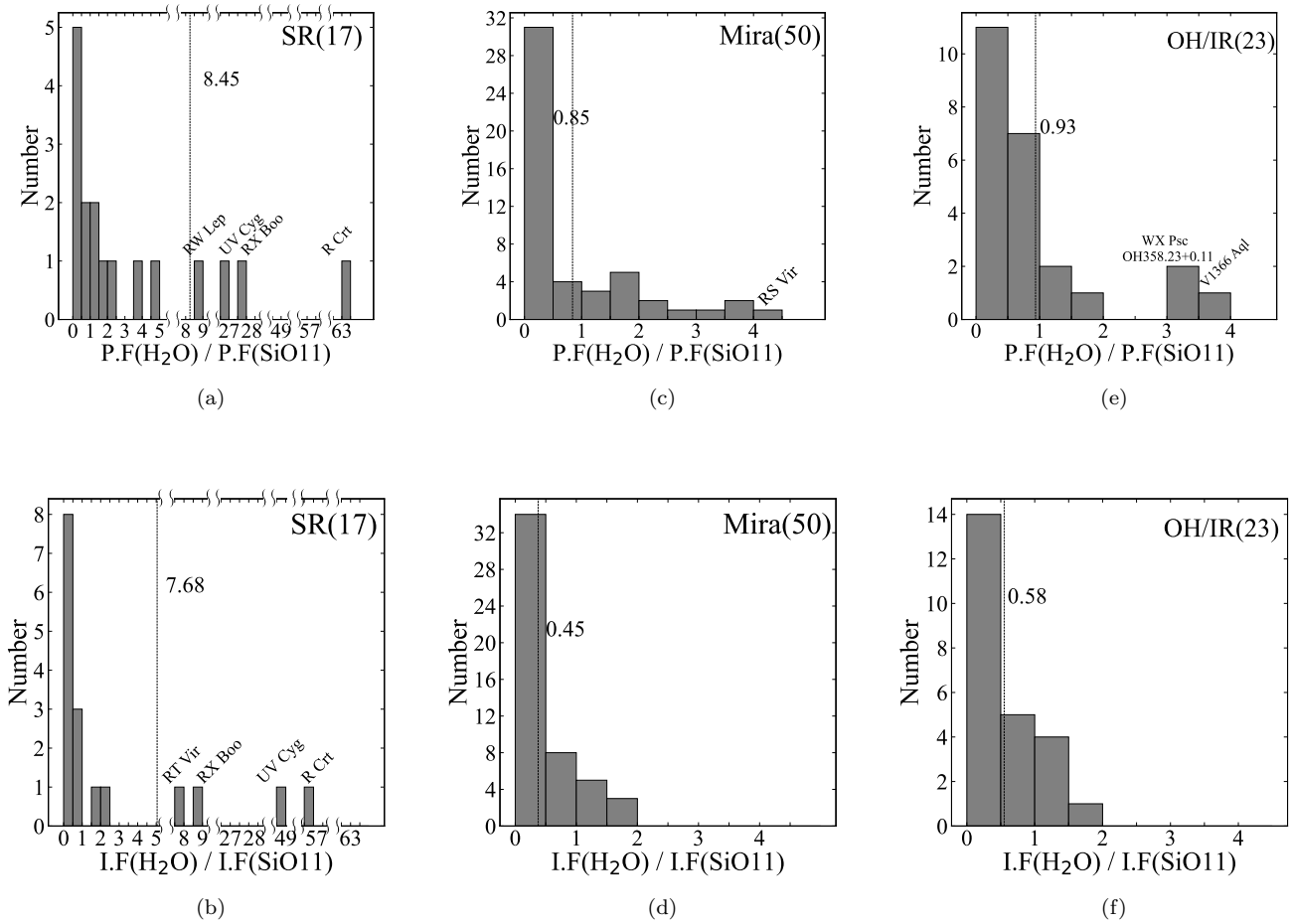

Figure 2. Distributions of the peak and integrated flux (P.F and I.F) ratios of H_2O to SiO11. (a) P.F of SR, (b) I.F of SR, (c) P.F of Mira, (d) I.F of Mira, (e) P.F of OH/IR, and (f) I.F of OH/IR. The solid line represents the average value of the flux ratios.

Table 16
Average and SD Values of P.F and I.F Ratios w.r.t. SiO11 Maser for SiO Detected Sources

Type(Sample)	$\frac{\text{P.F(SiO21)}}{\text{P.F(SiO11)}}$		$\frac{\text{P.F(SiO12)}}{\text{P.F(SiO11)}}$		$\frac{\text{P.F(SiO13)}}{\text{P.F(SiO11)}}$		$\frac{\text{I.F(SiO21)}}{\text{I.F(SiO11)}}$		$\frac{\text{I.F(SiO12)}}{\text{I.F(SiO11)}}$		$\frac{\text{I.F(SiO13)}}{\text{I.F(SiO11)}}$	
	Ave.	SD	Ave.	SD	Ave.	SD	Ave.	SD	Ave.	SD	Ave.	SD
SR(11)	0.99	0.90	1.60	0.82	0.42	0.20	0.87	0.60	2.57	2.51	0.45	0.32
Mira(46)	0.94	0.51	1.02	0.65	0.36	0.34	0.80	0.35	1.02	0.62	0.26	0.21
OH/IR(23)	1.43	1.50	1.07	0.81	0.60	0.58	1.36	1.12	0.88	0.64	0.38	0.47

those in the Miras and SRs shown in Table 16. The $v = 2$, $J = 1$–0 maser requires a much higher excitation temperature than the $v = 1$ (i.e., 1800 K for the $v = 1$ corresponding to 8 μm and 3600 K for the $v = 2$ corresponding to 4 μm; M. Elitzur 1982). So the relatively strong excitation of the SiO21 maser would be due to the development of the hot dust shell close to the star according to the evolution from Miras to OH/IR stars (S.-H. Cho & J. Kim 2012; S. Ramstedt et al. 2012; D.-H. Yoon et al. 2014). In Figure 3, we have plotted the distribution of the P.F(SiO21)/P.F(SiO11) and I.F(SiO21)/I.F (SiO11) ratios as histograms. The majority of the Miras and OH/IR stars are distributed between 0.5 and 1, while the SRs show a more even distribution between 0 and 0.5 and 0.5 and 1. The distributions of the P.F and I.F in the OH/IR stars are broader than those in the Miras and SRs. Among the SRs, RX Boo consistently exhibited high ratios. Sources with particularly large values are marked with their names.

Table 17 presents the list of sources where the SiO31 maser was detected. Table 17 provides the peak and integrated flux ratios of the SiO21 maser to the SiO11 maser (P.F(SiO21)/P.F (SiO11), I.F(SiO21)/I.F(SiO11)) and of the SiO12 maser to the SiO11 maser (P.F(SiO12)/P.F(SiO11), I.F(SiO12)/I.F (SiO11)) for both detected and undetected sources, categorized by the SRs, Miras, and OH/IR stars. The SiO31 maser transition requires a high temperature larger than 5000 K for its excitation from the vibrational ground state and a high density of $\geqslant 10^{10}$ cm^{-3} (J.-F. Desmurs et al. 2014). In addition, this maser is strongly variable (A. P. Lane 1982) and concentrated around the maximum stellar pulsation phase (S.-H. Cho et al. 1996).

As shown in Table 17, the majority of the SiO31 maser is detected from the Miras and OH/IR stars. In Table 17, the peak and integrated flux ratios of the P.F(SiO21)/P.F(SiO11) and I.F(SiO21)/I.F(SiO11) for SiO31 maser detected sources

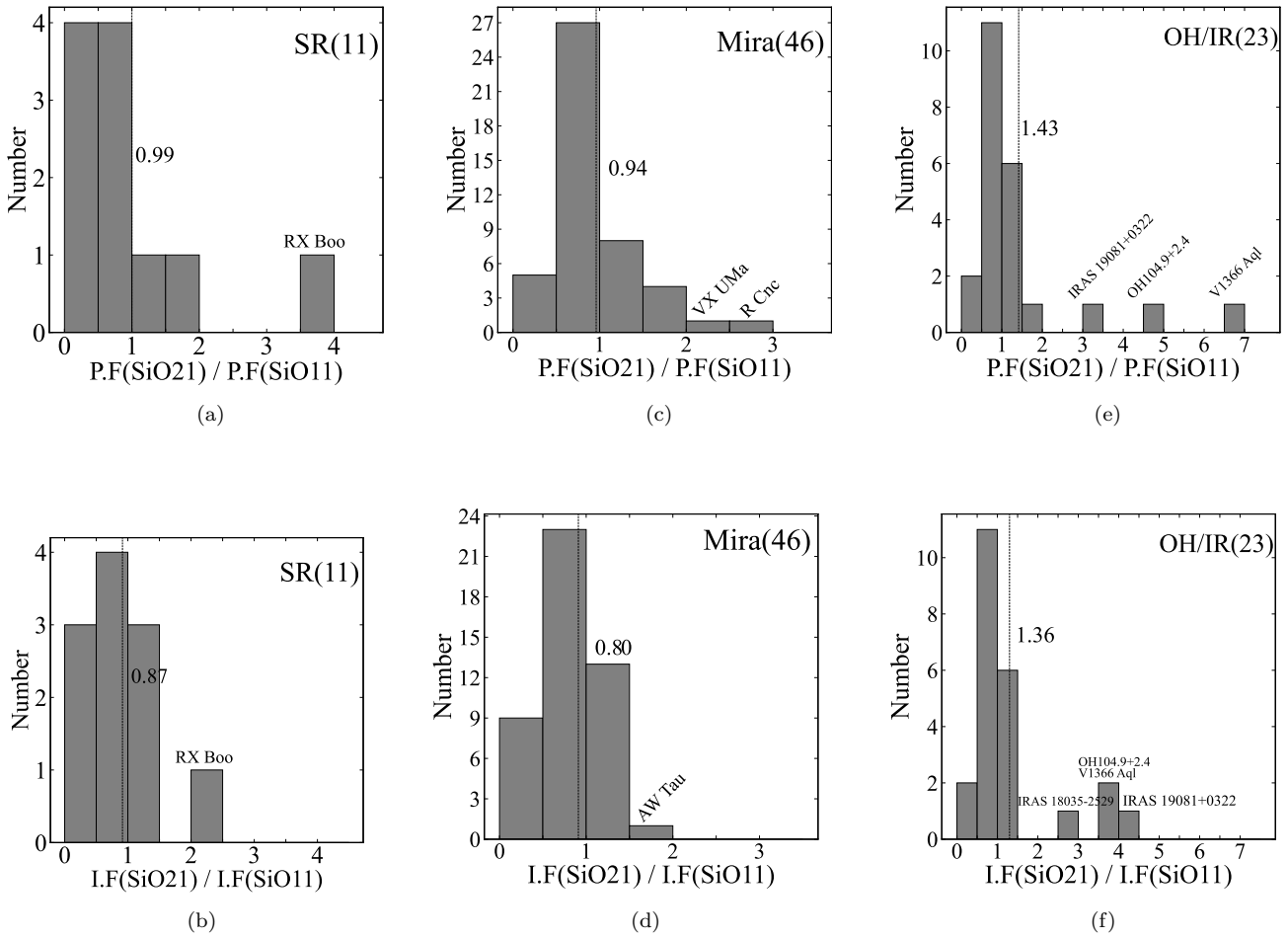

Figure 3. Distributions of the P.F and I.F ratios of SiO21 to SiO11. (a) P.F of SR, (b) I.F of SR, (c) P.F of Mira, (d) I.F of Mira, (e) P.F of OH/IR, and (f) I.F of OH/IR. The solid line represents the average value of the flux ratios.

regardless of the SiO13 detection in Miras and OH/IR stars are higher than those in Table 16 for the SiO11, SiO12, and SiO13 detected sources. The relation between the detections of the SiO31 and SiO13 masers is not clear yet. In Table 17, the average ratios of P.F(SiO21)/P.F(SiO11) and I.F(SiO21)/I.F(SiO11) in the Miras (1.08 and 0.93) show a smaller difference between the SiO11 and SiO21 maser intensities for sources with the SiO31 detections rather than for sources without the SiO31 detections (1.11, 0.90). This result is consistent with that of M. C. Stroh et al. (2018) and S.-H. Cho et al. (1996) showing the tight relation between SiO11 and SiO21 emission for sources with SiO31 masers. However, in the case of OH/IR stars with large SDs, these average values are opposite. On the other hand, except the large SD sources V1366 Aql and OH55.0+0.7, these values show the same tendency. For the SiO31 maser detected sources, the average values of the P.F(SiO21)/P.F(SiO11) and I.F(SiO21)/I.F(SiO11) in OH/IR stars are larger than those in Miras. This fact is consistent with the prior results of larger average values of the P.F(SiO21)/P.F(SiO11) and I.F(SiO21)/I.F(SiO11) in OH/IR stars due to the development of the hot dust shell according to the evolution from Miras to OH/IR stars.

The intensity ratios between the SiO11 and SiO12 masers are also compared for the SiO31 maser detected sources in Table 17. The average ratios of P.F(SiO12)/P.F(SiO11) and I.F(SiO12)/I.F(SiO11) in both the Miras and OH/IR stars for the SiO31 detected sources are less than 1, showing that the SiO11 masers are stronger than the SiO12 masers for the SiO31 detected sources. This result is also consistent with that of M. C. Stroh et al. (2018). The average ratios of P.F(SiO12)/P.F(SiO11) and I.F(SiO12)/I.F(SiO11) for the SiO31 undetected sources in the OH/IR stars are larger than 1, providing that the SiO12 masers are stronger than the SiO11 masers. These results may provide useful information for building the SiO31 maser model. It is difficult to investigate such meaningful trends in the case of the SRs, with only two sources.

4.2.2. Peak and Integrated Flux Ratios of the SiO12 Maser with Respect to the SiO11 Maser: P.F(SiO12)/P.F(SiO11) and I.F(SiO12)/I.F(SiO11)

The P.F and I.F ratios of P.F(SiO12)/P.F(SiO11) and I.F(SiO12)/I.F(SiO11) in the SRs are much larger than those of the Miras and OH/IR stars presented in Table 16. In the SRs, the SiO12 maser is detected in more stars than the SiO11 maser despite its higher excitation energy, as shown in Table 6. This may be due to a different pulsation mode of the SRs (i.e., SRs, overtone pulsation mode; Miras (OH/IR), fundamental mode), similar to what D.-J. Kim et al. (2018) suggested based on KVN VLBI observations for the SRb type, R Crt. Namely, it is because the overtone pulsation mode would induce a more turbulent environment across the CSE than the fundamental pulsation mode and produce different

Table 17
(a) Source List of SiO31 Detected Sources

No.	Source (Type)	P.F(SiO31)	I.F(SiO31)	$\frac{\text{P.F(SiO21)}}{\text{P.F(SiO11)}}$	$\frac{\text{I.F(SiO21)}}{\text{I.F(SiO11)}}$	Phase (ϕ)
1	Y Cas(Mira)	0.33	1.18	0.75	1.18	0.37
2	SY Scl(Mira)	12.38	1.87	1.02	1.16	0.71
3	WX Psc (OH/IR)	5.76	18.00	0.85	0.84	0.74
13	IK Tau(Mira)	9.84	23.78	0.98	0.80	0.14
22	NV Aur(Mira)	4.22	17.32	0.96	1.06	...
25	BW Cam(Mira)	0.29	0.58	1.15	0.88	...
28	BX Cam(Mira)	0.62	0.75	0.93	0.27	0.52
30	AW Tau(Mira)	0.25	1.00	2.00	1.89	...
32	U Lyn(Mira)	5.47	7.20	1.24	1.16	0.27
35	IRAS 07180-1314(OH/IR)	0.67	2.55	0.86	1.21	...
44	IW Hya(Mira)	2.00	5.44	0.75	0.82	...
45	R LMi(Mira)	0.25	0.37	1.21	0.97	0.75
46	R Leo(Mira)	5.11	11.99	1.35	0.74	0.76
48	R UMa(Mira)	0.89	0.78	0.57	0.54	0.03
62	W Hya(SR)	27.36	46.80	0.88	1.15	0.19
77	U Her(Mira)	15.98	30.53	0.71	0.70	0.12
82	IRAS 16486-3014(OH/IR)	0.56	3.11	0.72	1.09	...
83	V2108 Oph(SR)	12.53	36.86	0.84	0.90	...
89	VV Sgr(Mira)	1.25	1.49	1.58	0.71	...
92	V4120 Sgr(Mira)	0.25	0.37	0.83	0.65	...
94	IRAS 18035-2529(OH/IR)	0.72	1.15	1.71	2.60	...
95	V2302 Oph(Mira)	0.75	1.00	1.85	1.39	...
96	IRAS 18099+3127 (OH/IR)	0.43	0.58	0.91	0.93	...
102	V439 Sct (OH/IR)	0.72	1.01	0.97	1.11	...
106	V1366 Aql (OH/IR)	0.72	2.88	6.93	3.81	...
110	OH43.9+1.2 (OH/IR)	0.89	1.44	1.62	1.66	...
116	IRAS 19186+0315 (OH/IR)	0.58	1.87	1.11	1.06	...
118	OH49.8-0.8 (OH/IR)	0.33	0.44	1.04	0.95	...

Table 17
(Continued)

No.	Source (Type)	P.F(SiO31)	I.F(SiO31)	$\frac{P.F(SiO21)}{P.F(SiO11)}$	$\frac{I.F(SiO21)}{I.F(SiO11)}$	Phase (ϕ)
121	OH55.0+0.7 (OH/IR)	18.87	3.55	9.88	9.10	...
124	RT Aql(Mira)	5.04	9.22	1.07	1.07	0.07
126	IRAS 19422 +3506 (OH/IR)	3.24	3.24	1.13	0.75	...
129	RR Aql(Mira)	1.44	1.73	0.68	0.72	0.07
130	IRAS 19579 +3223 (OH/IR)	0.44	0.44	0.68	0.67	...
133	IRAS 20043 +2653 (OH/IR)	0.62	0.75	1.47	1.53	...
141	IRAS 20403 +3700 (OH/IR)	0.78	1.67	0.78	0.74	...
153	R Peg(Mira)	1.44	2.16	0.84	1.03	0.72

(b) Average and SD Value of Peak and Integrated Flux Ratios of SiO31 Detected and Undetected Sources

Type	Sample	SiO31 Detected												Sample	SiO31 Undetected							
		$\frac{P.F(SiO21)}{P.F(SiO11)}$		$\frac{I.F(SiO21)}{I.F(SiO11)}$		$\frac{P.F(SiO12)}{P.F(SiO11)}$		$\frac{I.F(SiO12)}{I.F(SiO11)}$		$\frac{P.F(SiO31)}{P.F(SiO11)}$		$\frac{I.F(SiO31)}{I.F(SiO11)}$			$\frac{P.F(SiO21)}{P.F(SiO11)}$		$\frac{I.F(SiO21)}{I.F(SiO11)}$		$\frac{P.F(SiO12)}{P.F(SiO11)}$		$\frac{I.F(SiO12)}{I.F(SiO11)}$	
		Ave.	SD	Ave.	SD	Ave.	SD	Ave.	SD	Ave.	SD	Ave.	SD		Ave.	SD	Ave.	SD	Ave.	SD	Ave.	SD
SR	2	0.86	0.02	1.02	0.12	1.15	0.42	0.78	0.17	0.05	0.03	0.03	0.02	19	1.34	1.45	1.15	1.29	2.23	1.82	3.52	3.00
Mira	19	1.08	0.38	0.93	0.34	0.67	0.36	0.71	0.37	0.07	0.10	0.03	0.03	35	1.11	1.21	0.90	0.69	1.26	0.67	1.20	0.65
OH/IR	15	2.04	2.57	1.87	2.09	0.82	0.66	0.63	0.29	0.19	0.21	0.14	0.21	25	1.57	1.34	1.54	1.29	1.08	0.70	1.04	0.67

Note. The phase was determined using the Lomb–Scargle periodogram and data from AAVSO. The phase of WX Psc was calculated approximately from L. Bertre (1993) J. Pardo et al. (2004), and Y. Yun et al. (2016).

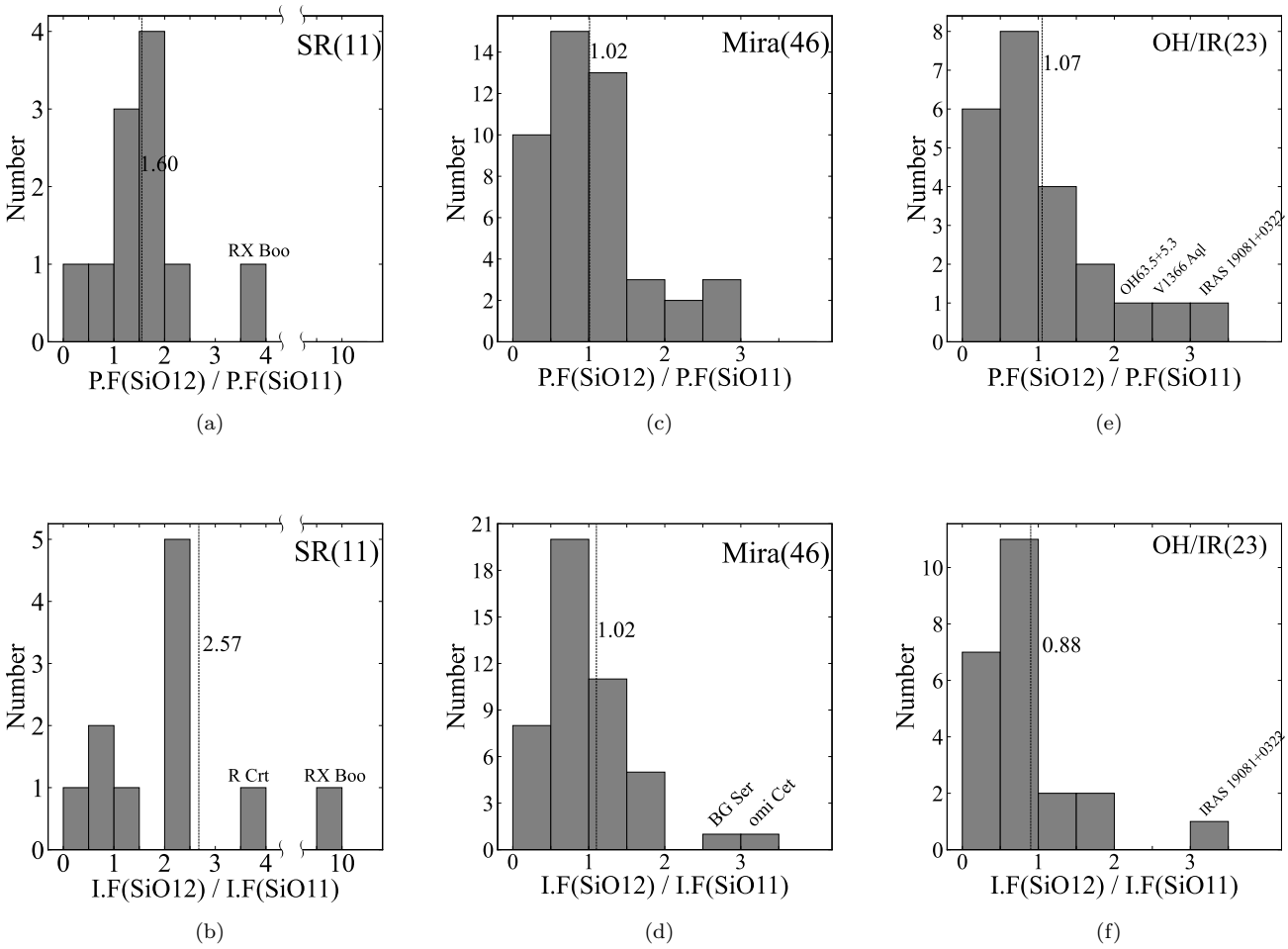

Figure 4. Distributions of the P.F and I.F ratios of SiO12 to SiO11. (a) P.F of SR, (b) I.F of SR, (c) P.F of Mira, (d) I.F of Mira, (e) P.F of OH/IR, and (f) I.F of OH/IR. The solid line represents the average value of the flux ratios.

physical conditions for maser emissions in SRs, as described in the previous section, for R Crt. Additionally, these ratios tend to decrease according to the more evolved types from Miras to OH/IR stars. As SRs evolve into Miras, the pulsation mode changes from the overtone mode to the fundamental mode and gradually becomes stable (P. Wood et al. 1999; M. Trabucchi et al. 2017). Figure 4 shows the distribution of the P.F(SiO12)/P.F(SiO11) and I.F(SiO12)/I.F(SiO11) ratios as histograms. The distribution for SRs is observed to be somewhat broader, with RX Boo standing out again due to its high ratios. The majority of stars in the Miras are distributed between 0.5 and 1, whereas in OH/IR stars, they are distributed between 0 and 0.5.

4.2.3. P.F(SiO13)/P.F(SiO11) and I.F(SiO13)/I.F(SiO11) Ratios

Figure 5 and Table 16 show there is no significant noticeable difference according to the SRs, Miras, and OH/IR stars. In Figure 5, the histograms illustrate that more than half of the distributions for all three pulsation-type stars are concentrated between 0 and 0.5. This suggests that the SiO13 maser does not show many different properties across the three pulsation types: SRs, Miras, and OH/IR stars.

4.3. Investigation of the Kinematics

Wind kinematics associated with the accelerating outflow from the atmosphere of the SiO maser region to the dust layer, the 22 GHz H_2O maser region, and the thermal SiO envelope, including other thermal lines of the HCN, SiS, and CO envelopes, were investigated by measuring their expansion velocities for the 11 HCN detected sources (WX Psc (#3), IK Tau (#13), TX Cam (#21), NV Aur(#22), BX Cam (#28), R Leo (#46), W Hya (#62), RX Boo (#65), V4120 Sgr (#92), V1111 Oph (#99), and R Cas (#155)). The expansion velocities were determined by measuring half of the full width at zero power (FWZP) of the H_2O maser and the SiO, HCN, and SiS thermal lines. In the case of the SiO masers, the maximum line-of-sight velocity with respect to the star (half of the FWZP of the SiO maser line) includes both the expansion and infall of gas (I. Gonidakis et al. 2013). The SiO maser regions (located at 2–4 R_*; P. Diamond et al. 1994; D. A. Boboltz & M. Wittkowski 2005) are situated between the radio photosphere and the dust layer within the wind launch region. Stellar pulsations and the resulting shocks directly influence these regions. The SiO masers show an expansion with a radial proper motion of 5–10 km s^{-1} as a dominant mode (P. J. Diamond & A. Kemball 2003) although both the expansion and infall motions of gas coexisted (I. Gonidakis et al. 2013). We assume that half of the FWZPs of the SiO masers represent the expansion velocity as an upper limit. This region will be important as a transmission channel of the pulsating motion that derives a dust formation and mass loss (I. McDonald & A. Zijlstra 2016). The representative

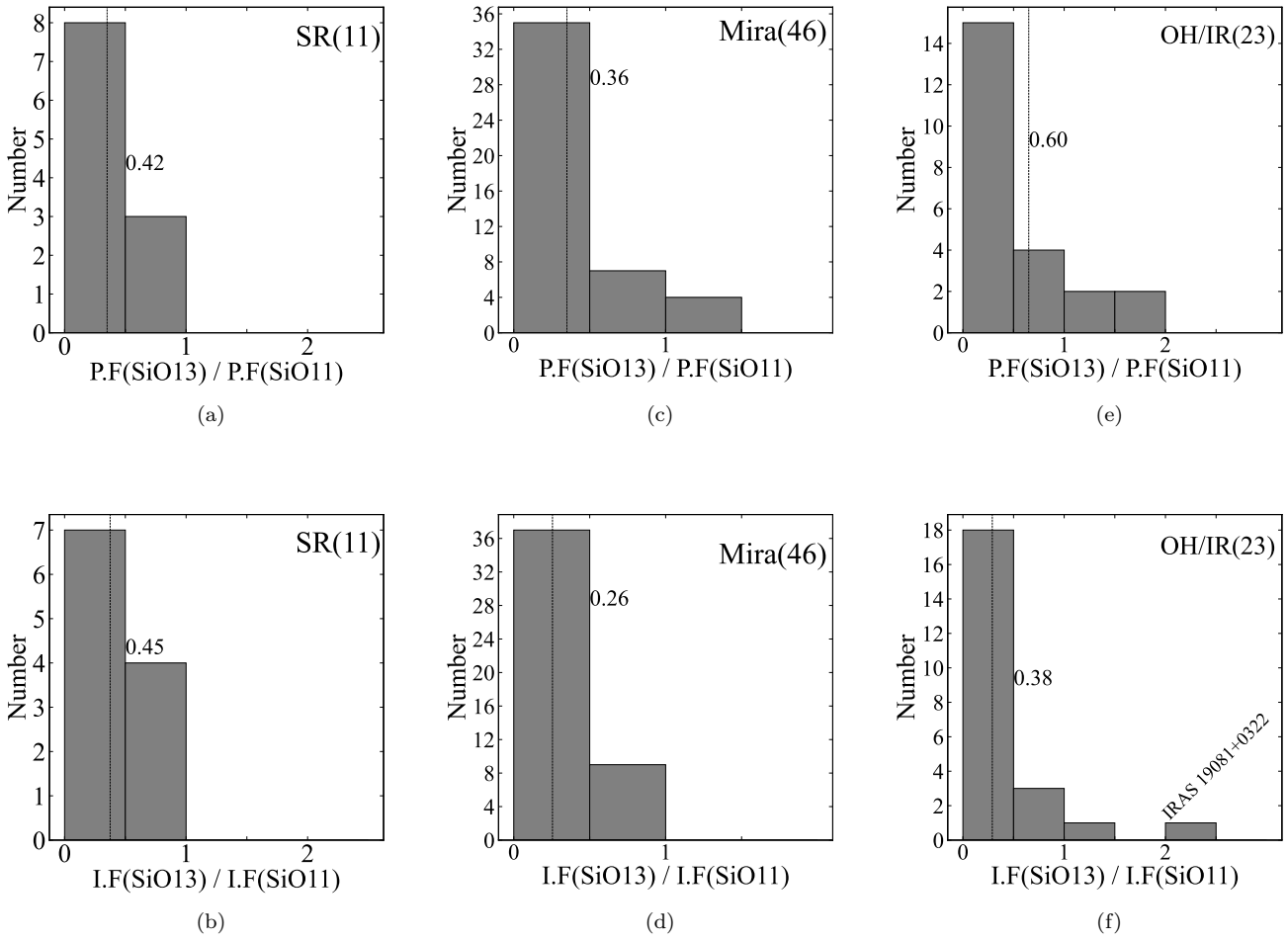

Figure 5. Distributions of the P.F and I.F ratios of SiO13 to SiO11. (a) P.F of SR, (b) I.F of SR, (c) P.F of Mira, (d) I.F of Mira, (e) P.F of OH/IR, and (f) I.F of OH/IR. The solid line represents the average value of the flux ratios.

expansion velocities of the SiO masers are adopted by the average values of the SiO11 SiO12 and SiO13 masers (Table 18). The H_2O maser traces 5–50 R_*, including dust layers, and the proper motions of the H_2O maser show overall an accelerating expansion (A. Richards et al. 2012). It is clumpy, and the momentum from the radiation pressure on the dust is transferred more efficiently in denser clumps, which may cause directed (one-sided or bipolar) and asymmetric outflows. The expansion velocities using the detected H_2O maser lines were estimated as follows. (1) We estimated the expansion velocities with half of the double-peaked H_2O maser lines with respect to the stellar velocities: IK Tau (#13) and W Hya (#62). (2) The one-sided H_2O maser velocities were adopted with respect to the stellar velocity (red or blue; WX Psc (#3), NV Aur (#22), and BX Cam (#28)). (3) Half of the FWZP velocities for the H_2O maser line with a significant intensity (>1.17 Jy) around the stellar velocity were adopted: RX Boo (#65) and V1111 Oph (#99). The H_2O maser sources with a weak intensity (<1.17 Jy: R Leo (#46), V4210 Sgr (#92), and R Cas (#155)) were excluded from the H_2O plot in Figure 6 because they cannot represent the expansion velocity of the H_2O maser region. The SiO thermal lines can provide information on the region where the mass loss is initiated and where dust is generated (M. J. Reid & K. M. Menten 1997; F. L. Schöier et al. 2006). According to S. Ramstedt et al. (2009), the expansion velocity of SiO gas is $\sim$ 20% less than that of CO gas. In our case, the average velocities of the SiO thermal lines are adopted by those of the SiO01, SiO02, and SiO03 lines, respectively. These SiO expansion velocities are only about 1% lower than those of CO, indicating a nearly similar value. HCN is formed in the inner envelope due to nonequilibrium shock chemistry (D. Duari et al. 1999), and its distribution radius is determined by photodissociation (K. B. Marvel 2005). The HCN line formation region traced by the observed molecular lines was 50–500 R_*, while that of ^{28}SiO was 70–10,000 R_* (L. Decin et al. 2010). S. Wallström et al. (2024) measured the angular extents of HCN to be 22–590 R_* and that of SiO to be 140–1100 R_*. The HCN is distributed further inward than SiO. In Figure 7, we adopted the median value of HCN (120 R_*) by S. Wallström et al. (2024). The expansion velocities of HCN estimated by half of the FWZPs are larger than those measured by the v_{CO} (Table 18). It is likely due to the three components of hyperfine splitting of the rotational levels in the HCN molecule. In evolved stars, this structure merges and broadens the FWZPs of HCN, which could result in higher estimated expansion velocities than those of CO. The outermost expansion velocities (terminal wind velocity) in Table 18 are obtained from existing CO data in the literature. In Figure 7, we plotted the expansion velocities estimated from three SiO maser lines, H_2O maser, HCN (SiS), three SiO thermal lines, and CO lines in Table 18 according to radial distances of the dominant line formation region of the molecular lines from the central star. The dust condensation radius was adopted as

Table 18
Half of FWZP and CO Expansion Velocity for HCN Detected Sources

Source	$v_{\mathrm{SiO\text{-}m}}$			$v_{\mathrm{H_2O}}$	$v_{\mathrm{SiO\text{-}t}}$			v_{SiS}	v_{HCN}	v_{CO}
	SiO11	SiO12	SiO13		SiO01	SiO02	SiO03			
WX Psc	8.30	7.75	7.83	17.50	18.51	20.33	20.31	20.99	22.06	23.1 (d)
IK Tau	7.39	7.29	5.93	14.77	21.06	21.61	21.88	18.97	21.97	18.5 (a)
TX Cam	10.76	9.26	9.49	⋯	19.66	21.74	21.51	20.93	24.52	21.2 (a)
NV Aur	6.36	4.39	3.01	3.24	18.04	18.16	19.55	⋯	20.59	19.2 (a)
BX Cam	6.40	6.89	5.92	11.69	21.71	18.65	19.24	⋯	18.79	19.0 (b)
R Leo	7.06	5.82	8.70	3.85	5.94	6.98	7.99	⋯	6.48	8.5 (b)
W Hya	5.31	8.25	5.34	5.18	7.87	7.08	7.56	⋯	13.75	8.5 (a)
RX Boo	13.98	13.55	8.15	4.35	9.61	11.67	9.52	⋯	12.01	10 (b)
V4120 Sgr	6.86	10.55	9.87	1.72	14.24	15.78	19.55	⋯	24.36	15.6 (c)
V1111 Oph	7.25	6.80	3.60	13.64	18.70	20.76	19.06	⋯	24.85	17.0 (b)
R Cas	7.81	7.48	9.00	2.94	9.86	14.87	15.07	⋯	13.25	13.5 (a)

Notes. $v_{\mathrm{H_2O}}$: expansion velocity (exp. vel.) by H_2O. $v_{\mathrm{SiO\text{-}m}}$: exp. vel. by SiO maser. $v_{\mathrm{SiO\text{-}t}}$: exp. vel. by SiO thermal. v_{SiS}: exp. vel. by SiS. v_{HCN}: exp. vel. by HCN. v_{CO}: exp. vel. by CO.
References. (a) E. De Beck et al. (2010), (b) T. Danilovich et al. (2015), (c) E. Josselin et al. (1998), (d) C. A. Gottlieb et al. (2022).

$R_{\mathrm{dust}} \sim 6\ R_*$ (C. A. Gottlieb et al. 2022). We confirmed the acceleration of the expansion velocities after the dust layers for each object. In particular, the expansion velocities measured by HCN are significantly larger than those measured by other molecules. The shape of the overall velocity curve is similar to a slow wind acceleration pattern (L. Decin et al. 2010, 2018), although the data points are limited. The terminal expansion velocities (v_{CO}) of two SRs, W Hya and RX Boo, and R Leo (Mira) are small compared to those of other Miras and OH/IR star WX Psc showing a small mass loss rate. These three stars also show that the expansion velocities measured by the H_2O maser are small compared to those by the SiO masers. It is not yet certain if the wind acceleration pattern is different for the pulsation types (C. A. Gottlieb et al. 2022). The ALMA ATOMIUM data present a slow wind acceleration and show that the radial velocity described by the momentum equation cannot explain the complexity of the velocity field in the innermost region (C. A. Gottlieb et al. 2022). C. A. Gottlieb et al. (2022) proposed a binary interaction with a (sub)stellar companion for this explanation.

4.4. Variations of Maser Properties According to Evolutionary Phases in IRAS Two-color Diagram

Figures 8, 9, and 10 present the IRAS two-color diagrams and the corresponding observational results for the SiO and H_2O masers from the 155 observed sources, which include 50 SRs, 55 Miras, and 50 OH/IR stars. The SRs, denoted by triangles, span Regions I, II, and IIIa except GP Tau (#26) and RW Lep (#27) in VII, while Miras, represented by circles, are confined to Region II and IIIa except R Leo (#46) in I, TX Cam (#21), VX UMa (#49), T Oph (#79), and V1111 Oph (#99) in VII. These sources are marked in Figure 8. On the other hand, OH/IRs, indicated by squares, are identified as being distributed in Regions IIIa and IIIb. Notably, all these objects are found to be well aligned with the evolutionary trajectory from O-rich Miras to OH/IRs (P. Bedijn 1987; W. van der Veen & H. Habing 1988).

Almost all H_2O and SiO maser detected sources from SRs, Miras, and OH/IR stars are found in Regions II and IIIa. H_2O-only detected sources appearing only in the SRs are found mainly in Regions II and IIIa, while the SiO-only detected sources are found mainly in the OH/IR stars of Region IIIb. The main factors of the evolutionary sequence in these different regions are the variability due to pulsation, without or with O-rich circumstellar shells, and the mass loss rate (W. van der Veen & H. Habing 1988). These results about dominant SiO-only detected sources in Region IIIb match the results of J. Kim et al. (2010) and C.-Y. Cho et al. (2017). The characteristic type of object in Region I is O-rich nonvariable stars without circumstellar shells (P. Bedijn 1987; W. van der Veen & H. Habing 1988). Thus, we can find that five SRs with no maser detections are distributed in Region I. However, one SR (W Hya (#62)) and one Mira (R Leo (#45)) with both H_2O and SiO maser detected sources are distributed on the right side of Region I. Almost all H_2O and SiO maser detected sources of SRs, Miras, and OH/IR stars are distributed in Regions II and IIIa. These variable stars with O-rich circumstellar shells show mass loss rates ranging from $10^{-7}\ M_\odot\ \mathrm{yr}^{-1}$ at the lower end to more than $10^{-4}\ M_\odot\ \mathrm{yr}^{-1}$ at the upper end (P. Bedijn 1987; M. Rowan-Robinson et al. 1986). In addition, H_2O-only detected sources that appeared only in the SRs are distributed in Regions II and IIIa. On the other hand, sources with SiO-only detections are predominantly found in OH/IR stars. They are distributed in Region IIIb, with variable stars and thick O-rich circumstellar shells. These different results between the H_2O and SiO masers seem to be due to their different pumping mechanisms associated with a physical environment according to the evolutionary stage. The H_2O maser is emitted at a relatively low temperature and low density (300–1000 K, $10^7 \sim 10^9\ \mathrm{cm}^{-3}$) by a collisional pumping mechanism, while the SiO maser is emitted at a high temperature and high density ($\sim$1770 K and $>10^9\ \mathrm{cm}^{-3}$) by both radiative and collisional pumping mechanisms (P. Lockett & M. Elitzur 1992; E. Humphreys et al. 2002; V. Bujarrabal 1994). Therefore, the lower density and temperature of the circumstellar shells in SRs may be why SRs do not emit SiO masers compared to Miras, as the shells are less developed due to relatively weaker pulsations than those of the Miras. In relation to the dominant SiO-only detected sources of the OH/IR stars in Region IIIb, we can also refer to the explanations provided by J. Kim et al. (2010) and C.-Y. Cho et al. (2017). In other words, two possibilities may be presented: an easy thermalization of the H_2O maser by collision due to the high mass loss rate of OH/IR stars and the increase in optical depth of the CSE leading to an insufficient

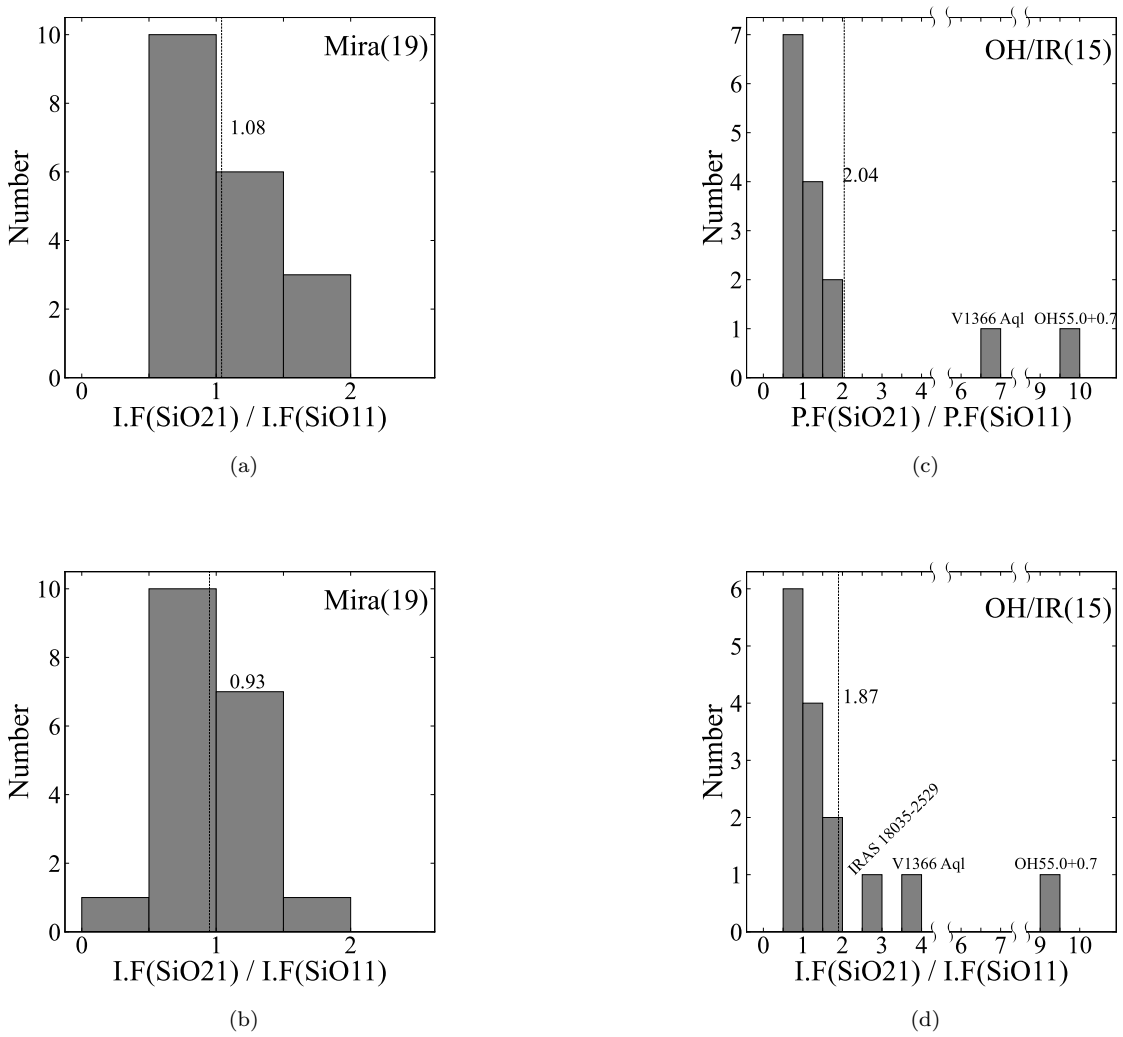

Figure 6. Distributions of the peak and integrated flux (P.F and I.F) ratios of SiO21 to SiO11 for SiO31 detected sources. (a) P.F of Mira, (b) I.F of Mira, (c) P.F of OH/IR, and (d) I.F of OH/IR. The solid line represents the average value of the flux ratios.

excitation temperature for the H_2O maser emission (Y. Gómez et al. 1990). As the evolution progresses further, in the post-AGB stage (Regions IV, V, and VIII), D.-H. Yoon et al. (2014) showed that SiO-only detected sources, including some with both SiO and H_2O detected sources, are distributed in the LI region while the H_2O-only detected sources distributed in the RI region may be due to the different mass and expansion velocities of the stars associated with their different evolutionary stages.

The sources detected in the SiO22 rare maser are distributed in Regions II (IU Tau (#)17), VII (TX Cam (#21), V1111 Oph (#99)), and IIIb (NV Aur (#22)). As mentioned in Section III, they are SiO-only or weak H_2O maser detected sources associated with the infrared line overlap between ^{28}SiO and H_2O molecules (H. Olofsson et al. 1981, 1985). TX Cam and V1111 Oph are located in Region VII, where variable stars mainly show evolved C-rich circumstellar shells (W. van der Veen & H. Habing 1988). Thus, these sources may be objects on their way to an S-type star. In addition, a carbon-bearing molecule HCN was detected from the O-rich stars TX Cam, V1111 Oph, and NV Aur. The characteristics of the maser properties from S-type stars will be presented again based on the KVN survey for S-type stars (S-M. Son et al. 2025, in preparation). In the IRAS two-color diagram of Figure 9, we investigated the distribution of the SiO21 sources, which exhibit stronger intensities than those of the SiO11 sources for all SiO11 and SiO21 maser detected sources according to SRs, Miras, and OH/IR stars. The number of stronger SiO21 sources increases from the evolutionary track (from Regions II to IIIb) according to the SRs, Miras, and OH/IR stars. They exhibit 25.0% (8/32) in the SRs, 32.7% (18/55) except 1 SiO $v = 2$-only source in the Miras (V Leo (#47)), and 52.0% (26/50) except 1 SiO $v = 2$-only source in the OH/IR stars (OH43.8+0.5 (#112)), respectively. As mentioned in Section 4.2, these results about the relatively strong emission of the SiO21 maser again seem to support that they may be due to the development of a hot dust shell and their different excitation temperatures associated with the physical environments according to their evolutionary stages. These results are also consistent with the fact that the SiO $v = 2$-only sources appear more frequently in the later evolutionary stages of the OH/IR stars (C.-Y. Cho et al. 2017). In Figure 10, the SiO12 and SiO13 maser detected sources among all SiO maser detected sources are plotted in the IRAS two-color diagram. Sources with both SiO12 and SiO13 detections appear most frequently in the Miras, with an 83.6% detection rate, followed by 26.0% in the SRs and 46.0% in the OH/IR stars (Table 6). These sources are distributed across Regions I to IIIb. The

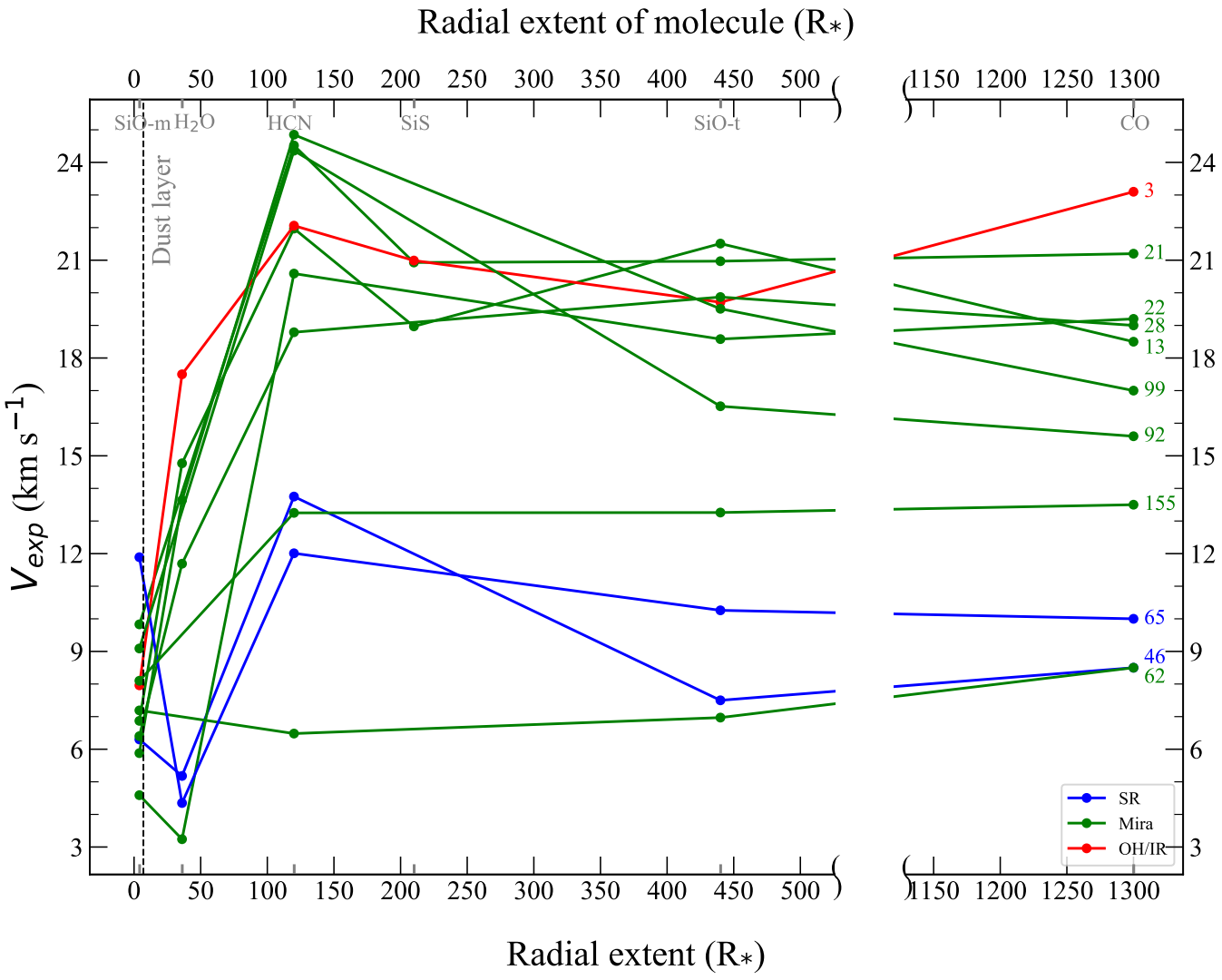

Figure 7. Measured expansion velocities of simultaneously observed molecular lines according to radial distances from the central star for 11 HCN detected sources. The distances of the dominant line formation region in units of stellar radius from the central star are as follows. SiO maser adopted 3 R_* as the median value between 2 and 4 R_* (P. Diamond et al. 1994; D. A. Boboltz & M. Wittkowski 2005), H_2O maser adopted 36 R_* (A. Richards et al. 2012) and 120 R_* for HCN, 210 R_* for the SiS, 440 R_* for the SiO thermal lines, and 1300 R_* for CO based on the median values measured by S. Wallström et al. (2024). These values are indicated at the top of the graph. The vertical dashed line indicates dust condensation radius, R_{dust} at ∼6 R_* derived by C. A. Gottlieb et al. (2022).

SiO13 maser like SiO11 and SiO12 masers show higher detection rates in the OH/IR stars than in the SRs. However, the the SiO01, SiO02, and SiO03 lines show opposite results in these two types shown in Table 6. This result may be due to differences in the physical environment according to the difference in the two line formation regions. The SiO maser comes from the atmospheric region (2–4 R_*) inside the dust layer, and the thermal line comes from above the dust layer (140–1100 R_*; S. Wallström et al. 2024). Thus, the SiO abundance in the SiO thermal line formation region of the highly extended and more evolved OH/IR stars with thick dust envelopes may be lower than the SiO abundance in the SRs due to a lot of dust formation like silicate dust grains (T. Jones & K. Merrill 1976). Therefore, the SiO01, SiO02, and SiO03 lines show lower detection rates in OH/IR stars than in SRs unlike SiO11, SiO12, and SiO13 masers.

5. Summary

1. We report the observational results of the Simultaneous Multi-mAser Survey Toward Evolved Stars (SMASTES) I, which was performed toward 155 M-type O-rich AGB stars (50 SRs, 55 Miras, and 50 OH/IR stars) from 2023 February to 2023 October. The upgraded four-band (22/43/86/129GHz) wide receiving system of the KVN was used for simultaneous observations of nineteen molecular lines: H_2O 6_{16}–5_{23}, ^{28}SiO $v = 0, 1, 2, 3$, $J = 1$–0; $v = 0, 1, 2$, $J = 2$–1; $v = 0, 1, 2$, $J = 3$–2; ^{29}SiO $v = 0$, $J = 1$–0, 2–1; ^{30}SiO $v = 0$, $J = 1$–0; CS $v = 0$, $J = 1$–0, HCN $v = 0$, $J = 1$–0, SiS $v = 0$, $J = 5$–4, SO $v = 0$, $N_J = 2_2$–1_1, and SO_2 $v = 0$, $J_{Ka,Kc} = 24_{4,20}$–$23_{5,19}$.

2. As the overall observational results of the H_2O and SiO masers, both the H_2O and SiO masers were detected from 21 stars among 50 SRs (42%), 50 stars among 55 Miras (91%), and 26 stars among 50 OH/IRs (52%), respectively. The H_2O maser was detected from 26 stars among 50 SRs (52%), 50 stars among 55 Miras (91%), and 26 stars among 50 OH/IR stars (52%). The H_2O-only maser without SiO maser detections was detected from 5 stars among 50 SRs (10%), but unlike the SiO-only maser, none from the 55 Miras and 50 OH/IR stars. The SiO11 maser was detected from 24 stars

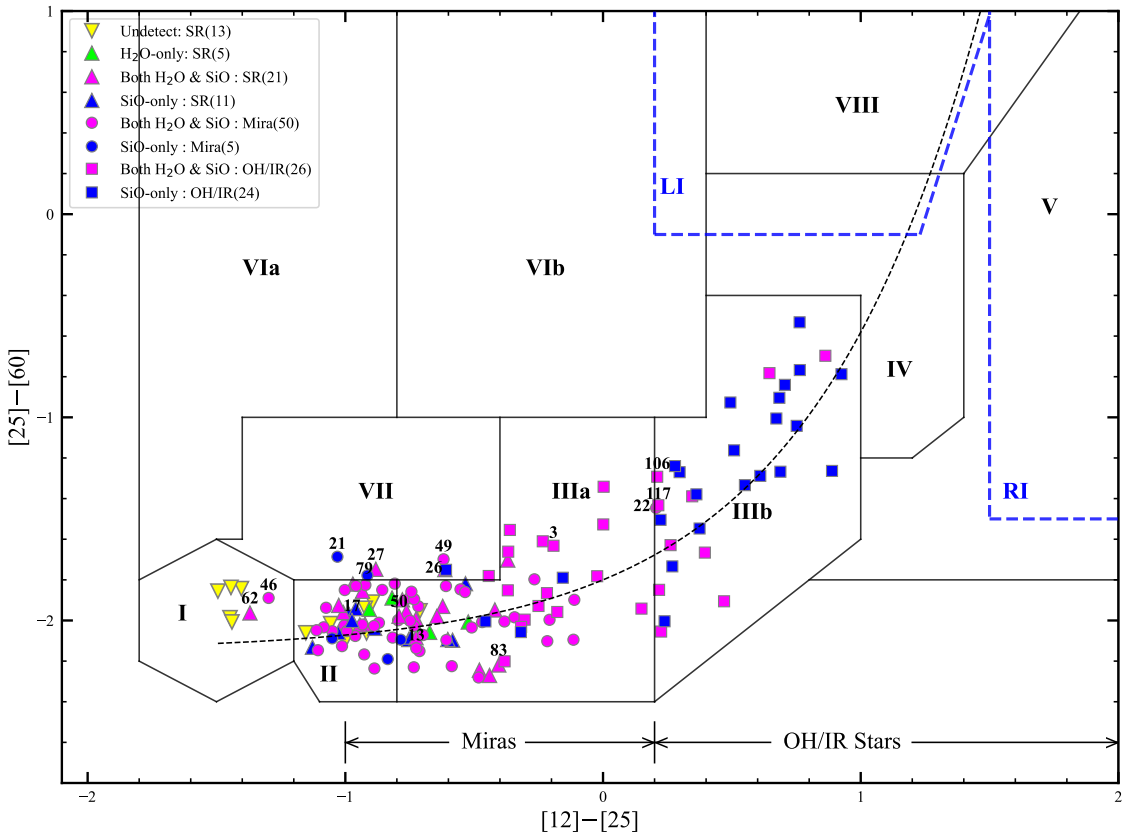

Figure 8. IRAS two-color diagram of observational results for the H_2O and SiO masers according to SRs, Miras, and OH/IR stars. The curved dashed line is the evolutionary track defined by W. van der Veen & H. Habing (1988). The blue dashed line indicates the two groups of post-AGB stars, LI (left of IRAS, blue group) and RI (Right of IRAS, red group; M. N. Sevenster 2002). Undetected sources are marked with the yellow inverted filled triangles, the green filled triangles represent sources with H_2O maser only detected sources, the blue triangles, circles, and squares indicate sources with SiO maser only detected sources, and the pink triangles, circles, and squares indicate sources with both H_2O and SiO maser detected sources. Triangles represent SRs, squares represent Miras, and circles represent OH/IR stars. The numbers indicate identification numbers in Table 1. The numbers indicated on the graph correspond to sources where SiO22 has been detected (#17, #21, #22, and #99), three famous sources for each type of SRs, Miras, and OH/IR stars (in total, nine stars) mentioned in Section 3 (#3, #13, #22, #50, #62, #83, #99, #106, and #117) and mentioned in Section 4.4 (#21, #26, #27, #46, #49, #79 and #99).

among the 50 SRs (48%), 54 stars among the 55 Miras (98%), and 48 stars among the 50 OH/IRs (96%) while the SiO12 maser was detected from 32 stars among the 50 SRs (64%), 54 stars among the 55 Miras (98%), and 41 stars among the 50 OH/IRs (82%).

3. The detection rates of the SiO02, SiO12, and ^{29}SiO02 masers in SRs were higher than those of the SiO01, SiO11, and ^{29}SiO01 masers, despite requiring a higher excitation energy compared to that of the SiO11 maser. The SiO12 maser was also detected in more stars than the SiO11 maser in the SRs. In addition, the average values of the P.F(SiO12)/P.F(SiO11) and I.F(SiO12)/I.F(SiO11) in the SRs are much larger than those of the Miras and OH/IR stars. This result may be due to a different pulsation mode of the SRs (i.e., SRs: overtone pulsation mode, whereas Miras and OH/IR): fundamental mode).

4. The SiO22 rare maser, which is known to be more frequently detected in S-type stars compared to M-type stars, was detected in 1 SR (IU Tau (#17)) and 3 Miras (TX Cam (#21), NV Aur (#22), and V1111 Oph (#99)) including three new detections (IU Tau, NV Aur, and V1111 Oph).

5. The SiO13 maser, like the SiO11 and SiO12 masers, shows higher detection rates in the OH/IR stars than in the SRs. However, the SiO01 SiO02, and SiO03 lines show opposite results in these two types. This result may be due to the differences in the physical conditions according to the difference in the line formation regions of these lines. The SiO maser comes from the atmospheric region (2–4 R_*) inside the dust layer; while the SiO thermal line comes from above the dust layer (140–1100 R_*; S. Wallström et al. 2024). Therefore, in highly extended and more evolved OH/IR stars with thick dust envelopes, the SiO abundance in the regions where SiO thermal lines form may be lower compared to that in SRs. This reduction is likely due to extensive dust formation, such as silicate dust grains.

6. Higher-J rotational transitions in the SiO01, SiO02, and SiO03 thermal lines were detected more frequently than lower-J ones, especially in the SRs and Miras. The HCN and SiS lines were detected from 11 and 3 stars among all observed O-rich stars.

7. The average values of the ratios P.F(H_2O)/P.F(SiO11) and I.F(H_2O)/I.F(SiO11) for SRs are significantly larger than those for the Miras and OH/IR stars although the SD is large. In the case of the Miras and OH/IR stars, these values are not much different; however, the value of the OH/IR star is slightly larger. These results may be interpreted in the context of the evolutionary sequence from SRs to Miras and OH/IR stars. As SRs evolve toward Miras, the latter exhibit larger pulsation amplitudes and stronger fundamental mode photospheric shocks, whereas SRs display weaker overtone-mode shocks. These stronger shocks in Miras can enhance SiO maser emission by driving more material outward and increasing the

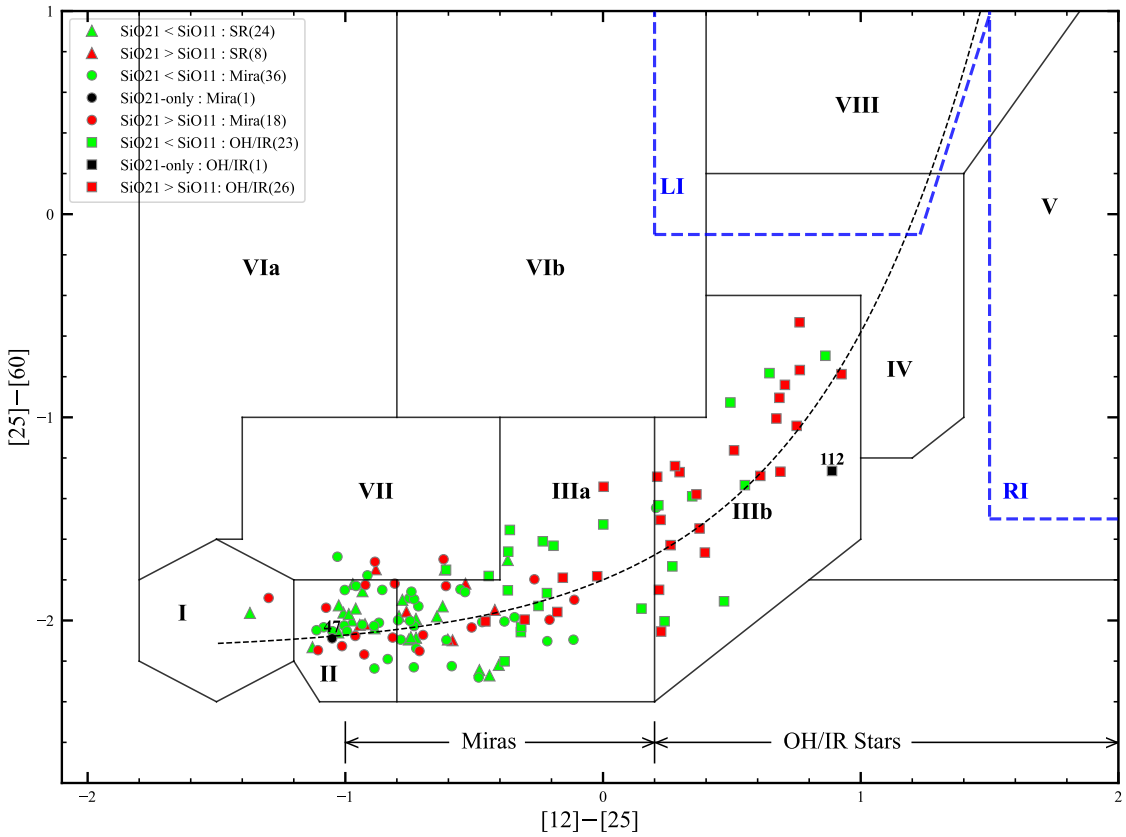

Figure 9. IRAS two-color diagram of observational results for the P.F values of SiO21 and SiO11 masers according to the SRs, Miras, and OH/IR stars. Sources with a higher P.F value for SiO11 than SiO21 are marked in green, while those with a higher P.F value for SiO21 are marked in red. SiO21-only sources are identified in black with numbers (V Leo (#47) and OH43.8+0.5 (#112)). The curved and blue dashed lines represent the same as in Figure 8.

local gas density, including that of SiO. In contrast, the extended atmospheres and envelopes of OH/IR stars may not provide the high-density and high-temperature conditions required for efficient SiO maser emission, which are higher than those needed for H_2O masers.

8. The P.F and I.F ratios of P.F(SiO21)/P.F(SiO11) and I.F (SiO21)/I.F(SiO11) in the OH/IR stars are much larger than those in the Miras and SRs. The SiO21 maser requires a much higher excitation temperature than the $v = 1$. So the relatively strong excitation of the SiO21 maser would be due to the development of the hot dust shell close to the star according to the evolution from Miras to OH/IR stars (S. Ramstedt et al. 2012; S.-H. Cho & J. Kim 2012; D.-H. Yoon et al. 2014). These facts match with the results that the number of stronger SiO21 sources increases from the evolutionary track (from Regions II to IIIb) according to the SRs, Miras, and OH/IR stars in IRAS two-color diagram.

9. In Table 17, the peak and integrated flux ratios of the P.F (SiO21)/P.F(SiO11) and I.F(SiO21)/I.F(SiO11) for the SiO31 maser detected sources are higher than the average values of those flux ratios in Miras and OH/IR stars for the SiO31 maser undetected sources except the P.F(SiO21)/P.F(SiO11) in Miras with large SD and also than those in Table 15. For the SiO31 maser detected sources, the average values of the P.F (SiO21)/P.F(SiO11), I.F(SiO21)/I.F(SiO11) in OH/IR stars are larger than those in Miras. This fact is consistent with the results of larger average values of the P.F(SiO21)/P.F(SiO11) and I.F(SiO21)/I.F(SiO11) in OH/IR stars due to the development of the hot dust shell according to the evolution from Miras to OH/IR stars.

10. Wind kinematics related to the accelerating outflow from the SiO maser region in the atmosphere to the dust layer, the 22 GHz H_2O maser region, and the thermal envelopes of SiO, HCN, SiS, and CO were investigated by measuring expansion velocities in 11 sources where HCN was detected. The acceleration of expansion velocities beyond the dust layer was confirmed for each object. The overall shape of the velocity curve resembles a slow wind acceleration pattern. The terminal expansion velocities of the two SRs, W Hya and RX Boo, as well as the Mira-type star R Leo are lower than those of the other Mira and the OH/IR star WX Psc, and these three stars show low mass loss rates. Additionally, these three stars have lower expansion velocities as measured by the H_2O maser than those as measured by the SiO maser.

11. Almost all H_2O and SiO maser sources detected from SRs, Miras, and OH/IR stars are located in Regions II, IIIa, and IIIb of the IRAS two-color diagram. The H_2O-only detected sources found mainly in SRs are primarily located in Regions II and IIIa. In contrast, SiO-only maser detected sources found mainly in OH/IR stars are concentrated in Region IIIb, which is consistent with previous KVN findings. These different distributions of H_2O and SiO masers likely reflect different pumping mechanisms that depend on the physical environment at different stages of evolution from SRs to Miras and OH/IR stars. Main physical environmental factors at these evolutionary stages could include the presence or absence of O-rich circumstellar shells (thin or thick), pulsation modes, and mass loss rates. Consequently, the weaker SiO maser emission in SRs compared to Miras may be attributed to the lower density and temperature of the

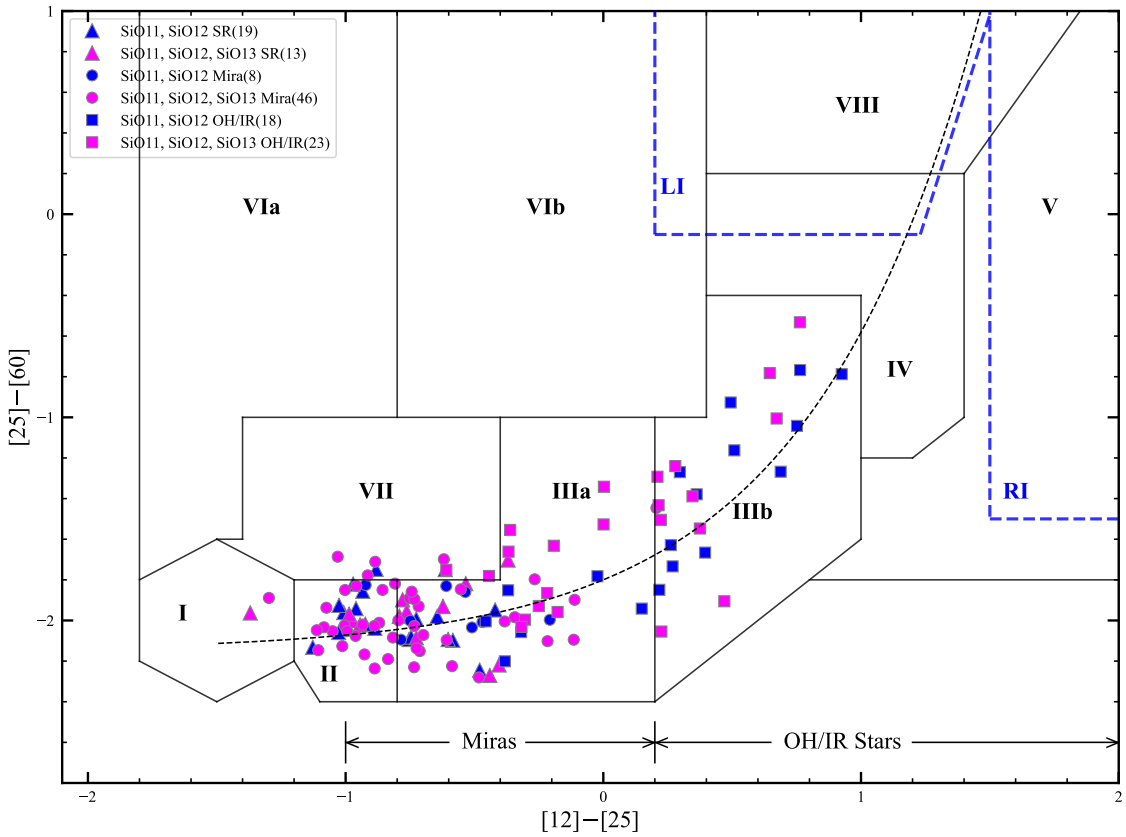

Figure 10. IRAS two-color diagram of observational results for the SiO12 and SiO13 masers according to the SRs, Miras, and OH/IR stars. The curved and blue dashed lines represent the same as in Figure 8. The sources where SiO11 and SiO12 are detected are shown in blue, while those where SiO11, SiO12, and SiO13 are all detected are shown in pink.

circumstellar shells which are less developed due to relatively weaker stellar pulsations in SRs.

This work was supported by a National Research Foundation of Korea (NRF) grant funded by the Korean government (MSIT; S.-H.C.; No. RS-2022-NR069862, D.-H.Y.; NRF2019 R1A6A3A01091901, K.-W.S.: 2022R1I1A3055131) and by the Major Project Research Fund (J.K.: No. 2022-1-840-05 and 2023-1-840-00) of the Korea Astronomy and Space Science Institute (KASI). We are grateful to all the staff members at the KVN who helped operate the array and the single-dish telescope and correlate the data. The KVN is a facility operated by KASI, which is under the protection of the National Research Council of Science and Technology (NST). KVN operations are supported by the Korea Research Environment Open Network (KREONET), which is managed and operated by the Korea Institute of Science and Technology Information (KISTI).

ORCID iDs

Hyeon Baek https://orcid.org/0009-0002-9223-8819
Se-Hyung Cho https://orcid.org/0000-0002-2012-5412
Jaeheon Kim https://orcid.org/0000-0001-9825-7864
Seung-Min Son https://orcid.org/0009-0007-1400-7413
Dong-Hwan Yoon https://orcid.org/0000-0001-7120-8851
Kyung-Won Suh https://orcid.org/0000-0001-9104-9763

References

Alcolea, J., Pardo, J., Bujarrabal, V., et al. 1999, A&AS, 139, 461
Balister, M., Batchelor, R., Haynes, R., et al. 1977, MNRAS, 180, 415
Bedijn, P. 1987, A&A, 186, 136
Benson, P. J., Little-Marenin, I. R., Woods, T. C., et al. 1990, ApJS, 74, 911
Bertre, L. 1993, A&AS, 97, 729
Boboltz, D. A., & Claussen, M. 2004, ApJ, 608, 480
Boboltz, D. A., & Wittkowski, M. 2005, ApJ, 618, 953
Bowers, P., & Hagen, W. 1984, ApJ, 285, 637
Brand, J., Engels, D., & Winnberg, A. 2020, A&A, 644, A45
Bujarrabal, V. 1994, A&A, 285, 953
Bujarrabal, V., Alcolea, J., Sanchez Contreras, C., & Colomer, F. 1996, A&A, 314, 883
Chen, X., Shen, Z.-Q., & Xu, Y. 2007, ChJAA, 7, 531
Cherchneff, I. 2006, A&A, 456, 1001
Cho, C.-Y., Cho, S.-H., Kim, S., et al. 2017, ApJS, 232, 13
Cho, S.-H., Chung, H.-S., Kim, H.-G., et al. 2009, ApJS, 181, 421
Cho, S.-H., Chung, H.-S., Kim, H.-R., et al. 1998, ApJS, 115, 277
Cho, S.-H., Kaifu, N., & Ukita, N. 1996, AJ, 111, 1987
Cho, S.-H., & Kim, J. 2012, AJ, 144, 129
Danilovich, T., Richards, A., Decin, L., Van de Sande, M., & Gottlieb, C. 2020, MNRAS, 494, 1323
Danilovich, T., Richards, A., Karakas, A., et al. 2019, MNRAS, 484, 494
Danilovich, T., Teyssier, D., Justtanont, K., et al. 2015, A&A, 581, A60
De Beck, E., Decin, L., De Koter, A., et al. 2010, A&A, 523, A18
De Vicente, P., Bujarrabal, V., Dìaz-Pulido, A., et al. 2016, A&A, 589, A74
Decin, L., De Beck, E., Brünken, S., et al. 2010, A&A, 516, A69
Decin, L., Montargès, M., Richards, A., et al. 2020, Sci, 369, 1497
Decin, L., Richards, A., Danilovich, T., Homan, W., & Nuth, J. 2018, A&A, 615, A28
Desmurs, J.-F., Bujarrabal, V., Lindqvist, M., et al. 2014, A&A, 565, A127
Diamond, P., Kemball, A., Junor, W., et al. 1994, ApJL, 430, L61
Diamond, P. J., & Kemball, A. 2003, ApJ, 599, 1372
Duari, D., Cherchneff, I., & Willacy, K. 1999, A&A, 341, 47
Duari, D., & Hatchell, J. 2000, A&A, 358, L25
Elitzur, M. 1982, ApJ, 262, 189
Engels, D., Schmid-Burgk, J., & Walmsley, C. 1986, A&A, 167, 129
Glass, I., & Van Leeuwen, F. 2007, MNRAS, 378, 1543
Gómez, Y., Moran, J., & Rodrìguez, L. 1990, RMxAA, 20, 55
Gonidakis, I., Diamond, P., & Kemball, A. 2010, MNRAS, 406, 395

Gonidakis, I., Diamond, P., & Kemball, A. 2013, MNRAS, 433, 3133
Gottlieb, C. A., Decin, L., Richards, A. M. S., et al. 2022, A&A, 660, A94
Hinkle, K. H., Scharlach, W. W., & Hall, D. N. 1984, ApJS, 56, 1
Humphreys, E., Gray, M., Yates, J., et al. 2002, A&A, 386, 256
Imai, H. 2007, in IAU Symp. 242, Astrophysical Masers and their Environments, ed. J. M. Chapman & W. A. Baan (Cambridge: Cambridge Univ. Press), 279
Inomata, N., Imai, H., & Omodaka, T. 2007, PASJ, 59, 799
Jones, T., & Merrill, K. 1976, ApJ, 209, 509
Josselin, E., Loup, C., Omont, A., et al. 1998, A&AS, 129, 45
Kang, J., Cho, S.-H., Kim, H.-G., et al. 2006, ApJS, 165, 360
Kim, D.-J., Cho, S.-H., Yun, Y., et al. 2018, ApJL, 866, L19
Kim, J., Cho, S.-H., & Kim, S. J. 2012, AJ, 145, 22
Kim, J., Cho, S.-H., & Kim, S. J. 2014, AJ, 147, 22
Kim, J., Cho, S.-H., Oh, C. S., & Byun, D.-Y. 2010, ApJS, 188, 209
Knapp, G., Pourbaix, D., Platais, I., & Jorissen, A. 2003, A&A, 403, 993
Lane, A. P. 1982, Ph.D.thesis, University of Massachusetts
Lewis, B. 1989, ApJ, 338, 234
Lockett, P., & Elitzur, M. 1992, ApJ, 399, 704
Martinez, A., Rydbeck, O., Bujarrabal, V., & Alcolea, J. 1988, A&A, 74, 273
Marvel, K. B. 2005, AJ, 130, 261
McDonald, I., & Zijlstra, A. 2016, ApJL, 823, L38
Nyman, L.-A., & Olofsson, H. 1986, A&A, 158, 67
Olofsson, H., Rydbeck, O., Lane, A., & Predmore, C. 1981, ApJL, 247, L81
Olofsson, H., Rydbeck, O., & Nyman, L.-A. 1985, A&A, 150, 169
Pardo, J., Alcolea, J., Bujarrabal, V., Colomer, F., & de Vicente, P. 2004, A&A, 424, 145
Pardo, J., Cernicharo, J., Gonzalez-Alfonso, E., & Bujarrabal, V. 1998, A&A, 329, 219
Perryman, M. A., Lindegren, L., Kovalevsky, J., et al. 1997, A&A, 323, L49
Pijpers, F., Pardo, J., & Bujarrabal, V. 1994, A&A, 286, 501
Ramstedt, S., Montez, R., Kastner, J., & Vlemmings, W. 2012, A&A, 543, A147
Ramstedt, S., Schöier, F. L., & Olofsson, H. 2009, A&A, 499, 515
Reid, M. J., & Menten, K. M. 1997, ApJ, 476, 327
Reid, M. J., & Moran, J. M. 1981, ARA&A, 19, 231
Richards, A., Etoka, S., Gray, M., et al. 2012, A&A, 546, A16
Richards, A. M. S. 2012, in IAU Symp. 287, Cosmic Masers - from OH to H0, ed. R. S. Booth, W. H. T. Vlemmings, & E. M. L. Humphreys (Cambridge: Cambridge Univ. Press), 199
Richards, A. M. S., Assaf, K. A., Baudry, A., et al. 2022, in IAU Symp. 366, The Origin of Outflows in Evolved Stars, ed. L. Decin, A. Zijlstra, & C. Gielen (Cambridge: Cambridge Univ. Press), 204
Rizzo, J. R., Cernicharo, J., & García-Mirö, C. 2021, ApJS, 253, 44
Rowan-Robinson, M., Lock, T., Walker, D., & Harris, S. 1986, MNRAS, 222, 273
Rudnitskij, G., Lekht, E., Mendoza-Torres, J., Pashchenko, M., & Berulis, I. 2000, A&AS, 146, 385
Samus', N., Kazarovets, E., Durlevich, O., Kireeva, N., & Pastukhova, E. 2017, ARep, 61, 80
Schöier, F. L., Fong, D., Olofsson, H., Zhang, Q., & Patel, N. 2006, ApJ, 649, 965
Schwartz, P., Zuckerman, B., & Bologna, J. 1982, ApJL, 256, L55
Sevenster, M. N. 2002, AJ, 123, 2788
Shintani, M., Imai, H., Ando, K., et al. 2008, PASJ, 60, 1077
Stroh, M. C., Pihlström, Y. M., Sjouwerman, L. O., et al. 2018, ApJ, 862, 153
Su, J., Shen, Z.-Q., Chen, X., et al. 2012, ApJ, 754, 47
Trabucchi, M., Wood, P. R., Montalbán, J., et al. 2017, ApJ, 847, 139
van der Veen, W., & Habing, H. 1988, A&A, 194, 125
VanderPlas, J. T. 2018, ApJS, 236, 16
Wallström, S., Danilovich, T., Müller, H., et al. 2024, A&A, 681, A50
Willson, L. A. 2000, ARA&A, 38, 573
Winnberg, A., Brand, J., & Engels, D. 2011, in ASP Conf. Ser. 445, Why Galaxies Care about AGB Stars II: Shining Examples and Common Inhabitants, ed. F. Kerschbaum (San Francisco, CA: ASP), 375
Winnberg, A., Engels, D., Brand, J., Baldacci, L., & Walmsley, C. 2008, A&A, 482, 831
Wood, P., Alcock, C., Allsman, R., et al. 1999, in IAU Symp. 191, Asymptotic Giant Branch Stars, ed. T. L. Bertre, A. Lebre, & C. Waelkens (Cambridge: Cambridge Univ. Press), 151
Yoon, D.-H., Cho, S.-H., Kim, J., joo Yun, Y., & Park, Y.-S. 2014, ApJS, 211, 15
Yoon, D.-H., Cho, S.-H., Yun, Y., et al. 2018, NatCo, 9, 2534
Yun, Y., Cho, S.-H., Imai, H., et al. 2016, ApJ, 822, 3